arXiv:1612.04293v1 [astro-ph.GA] 13 Dec 2016

# Silicate Dust in Active Galactic Nuclei

**DRAFT: 2016.12.14.118**

Yanxia Xie[1,2,3], Aigen Li[2], and Lei Hao[1]

## ABSTRACT

The unification theory of active galactic nuclei (AGNs) hypothesizes that all AGNs are surrounded by an anisotropic dust torus and are essentially the same objects but viewed from different angles. However, little is known about the dust which plays a central role in the unification theory. There are suggestions that the AGN dust extinction law appreciably differs from that of the Galaxy. Also, the silicate emission features observed in type 1 AGNs appear anomalous (i.e., their peak wavelengths and widths differ considerably from that of the Galaxy). In this work, we explore the dust properties of 147 AGNs of various types at redshifts $z \lesssim 0.5$, with special attention paid to 93 AGNs which exhibit the 9.7 and 18 $\mu$m silicate emission features. We model their silicate emission spectra obtained with the *Infrared Spectrograph* aboard the *Spitzer Space Telescope*. We find that 60/93 of the observed spectra can be well explained with "astronomical silicate", while the remaining sources favor amorphous olivine or pyroxene. Most notably, all sources require the dust to be $\mu$m-sized (with a typical size of $\sim 1.5 \pm 0.1\,\mu$m), much larger than sub-$\mu$m-sized Galactic interstellar grains, implying a flat or "gray" extinction law for AGNs. We also find that, while the 9.7 $\mu$m emission feature arises predominantly from warm silicate dust of temperature $T \sim 270$ K, the $\sim$5–8 $\mu$m continuum emission is mostly from carbon dust of $T \sim 640$ K. Finally, the correlations between the dust properties (e.g., mass, temperature) and the AGN properties (e.g., luminosity, black hole mass) have also been investigated.

*Subject headings:* dust, extinction — galaxies: nuclei — (galaxies:) quasars: general — infrared: galaxies

[1]Shanghai Astronomical Observatory, Chinese Academy of Sciences, 80 Nandan Road, Shanghai 200030, China; xieya@missouri.edu, haol@shao.ac.cn

[2]Department of Physics and Astronomy, University of Missouri, Columbia, MO 65211, USA; lia@missouri.edu

[3]Kavli Institute for Astronomy and Astrophysics, Peking University, Beijing 100871, China; yanxia.xie@pku.edu.cn

## 1. Introduction

The unification theory of active galactic nuclei (AGNs) invokes an anisotropic dusty torus to account for the observational dichotomy of AGNs (Atonucci 1993, Urry & Padovani 1995). This theory assumes that, for type 2 AGNs, the dust torus blocks the photons from the broad line region and accretion disk when they are viewed through the edge of the torus. For type 1 AGNs, the line of sight is perpendicular to the dusty torus and allows the detection of the broad emission lines. The existence of such a dust torus around AGNs has been confirmed through the detection of polarized broad emission lines in type 2 AGNs. These polarized lines are believed to arise from the otherwise-blocked broad line regions in type 2 AGNs, and they are detected just because they are scattered by dust into the viewing line-of-sight (e.g., see Antonucci & Miller 1985, Lumsden et al. 2004).

What is the AGN dust torus composed of? essentially, the torus forms out of the original interstellar matter (gas and dust) of the host galaxies of AGNs. These dust grains of interstellar origin are processed by the X-ray and ultraviolet (UV) radiation of the central engine (e.g., see Voit 1991, Li 2007). They may also undergo coagulational growth in the torus (e.g., see Maiolino et al. 2001). As amorphous silicate and some sorts of carbonaceous dust are the major dust species of interstellar grains (e.g., see Mishra & Li 2015), one naturally expects amorphous silicate dust and carbon dust (e.g., graphite, amorphous carbon) to be present in the dust torus around AGNs. According to the unification theory, type 1 AGNs are expected to show silicate emission around 9.7 and 18 $\mu$m while type 2 AGNs are expected to show silicate absorption. The detection of silicate emission in a wide variety of type 1 AGNs ranging from luminous quasars to low-luminosity Seyfert galaxies (e.g., see Hao et al. 2005a, Siebenmorgen et al. 2005, Sturm et al. 2005, Hao et al. 2007, Xie et al. 2014) as well as silicate absorption in type 2 Seyfert galaxies (e.g., see Rieke & Low 1975, Jaffe et al. 2004, Roche et al. 2007, Shi et al. 2014) and type 2 QSOs (e.g., see Sturm et al. 2006, Nikutta et al. 2009) provides further support for the unification theory of AGNs.

However, the detection of silicate emission (and absorption as well) in AGNs is found to be rather diverse among different AGN types as revealed from the rich data set obtained by the *Infrared Spectrograph* (IRS) on board the *Spitzer Space Telescope* (Houck et al. 2004). Type 1 Seyfert galaxies are found equally displaying silicate emission and weak absorption in the mid infrared (IR; Hao et al. 2007), meanwhile some type 2 AGNs exhibit silicate emission rather than absorption (e.g., see Sturm et al. 2006, Mason et al. 2009, Nikutta et al. 2009). For those in which the silicate dust is seen in emission, the silicate feature often shows an "anomalous" spectral profile: the peak wavelength of the Si–O stretching feature which has a canonical wavelength of $\sim 9.7\,\mu$m in the Milky Way diffuse interstellar medium (ISM; e.g., see Kemper et al. 2004, Chiar & Tielens 2006, Henning 2010) often shifts to longer

wavelengths beyond $\sim 10\,\mu$m in AGNs (e.g., see Sturm et al. 2005, Mason 2015). Also, this feature often shows a much broader width compared to that of the Milky Way diffuse ISM (see Li et al. 2008, Smith et al. 2010 and references therein).

The spectral profile of the $9.7\,\mu$m silicate absorption feature seen in AGNs also exhibit spatial variations. Spatially-resolved observations of Circinus, a Seyfert 2 galaxy, made by Tristram et al. (2007) using the *Mid-Infrared Interferometric* (MIDI) instrument at the *Very Large Telescope* (VLT) reveals a two-component structure: an inner disk-like ($\sim 0.4\,$pc) component showing mild silicate emission around $\sim 10\,\mu$m, and an outer, extended, cooler torus ($\sim 2.0\,$pc) exhibiting silicate absorption. Both the emission and absorption features of Circinus resemble the spectral profile of the Milky Way diffuse ISM. On the other hand, the spatially-resolved mid-IR spectrum of NGC 1068, a prototypical type 2 AGN, shows that the silicate absorption profile varies with the distance to the nucleus, with the maximum absorption occurring around the innermost region (Rhee & Larkin 2006, Mason et al. 2006). Particularly, the *VLT*/MIDI observations of the central $\sim 2.0\,$pc of NGC 1068 reveal that the silicate absorption profile also appears "anomalous": differing from that of the Galactic ISM and that of common olivine-type silicate dust, the $9.7\,\mu$m silicate absorption feature of NGC 1068 shows a relatively flat profile from $\sim 8$ to $9\,\mu$m and then a sharp drop between $\sim 9$ and $10\,\mu$m, while the Galactic silicate absorption profiles already begin to drop at $\sim 8\,\mu$m (see Figure 1 of Köhler & Li 2010).

Li et al. (2008) examined the anomalous redward-shifting of the peak wavelength and broadening of the width of the $9.7\,\mu$m emission feature observed in the bright quasar 3C 273 and the low-luminosity AGN NGC 3998. They ascribed the anomalous silicate emission profile of 3C 273 and NGC 3998 to porous dust. Such an anomalous emission profile is also detected in the type 1 nucleus of M 81, a low-ionization nuclear emission-line region (LINER) and is explained in terms of $\mu$m-sized grains (Smith et al. 2010). In contrast, the anomalous spectral profile of the $9.7\,\mu$m silicate feature observed in the innermost region of NGC 1068 was attributed to the presence of silicon carbide dust (Köhler & Li 2010) or to a less extent, gehlenite ($Ca_2Al_2SiO_7$), a high-temperature calcium aluminum silicate species. However, Nikutta et al. (2009) argued that, in the framework of a clumpy dust torus, the observed anomaly in the silicate emission and absorption profiles does not necessarily imply anomalies in dust size, structure or composition; instead, they argued that it could simply be caused by radiation transfer effects. But Xie et al. (2015, 2016) noted that the success of the "Clumpy" dust torus model (Nenkova et al. 2008a,b, Schartmann et al. 2008, Hönig & Kishimoto 2010) in explaining the much longer peak wavelength of the silicate Si–O emission feature (compared to that of the Galactic diffuse ISM) seems to be due to the adoption of a set of silicate opacity differing from that commonly adopted: Nikutta et al. (2009) adopted the silicate opacity of Ossenkopf et al. (1992) which peaks at $\sim 10.0\,\mu$m while the

commonly-adopted opacity profile of "astronomical silicate" of Draine & Lee (1984) peaks at $\sim 9.5\,\mu$m. Note that the observed silicate absorption profiles of the Galactic diffuse ISM peak at $\sim 9.7\,\mu$m (e.g., see Kemper et al. 2004, Chiar & Tielens 2006, Henning 2010).

The exact properties of the silicate dust component in AGN torus remain debated and no consensus has yet been reached. As elaborated above, the current knowledge about the silicate dust properties of AGNs are mainly derived from several individual sources. To address the observed silicate diversity among AGNs and to gain insight into the origin of the AGN dichotomy, it is necessary to study the silicate spectral profiles for a large and well defined AGN sample, taking into account a wide range of dust compositions and sizes. In this work we will model the *Spitzer*/IRS spectra of a large sample of 147 AGNs, including both type 1 and type 2 AGNs at both high and low luminosity levels. Such a large AGN sample will allow us to obtain a better understanding of the size and composition of the dust grains in AGN torus. For simplicity, we will focus on those AGNs showing silicate emission (see §2.1).

The structure of this paper is organized in the following sequence. We briefly describe the sample in §2 and elaborate the dust model in §3. We present in §4 the results derived from modeling the *Spitzer*/IRS spectra of 147 AGNs. Also in §4 we discuss the model-derived dust properties (e.g., composition, size, temperature) and their relations with the AGN parameters (e.g., accretion rate, luminosity, black hole mass). We summarize the major results of this paper in §5. Throughout the paper, we take the following cosmology parameters: $\Omega_m = 0.3$, $\Omega_\wedge = 0.7$, and $H_0 = 70\,h_{70}$ km s$^{-1}$ Mpc$^{-1}$.

## 2. Sample and Data

### 2.1. Samples

Our AGN sample is mainly collected from the literature. We consider all 87 PG quasars at $z \lesssim 0.5$ (Schmidt & Green 1983, Boroson & Green 1992) and all 52 *2MASS* quasars at $z \lesssim 0.3$ (Cutri et al. 2001, Smith et al. 2002). We also consider all 253 AGNs from the *Spitzer/IRS-SDSS Spectral Atlas of Galaxies and AGNs* (S$^3$AGA; L. Hao et al. 2016, in preparation) at $z \lesssim 0.33$.

PG quasars are selected to have an average $B$-band absolute magnitude of $\sim 16.16$, $U-B$ color of $\lesssim -0.44$, and a dominant point-like sources. All these objects show broad emission lines in optical, and thus are classified as type 1 quasars. Due to the large photographic magnitude errors and the simple color selection criterion, the PG sample is incomplete (e.g., see Goldschmidt et al. 1992, Jester et al. 2005), but the incompleteness is independent of

the optical magnitude and color (Jester et al. 2005). This indicates that the PG sample is still representative of bright optically selected quasars. In comparison with PG quasars, the *2MASS* quasars represent a redder population with $J - K_S \gtrsim 2$ (compared to a typical color of $J - K_S \gtrsim 1.5$ for PG quasars), but have a similar $K_S$-band luminosity of $K_S \lesssim 23$ (Smith et al. 2002). Unlike PG quasars, the *2MASS* sample includes objects with narrow, intermediate and broad emission lines. The *2MASS* sample is highly incomplete at $K_S \gtrsim 13$ (Cutri et al. 2001). Throughout the following text, we will refer to this sample as the quasar sample.

$S^3$AGA is a heterogeneous collection of galaxies that have *Spitzer*/IRS low-resolution spectra (Houck et al. 2004) and *Sloan Digital Sky Survey* (SDSS) spectroscopic observations (Data Release 7; Abazajian et al. 2009) within a $\sim 3''$ searching radius. The whole $S^3$AGA sample contains 139 type 1 AGNs, 114 type 2 AGNs, 241 star-forming (SF) galaxies, 103 AGN-SF composites, and one quiescent galaxy. The galaxy types are classified based on the *SDSS* optical emission line properties (see Hao et al. 2005b).[1] Throughout the following text, we will refer to this sample as $S^3$AGA.

In this work we will disregard those sources which show silicate in absorption since they do not contain a sufficient amount of information for constraining the nature of the dust (particularly, the temperature of the dust). Also, the silicate absorption could have been contaminated by the interstellar silicate dust of the AGN's host galaxy. Therefore, we are left with 147 sources (i.e., 85 PG quasars, 18 *2MASS* quasars, and 44 $S^3$AGA AGNs). In Appendix we list the basic parameters including the redshift ($z$), type, black-hole mass ($M_{\rm BH}$), and luminosity at $\lambda = 5100\,$Å for each of our 147 sources. Among these objects, the *Spitzer*/IRS spectra of 62 PG quasars, 13 *2MASS* quasars and 18 $S^3$AGA AGNs show silicate in emission. We will focus on these 93 "silicate emission" sources which show silicate emission at 9.7 and $18\,\mu$m.

### 2.2. Data

For the selected sample sources, we utilize the low resolution mid-IR spectra obtained by *Spitzer*/IRS. The spectral wavelength ranges from $\sim 5\,\mu$m to $\sim 38\,\mu$m and the spectral resolution varies between $\sim 60$ and $\sim 128$.

[1]Type 1 AGNs are those exhibiting broad H$\alpha$ emission lines with an FWHM of $\gtrsim 1200\,{\rm km\,s^{-1}}$. Type 2 AGNs are identified with the emission line ratios featuring the Baldwin, Phillips, & Terlevich (1989; BPT) diagram. This sample spans a redshift range of $z \sim 0.001$–$0.25$, corresponding to a physical size of $\sim 0.06$–$18\,$kpc in the *SDSS* $3''$ aperture.

The *Spitzer*/IRS spectra for the quasar sample are compiled from Shi et al. (2014). The detailed observations and data reduction can be found in Shi et al. (2014) and reference therein. For the S$^3$AGA sample, the mid-IR spectra are obtained from the *Cornell Atlas of Spitzer/IRS Sources* (CASSIS) which have been processed with Pipeline S18.7 (Lebouteiller et al. 2011). For more details we refer to L. Hao et al. (2016, in preparation).

We have not specifically applied any quantitative signal-to-noise (SNR) cut to the selected spectra; instead, the selection is mainly based on visual inspection and we require an apparent detection of the 9.7 and 18 $\mu$m silicate emission features or a flat, featureless emission continuum.[2] As demonstrated in §4.6, the "silicate emission" sources and the "flat continuum" sources appreciably distinguish themselves from each other in terms of the flux fraction of the silicate emission features in the total mid-IR emission. Finally, we note that for those sources whose *Spitzer*/IRS spectra are of a rather low SNR, we will exclude them when we statistically examine whether (and how) the dust properties are related to the AGN properties.

## 3. The Dust Model

We aim to constrain the dust chemical composition, size, and temperature through modeling the observed dust thermal IR emission. We will consider two kinds of dust: amorphous silicate and carbonaceous dust. For the former, we will consider a range of compositions: (1) the Draine & Lee (1984) "astronomical silicate", (2) three pyroxene species ($Mg_xFe_{1-x}SiO_3$ with $x = 0.4, 0.7, 1.0$), and (3) two olivine species ($Mg_{2x}Fe_{2(1-x)}SiO_4$ with $x = 0.4, 0.5$). For the latter, we will consider graphite and amorphous carbon. Although other dust species (e.g., SiC, oxides) may also be present in AGN torus (e.g., see Laor & Draine 1993, Markwick-Kemper et al. 2007, Köher & Li 2010), in this work they are not included in our model. The dust is expected to have a distribution of sizes. For simplicity, we will only consider 100 discrete sizes: $a = 0.1$, 0.2, ..., 10.0 $\mu$m at a step of 0.1 $\mu$m where $a$ is the spherical radius of the dust (we assume a spherical shape for the dust). The dust is also expected to have a distribution of temperatures, with the dust temperature reaching $\gtrsim$1500 K — the sublimation temperature of silicate, graphite and amorphous carbon and dropping to $\lesssim$100 K in the outer boundary of the torus. Also for simplicity, we will only consider two temperatures — a warm component of temperature $T_w$ and a cold component of temperature $T_c$— to represent the temperature distribution.

[2]For some sources, the flat emission continuum may be superimposed by several spectral features from polycyclic aromatic hydrocarbon (PAH) molecules (see §4.6).

Assuming that the torus is optically thin in the IR, we model the dust IR emission as

$$F_\nu = \frac{1}{d^2} \times \sum_i \left\{ B_\nu(T_{\rm w,}i) \times \kappa_{\rm abs,}i(\nu) \times M_{\rm w,}i + B_\nu(T_{\rm c,}i) \times \kappa_{\rm abs,}i(\nu) \times M_{\rm c,}i \right\} \quad , \tag{1}$$

where the sum is over the two dust species (silicate and graphite or amorphous carbon), $d$ is the luminosity distance of the object, $\kappa_{{\rm abs},i}(\nu)$ is the mass absorption coefficient (in unit of $\rm cm^2\,g^{-1}$) of dust of type $i$, $B_\nu(T)$ is the Planck function of temperature $T$ at frequency $\nu$, $T_{{\rm w},i}$ and $T_{{\rm c},i}$ are respectively the temperatures of the warm and cold components of dust of type $i$, and $M_{{\rm w},i}$ and $M_{{\rm c},i}$ are respectively the masses of the warm and cold components of dust of type $i$. For a given composition and size, the mass absorption coefficient $\kappa_{\rm abs}(\nu)$ is obtained from Mie theory (Bohren & Huffman 1983) using the refractive indices (1) of Draine & Lee (1984) for "astronomical silicate" and graphite, (2) of Dorschner et al. (1995) for amorphous pyroxene and amorphous olivine, and (3) of Rouleau & Martin (1991) for amorphous carbon. We refer the reader to Figure 2 of Xie et al. (2015) for the computed $\kappa_{\rm abs}(\nu)$ profiles for different grain materials and sizes.

## 4. Results and Discussion

In fitting the observed IR emission, we have eight parameters: the temperature ($T_{\rm w}^{\rm S}$) and mass ($M_{\rm w}^{\rm S}$) for the warm silicate component, the temperature ($T_{\rm c}^{\rm S}$) and mass ($M_{\rm c}^{\rm S}$) for the cold silicate component, the temperature ($T_{\rm w}^{\rm G}$) and mass ($M_{\rm w}^{\rm G}$) for the warm carbon dust component, and the temperature ($T_{\rm c}^{\rm G}$) and mass ($M_{\rm c}^{\rm G}$) for the cold carbon dust component. We require the dust temperatures not to exceed the sublimation temperature ($T_{\rm subl} \sim 1500\,{\rm K}$) of silicate and graphite materials. By applying cosmic abundance constraints to $M_{\rm carb}/M_{\rm sil}$, the mass ratio of the silicate component to the carbon dust component, we require $0.2 < M_{\rm carb}/M_{\rm sil} < 2$ (see Xie et al. 2015). With these constraints taken into account, we obtain the best fit for each galaxy using the MPFIT code, an IDL $\chi^2$-minimization routine based on the Levenberg-Marquardt algorithm (Markwardt 2009). The quality of the fit is measured by the reduced $\chi^2$ which is defined as follows:

$$\chi^2/{\rm dof} = \sum_{j=1}^{N_{\rm obs}} \left\{ \frac{F_\nu({\rm mod}) - F_\nu({\rm obs})}{\sigma_\nu({\rm obs})} \right\}^2 / \left\{ N_{\rm obs} - N_{\rm mod} \right\} \quad , \tag{2}$$

where $F_\nu({\rm mod})$ is the model-calculated flux density, $F_\nu({\rm obs})$ is the observed flux density, $\sigma_\nu({\rm obs})$ is the observational uncertainty of the flux density $F_\nu({\rm obs})$, $N_{\rm obs}$ is the number of data points, and $N_{\rm mod} = 8$ is the number of model parameters.

We note that the *Spitzer*/IRS spectra in the $\sim$5–14.5 $\mu$m wavelength interval have a lower SNR compared with that in the interval of $\sim$14.5–38 $\mu$m. This is due to the different

observational modules, i.e., the $\sim$5–14.5 $\mu$m *Short Low* (SL) IRS module has a slit width of $\sim 3.6''$, while the $\sim$14.5–38 $\mu$m *Long Low* (LL) IRS module has a slit width of $\sim 11.2''$. To fit the $\sim$5–8 $\mu$m continuum emission and the 9.7 $\mu$m silicate emission feature, for those sources of which the SL spectra are rather noisy (including PG1352+183, 2MASSiJ132917.5+121340, 2MASSiJ234259.3+134750, 2MASXJ02335161+0108136, 2MASXJ13495283+0204456, and SDSSJ115138.24+004946.4), we arbitrarily increase the weights respectively by a factor of ten and two for the data points at $\sim$5–8 $\mu$m and $\sim$8–14.5 $\mu$m (relative to that at $\sim$14.5–38 $\mu$m). These sources will be excluded when we perform statistical analyses of the possible correlations between the dust properties and the AGN properties.

In Figure 1, we show the best-fit results to all 93 "silicate emission" sources which exhibit prominent silicate emission at 9.7 and 18 $\mu$m. The best-fit model parameters and their uncertainties are tabulated in Table 1. The uncertainties for the model parameters are derived by performing Monte-Carlo simulations. As illustrated in Figure 2 with PG 2233+134 as an example, we assume that the *Spitzer*/IRS flux density uncertainty statistically follows a normal distribution. The dispersion is taken to be the observed $1\sigma$ error, composed of the statistical and systematic errors, with the latter arising from the flux differences between the two nods of the *Spitzer*/IRS spectra, the sky background contamination, and the *Spitzer*/IRS pointing and flux calibration errors (Lebouteiller et al. 2011). A new "observational" spectrum is generated through randomly sampling a point at each wavelength from the normal distribution. We then model the new spectrum and derive a set of model parameters. We conduct 100 simulations for each source as the parameters derived from 10,000 simulations only slightly differ from that derived from 100 simulations (Xie et al. 2015). The final model spectrum is calculated from the median values of the model parameters. The error of each parameter is derived from the standard deviation of 100 simulations.

### 4.1. Dust Composition

We find that the combination of the Draine & Lee (1984) "astronomical silicate" and graphite can closely reproduce the *Spitzer*/IRS spectra of 60 of our 93 AGNs. For 31 AGNs, amorphous olivine combined with graphite fits the observed spectra better than "astronomical silicate". In contrast, amorphous pyroxene provides the best fit to two of our 93 AGNs (i.e, PG 1535+547 and PG 2214+139). For illustration, in Figure 3 we show the best-fit results for three PG quasars (PG 1004+130, PG 1351+640, and PG 2214+139) for which the best-fits are respectively provided by "astronomical silicate", amorphous olivine $Mg_{1.2}Fe_{0.8}SiO_4$, and amorphous pyroxene $Mg_{0.3}Fe_{0.7}SiO_3$, again, together with graphite. Different silicate species have different band widths, peak wavelengths, and relative strengths

for the 9.7 and 18 $\mu$m features. For a given grain size, the Draine & Lee (1984) "astronomical silicate" results in an absorption profile at 9.7 $\mu$m much broader than amorphous olivine and pyroxene, while amorphous olivine gives the longest peak wavelength for the 9.7 $\mu$m feature and the highest ratio of the 18 $\mu$m feature to the 9.7 $\mu$m feature, and amorphous pyroxene has the smallest ratio of the 9.7 $\mu$m feature to the "trough" between the 9.7 and 18 $\mu$m features. As elaborated in Figure 3, the *Spitzer*/IRS spectra of PG 1004+130, PG 1351+640, and PG 2214+139 show considerable variations in the spectral profiles of the 9.7 and 18 $\mu$m emission features. For illustration, we display in Figure 4 the *Spitzer*/IRS spectra of several selected AGNs for which the best fits favor "astronomical silicate", amorphous olivine, and amorphous pyroxene, respectively. Although complicated by the dust size and temperature effects, a first glance of Figure 4 would already tell that these AGNs differ in silicate composition and their spectral profiles appear consistent with the feature width and band ratio expected from "astronomical silicate", amorphous olivine, or amorphous pyroxene, respectively.

There are also several AGNs for which their silicate emission features can not be closely fitted in terms of "astronomical silicate", amorphous olivine, or amorphous pyroxene. We note that, except a couple of sources of which the *Spitzer*/IRS spectra are noisy (e.g., PG 1352+183), most of these AGNs probably have other dust species (e.g., crystalline silicates) present. In Figure 5 we display the *Spitzer*/IRS spectra of those sources which exhibit the crystalline silicate emission features at 11.3, 16.3, 18.5, 23.5, and 27.5 $\mu$m.

Finally, we note that our model fitting is not sensitive to the choice of graphite or amorphous carbon. However, the opacity profile of amorphous carbon exhibits several weak resonant structures in the wavelength range of $\sim$5–8 $\mu$m (see Figure 3b of Xie et al. 2015) which are not seen in the *Spitzer*/IRS spectra of the AGNs considered here. Therefore, graphite appears more favorable.

### 4.2. Dust Sizes

From our fitting, we find that the *Spitzer*/IRS spectra of 70 of our 93 AGNs can be well reproduced with spherical grains of radii $a = 1.5\,\mu$m. Only three AGNs require grains smaller than $a = 1\,\mu$m. In Figure 6 we show the histogram of the best-fit grain sizes. Roughly speaking, the sizes of the grains in the torus around these 93 AGNs which show silicate emission are constrained to be $\sim 1.5\pm0.1\,\mu$m. This is consistent with our previous work that the dust grains in AGNs are micrometer-sized (e.g., Li et al. 2008, Smith et al. 2010, Xie et al. 2015).

We calculate the extinction as a function of inverse wavelength ($\lambda^{-1}$) expected from

mixtures of spherical amorphous silicate and graphite of radii $a = 1.5\,\mu$m. We represent the extinction by $E(\lambda - V)/E(B - V)$, where $E(\lambda - V) \equiv A_\lambda - A_V$, $E(B - V) \equiv A_B - A_V$, and $A_\lambda$, $A_B$, and $A_V$ are respectively the extinction at wavelength $\lambda$, and at the $B$ and $V$ bands. As shown in Figure 7, the extinction curve predicted from a mixture of silicate and graphite grains of $a = 1.5\,\mu$m is flat or gray at $\lambda^{-1} > 2.5\,\mu\mathrm{m}^{-1}$, i.e., the extinction varies little with $\lambda^{-1}$. Depending on the mass ratio of graphite to silicate, the extinction displays a gradual rise at $\lambda^{-1} > 4.5\,\mu$m and then flattens off at $\lambda^{-1} > 6\,\mu$m. But overall, the extinction curve is flat. The resonant structures seen at $\lambda^{-1} < 2.5\,\mu\mathrm{m}^{-1}$ will be smoothed out if we consider a distribution of grain sizes instead of single sizes of $a = 1.5\,\mu$m.

The predicted gray extinction curve generally agrees with that of Gaskell et al. (2004) who derived an AGN extinction curve based on the composite spectra of 72 radio quasars and 1018 radio-quiet AGNs. Czerny et al. (2004) also constructed a relatively featureless flat extinction curve for quasars based on the blue and red composite quasar spectra of Richards et al. (2003) obtained from the Sloan Digital Sky Survey (SDSS). It is interesting to note that, the extinction curve calculated from spherical silicate dust of $a = 1.5\,\mu$m closely agrees with that of Gaskell et al. (2004) except those resonant structures at $\lambda^{-1} < 2.5\,\mu\mathrm{m}^{-1}$ which are expected to be smoothed out if a distribution of grain sizes is considered. The Galactic extinction curve differs substantially from our model extinction curve as well as that of Gaskell et al. (2004) in that, the Galactic extinction curve shows a prominent extinction bump at 2175 Å and a steep far-UV rise which is believed to arised from small graphite dust grains. In contrast, the extinction curve of the Small Magellanic Cloud (SMC) lacks the 2175 Å bump and displays an even steeper far-UV rise than that of the Milky Way.

### 4.3. Dust Temperatures

Figure 8 presents the histograms of the dust temperatures derived from our best-fits to the *Spitzer*/IRS spectra of these 93 "silicate emission" sources (which show silicate emission). It is seen that the temperatures for the warm silicate dust component ($T_{\rm w}^{\rm S}$) span from $\sim 150$ K to $\sim 500$ K, with a median value of $\sim 265$ K and a dispersion of $\sim 89$ K. The temperatures for the cold silicate component ($T_{\rm c}^{\rm S}$) vary from $\sim 40$ K to $\sim 200$ K. The median value is $\sim 66$ K for $T_{\rm c}^{\rm S}$ and the dispersion is $\sim 89$ K. For graphite, much higher temperatures are obtained: $T_{\rm w}^{\rm G}$ is in the range of $\sim 200$ K to $\sim 1000$ K, with a median value of $\sim 638$ K and a dispersion of $\sim 159$ K; $T_{\rm c}^{\rm G}$ is within $\sim 100$ K to $\sim 220$ K, with a median value of $\sim 159$ K and a dispersion of $\sim 22$ K. We note that, even if the spatial distributions of silicate and graphite are similar in an AGN torus, one expects graphite to be much hotter than silicate because of the much higher UV/optical absorptivities of graphite compared to that of silicate (see Draine & Lee

1984). Graphite grains could be distributed closer to the central engine of an AGN than silicate grains since graphite has a higher sublimation temperature (see Li 2009).

The grains in the AGN torus are heated by photons from the central engine. Let $R$ be the distance of a silicate or graphite grain of size $a$ from the central engine of luminosity $L_\lambda$. The steady-state temperature of the grain can be calculated from the energy balance between absorption and emission:

$$\int_0^\infty \frac{L_\lambda}{4\pi R^2} C_{\rm abs}(a,\lambda)\, d\lambda = \int_0^\infty 4\pi B_\lambda[T(a,R)] C_{\rm abs}(a,\lambda)\, d\lambda \quad , \tag{3}$$

where $C_{\rm abs}(a,\lambda)$ is the absorption cross section of the spherical grain of radii $a$ at wavelength $\lambda$, and $B_\lambda(T)$ is the Planck function of temperature $T$. For simplicity, in eq. 3 we neglect the extinction of the illuminating light in the torus. If the dust extinction is included, one would expect a smaller $R$ for the same dust temperature. For the AGN luminosity $L_\lambda$, we take the tabulated $L_\lambda(5100\,\text{Å})$ (see Table 4) and the spectral shape of Rowan-Robinson (1995). For each AGN and each dust component, we derive the distance of the dust from the central engine where the dust attains an equilibrium temperature exactly equaling that derived from the *Spitzer*/IRS spectral modeling. We find that the warm dust components are at several hundredth to tenth parsecs from the central engine and the cold dust components are at several parsecs from the central engine (see Figure 9). The actual distances could be smaller since the torus extinction is neglected in calculating the dust temperature. These results are consistent with Elitzur (2006) who argues for a torus size of no more than a few parsecs.

### 4.4. Dust Masses

We show in Figure 10 the mass ratios of the warm graphite component to the warm silicate component ($M_{\rm w}^{\rm G}/M_{\rm w}^{\rm S}$), and the mass ratios of the cold graphite component to the cold silicate component ($M_{\rm c}^{\rm G}/M_{\rm c}^{\rm S}$). We derive a mean ratio of $\sim 0.33$ for $M_{\rm w}^{\rm G}/M_{\rm w}^{\rm S}$, and a mean ratio of $\sim 0.93$ for $M_{\rm c}^{\rm G}/M_{\rm c}^{\rm S}$. However, these ratios should be treated with caution since for a substantial number of sources the mass ratio reaches the pre-set limiting values of $M_{\rm carb}/M_{\rm sil} = 0.2$ and $M_{\rm carb}/M_{\rm sil} = 2.0$ (see Figure 10). We find that reasonably good fits are still achievable as long as $M_{\rm carb}/M_{\rm sil} \gtrsim 0.05$.

For our "silicate emission" sources, the stellar mass ($M_\star$) is known for 39 PG quasars and two *2MASS* quasars (see Zhang et al. 2016). For each of these sources, we obtain $M_{\rm dust}$, the total dust mass summed over all four dust components (i.e., $M_{\rm dust} = M_{\rm w}^{\rm S} + M_{\rm c}^{\rm S} + M_{\rm w}^{\rm G} + M_{\rm c}^{\rm G}$). In Figure 11 we compare the dust mass with the stellar mass. On average, the dust-to-stellar mass ratio of these sources is $\sim 10^{-7}$, much smaller than that of the Milky Way ($\sim 10^{-3}$;

see Li 2004). This ratio appears reasonable since the mid-IR emission considered here only probes the dust in the torus while the bulk mass is in starlight-heated cold dust in the host galaxy which emits in the far-IR and escapes from detection by *Spitzer*/IRS.

### 4.5. Correlations between Dust and AGNs

With the dust properties determined, we now explore the possible connection between the fundamental properties of AGNs and the properties of the dust derived from the silicate emission modeling. If the dust in the torus is heated by the photons originating from the accretion disk, one would expect the dust properties to somewhat correlate with the AGN parameters. Therefore, we examine the correlation between the dust temperature and mass and the bolometric luminosity ($L_{\rm bol}$), black hole mass ($M_{\rm BH}$), and Eddington ratio ($L_{\rm bol}/L_{\rm Edd}$) of AGNs. We represent $L_{\rm bol}$ by $\lambda L_{\lambda}(5100\,\text{Å})$, since the spectral region at this wavelength is barely contaminated by emission lines and is assumed to be purely from the AGN accretion disk. The Eddington ratio ($\varepsilon$) relates the AGN bolometric luminosity with the Eddington luminosity: $\varepsilon \equiv L_{\rm bol}/L_{\rm Edd}$, with $L_{\rm Edd} = 4\pi cGMm_{\rm H}/\sigma_T$, where $c$ is the speed of light, $G$ is the gravitational constant, and $\sigma_T$ is the Thomson cross section. We compile these parameters from the literature and list them in Table 4.

In Figures 12, 13, 14 we present the correlations between the dust masses of the warm silicate, warm graphite, cold silicate and cold graphite components with the bolometric luminosity, the black hole mass, and the Eddington ratio of AGNs. While the dust masses show no correlation with the black hole mass or with the Eddington ratio, they do show a somewhat correlation with the bolometric luminosity (see Figure 12a,b,d). This suggests that the covering factor of the dust torus (i.e., the fraction of the sky covered by the torus as seen from the central engine) may increase with the bolometric luminosity of AGNs. Similarly, in Figures 15, 16, 17 we present the correlations between the temperatures ($T$) of the warm silicate, warm graphite, cold silicate and cold graphite components with the bolometric luminosity, the black hole mass, and the Eddington ratio of AGNs. No correlations are found. The lack of correlation between $T$ and $L_{\rm bol}$ is not unexpected since $T$ depends on both $L_{\rm bol}$ and $R$, the distance of the dust from the central engine.

### 4.6. Other Sources

Among our sample of 147 AGNs, there are 30 sources which do not show prominent silicate emission but a featureless thermal continuum in the mid-IR (hereafter we will call

these AGNs "flat continuum" sources). In addition, there are 24 sources exhibit weak PAH features superimposed on an otherwise featureless thermal continuum (hereafter we will call these AGNs "PAH + continuum" sources). In Figure 18 we show $F_{\rm silicate}/F_{\rm MIR}$, the fractional fluxes emitted in the 9.7 and 18 $\mu$m silicate features relative to the total mid-IR emission at $\sim$5–38 $\mu$m, for all three categories of sources.[3] It is apparent that, with a considerably larger mean fractional flux ($\langle F_{\rm silicate}/F_{\rm MIR}\rangle \approx 0.13$), the "silicate emission" sources clearly distinguish them from those "flat continuum" sources (with $\langle F_{\rm silicate}/F_{\rm MIR}\rangle \approx 0.041$) and "PAH + continuum" sources (with $\langle F_{\rm silicate}/F_{\rm MIR}\rangle \approx 0.051$). This confirms that the silicate emission features in the 93 "silicate emission" sources are indeed prominent and therefore the silicate dust properties yielded from our modeling have a high level of significance.

We have also modeled the *Spitzer*/IRS spectra of those 30 "flat continuum" sources which do not show any silicate emission but a featureless thermal continuum. As shown in Figure 19, mixtures of $\mu$m-sized silicate and graphite also provide close fits to the observed spectra. Compared with those "silicate emission" sources (which show prominent silicate emission features; see Figure 1), these sources have lower dust temperatures (see Figure 20). In Figure 21 we show the graphite-to-silicate mass ratios.

We have also modeled the thermal continuum emission of these 24 "PAH + continuum" sources with mixtures of silicate and graphite grains. As shown in Figure 22, the best-fits to the observed spectra are provided by $\mu$m-sized dust grains. The graphite-to-silicate mass ratios are shown in Figure 24. The derived dust temperatures are shown in Figure 23 and they are rather close to that of those PAH-lacking "flat continuum" sources. This suggests that the thermal continuum emission seen in these "PAH + continuum" AGNs is not from their host galaxies but from the torus.

A wide variety of Galactic and extragalactic objects show a distinctive set of emission features at 3.3, 6.2, 7.7, 8.6, and 11.3 $\mu$m. These features are generally identified as the vibrational modes of PAH molecules (Léger & Puget 1984, Allamandola, Tielens, & Barker 1985). However, the PAH features are often absent in AGNs (e.g., see Roche et al. 1991). This is generally interpreted as the destruction of PAHs by extreme UV and soft X-ray photons in AGNs (Roche et al. 1991, Voit 1992, Siebenmorgen, Krügel, & Spoon 2004). If the PAH emission and the thermal emission continuum seen in these sources are contaminated by their host galaxies, one would expect the dust to be smaller and colder than that in those "flat continuum" sources of which the *Spitzer*/IRS spectra are characterized by a featureless, PAH-lacking thermal continuum. This is because the interstellar dust grains in the host galaxies of AGNs are believed to be around $\sim$0.1 $\mu$m in size and $\sim$20 K in temperature (see

[3]For the "flat continuum" sources and the "PAH + continuum" sources, $F_{\rm silicate}$ is actually an upper limit.

Li & Draine 2001). But as we see that this is not the case. The PAH emission features may as well arise from the AGN torus, i.e., some quantities of PAHs may survive in the hostile environments of AGNs (L.C. Ho, private communication).

## 5. Summary

We have investigated the dust properties of a sample of 147 AGNs compiled from PG quasars, *2MASS* quasars, and S$^3$AGA AGNs which do not show silicate absorption features. Our principal results are as follows:

1. Through fitting the *Spitzer*/IRS spectra of 93 AGNs of various types in which the 9.7 and 18 $\mu$m emission features are seen in emission with mixtures of silicate and graphite grains, we find that the majority (60/93) of the observed spectra can be well reproduced by "astronomical silicate", with the remaining 31 sources favoring amorphous olivine and two sources favoring amorphous pyroxene.

2. All sources require the dust to be $\mu$m-sized (with a typical size of $\sim 1.5\,\mu$m), much larger than the sub-$\mu$m-sized Galactic interstellar dust. This implies a flat or "gray" extinction curve for AGNs.

3. The 9.7 $\mu$m emission feature arises predominantly from warm silicate dust of temperature $T \sim 270\,$K, while the $\sim$5–8 $\mu$m continuum emission is mostly from graphite of $T \sim 640\,$K.

4. We have examined the possible relations between the dust masses and temperatures and the bolometric luminosity, black hole masses, and Eddington ratios of AGNs. It is found that except the dust masses are somewhat correlated with the bolometric luminosity, we do not see any correlations between any other quantities.

5. We have also modeled the *Spitzer*/IRS spectra of 30 (of 147) sources which do not show silicate emission features but a featureless thermal continuum. Compared to those 93 sources which show silicate emission, $\mu$m-sized silicate and graphite grains with smaller silicate-to-graphite mass ratios and lower dust temperatures are preferred. We have also modeled the *Spitzer*/IRS spectra of 24 (of 147) sources which exhibit weak PAH emission features superimposed on an otherwise featureless thermal continuum. It is found that the derived dust sizes and temperatures are not appreciably different from that of those 30 sources which emit a featureless thermal continuum.

We thank B.T. Draine, L.C. Ho and the anonymous referee for stimulating discussions and suggestions. We thank Y. Shi for kindly providing us with the *Spitzer*/IRS spectra of PG quasars. A.L. and X.Y.X. are supported in part by NSF AST-1311804 and NASA NNX14AF68G. L.H. is supported by NSFC 11473305 and the CAS Strategic Priority Research Program XDB09030200. The Cornell Atlas of *Spitzer*/IRS Sources (CASSIS) is a product of the Infrared Science Center at Cornell University, supported by NASA and JPL.

## A. Basic Parameters for Our Sample of 147 AGNs

In this appendix we list the redshift ($z$), type, black-hole mass ($M_{\rm BH}$), and luminosity at $\lambda = 5100\,$Å for each of our 147 AGNs, which are divided into three categories: the "silicate emission" sources which exhibit the 9.7 and 18 $\mu$m silicate emission features (see Table 4), the "flat continuum" sources which exhibit a featureless emission continuum (see Table 5), and the "PAH + continuum" sources which show PAH emission features superimposed on an otherwise featureless continuum (see Table 6).

## REFERENCES

Abazajian, K. N., Adelman-McCarthy, J. K., Agüeros, M. A., et al. 2009, ApJS, 182, 543

Allamandola, L. J., Tielens, A. G. G. M., & Barker, J. R. 1985, ApJ, 290, L25

Antonucci, R. 1993, ARA&A, 31, 473

Antonucci, R. R. J., & Miller, J. S. 1985, ApJ, 297, 621

Bohren, C. F. & Huffman, D. R. 1983, Absorption and scattering of light by small particles, Wiley

Boroson, T. A., & Green, R. F. 1992, ApJS, 80, 109

Chiar, J. E., & Tielens, A. G. G. M. 2006, ApJ, 637, 774

Cutri, R. M., Nelson, B.O., Kirkpatrick, J.D., Huchra, J.P. & Smith, P.S. 2001, in ASP Conf. Ser. 232: The New Era of Wide Field Astronomy, ed. R. Clowes, A. Adamson, & G. Bromage (San Francisco, CA: ASP), 78

Czerny, B., Li, J., Loska, Z., & Szczerba, R. 2004, MNRAS, 348, 54

Dasyra, K. M., Ho, L. C., Netzer, H., et al. 2011, ApJ, 740, 94

Draine, B. T., & Lee, H. M. 1984, ApJ, 285, 89

Dong, X.-B., Ho, L. C., Wang, J.-G., et al. 2010, ApJ, 721, L143

Dorschner, J., Begemann, B., Henning, T., Jaeger, C., & Mutschke, H. 1995, A&A, 300, 503

Du, P., Hu, C., Lu, K.-X., et al. 2014, ApJ, 782, 45

Elitzur, M. 2006, New Astro. Rev., 50, 728

Elitzur, M., & Shlosman, I. 2006, ApJ, 648, L101

Gaskell, C. M., Goosmann, R. W., Antonucci, R. R. J., & Whysong, D. H. 2004, ApJ, 616, 147

Greene, J. E., Ho, L. C., & Barth, A. J. 2008, ApJ, 688, 159

Goldschmidt, P., Miller, L., La Franca, F., & Cristiani, S. 1992, MNRAS, 256, 65P

Hao, L., Spoon, H. W. W., Sloan, G. C., et al. 2005a, ApJ, 625, L75

Hao, L., Strauss, M. A., Tremonti, C. A., et al. 2005b, AJ, 129, 1783

Hao, L., Weedman, D. W., Spoon, H. W. W., et al. 2007, ApJ, 655, L77

Henning, T. 2010, ARA&A, 48, 21

Ho, L. C., & Kim, M. 2014, ApJ, 789, 17

Hönig, S. F., & Kishimoto, M. 2010, A&A, 523, A27

Houck, J. R., Roellig, T. L., van Cleve, J., et al. 2004, ApJS, 154, 18

Jaffe, W., Meisenheimer, K., Röttgering, H. J. A., et al. 2004, Nature, 429, 47

Jester, S., Schneider, D. P., Richards, G. T., et al. 2005, AJ, 130, 873

Kaspi, S., Smith, P. S., Netzer, H., et al. 2000, ApJ, 533, 631

Kemper, F., Vriend, W. J., & Tielens, A. G. G. M. 2004, ApJ, 609, 826

Markwick-Kemper, F., Gallagher, S. C., Hines, D. C., & Bouwman, J. 2007, ApJ, 668, L107

Köhler, M., & Li, A. 2010, MNRAS, 406, L6

Laor, A., & Draine, B. T. 1993, ApJ, 402, 441

Lebouteiller, V., Barry, D. J., Spoon, H. W. W., et al. 2011, ApJS, 196, 8

Leger, A., & Puget, J. L. 1984, A&A, 137, L5

Li, A. 2004, in Penetrating Bars Through Masks of Cosmic Dust: The Hubble Tuning Fork Strikes a New Note, ed. D.L. Block, I. Puerari, K.C. Freeman, R. Groess, & E.K. Block (Dordrecht: Kluwer) 535

Li, A. 2007, in The Central Engine of Active Galactic Nuclei (ASP Conf. Ser. 373), ed. L. C. Ho & J.-M. Wang (San Francisco, CA: ASP), 561

Li, A. 2009, in Small Bodies in Planetary Sciences (Lecture Notes in Physics vol. 758), ed. I. Mann, A. Nakamura, & T. Mukai, Springer, Chapter 6, 167

Li, A., & Draine, B. T. 2001, ApJ, 554, 778

Li, M. P., Shi, Q. J., & Li, A. 2008, MNRAS, 391, L49

Lumsden, S. L., Alexander, D. M., & Hough, J. H. 2004, MNRAS, 348, 1451

Maiolino, R., Marconi, A., & Oliva, E. 2001, A&A, 365, 37

Mason, R. E. 2015, Planet. Space Sci., 116, 97

Mason, R. E., Wright, G., Pendleton, Y., & Adamson, A. 2004, ApJ, 613, 770

Mason, R. E., Geballe, T. R., Packham, C., et al. 2006, ApJ, 640, 612

Mason, R. E., Levenson, N. A., Shi, Y., et al. 2009, ApJ, 693, L136

Mishra, A., & Li, A. 2015, ApJ, 809, 120

Markwardt, C. B. 2009, Astronomical Data Analysis Software and Systems XVIII, 411, 251

Marziani, P., Sulentic, J. W., Zamanov, R., et al. 2003, ApJS, 145, 199

Nenkova, M., Sirocky, M. M., Ivezić, Ž., & Elitzur, M. 2008, ApJ, 685, 147

Nenkova, M., Sirocky, M. M., Nikutta, R., Ivezić, Ž., & Elitzur, M. 2008, ApJ, 685, 160

Neugebauer, G., Green, R. F., Matthews, K., et al. 1987, ApJS, 63, 615

Nikutta, R., Elitzur, M., & Lacy, M. 2009, ApJ, 707, 1550

Ossenkopf, V., Henning, T., & Mathis, J. S. 1992, A&A, 261, 567

Rhee, J. H., & Larkin, J. E. 2006, ApJ, 640, 625

Richards, G. T., Hall, P. B., Vanden Berk, D. E., et al. 2003, AJ, 126, 1131

Rieke, G. H., & Low, F. J. 1975, ApJ, 199, L13

Roche, P. F., Aitken, D. K., Smith, C. H., & Ward, M. J. 1991, MNRAS, 248, 606

Roche, P. F., Packham, C., Aitken, D. K., & Mason, R. E. 2007, MNRAS, 375, 99

Rose, M., Tadhunter, C. N., Holt, J., & Rodríguez Zaurín, J. 2013, MNRAS, 432, 2150

Rouleau, F., & Martin, P. G. 1991, ApJ, 377, 526

Rowan-Robinson, M. 1995, MNRAS, 272, 737

Sani, E., Lutz, D., Risaliti, G., et al. 2010, MNRAS, 403, 1246

Schartmann, M., Meisenheimer, K., Camenzind, M., et al. 2008, A&A, 482, 67

Schmidt, M., & Green, R. F. 1983, ApJ, 269, 352

Siebenmorgen, R., Krügel, E., & Spoon, H. W. W. 2004, A&A, 414, 123

Siebenmorgen, R., Haas, M., Krügel, E., & Schulz, B. 2005, A&A, 436, L5

Shen, Y., Richards, G. T., Strauss, M. A., et al. 2011, ApJS, 194, 45

Shi, Y., Rieke, G. H., Ogle, P. M., Su, K. Y. L., & Balog, Z. 2014, ApJS, 214, 23

Smith, P. S., Schmidt, G. D., Hines, D. C., Cutri, R. M., & Nelson, B. O. 2002, ApJ, 569, 23

Smith, H. A., Li, A., Li, M. P., et al. 2010, ApJ, 716, 490

Sturm, E., Schweitzer, M., Lutz, D., et al. 2005, ApJ, 629, L21

Sturm, E., Rupke, D., Contursi, A., et al. 2006, ApJ, 653, L13

Trichas, M., Green, P. J., Constantin, A., et al. 2013, ApJ, 778, 188

Tristram, K. R. W., Meisenheimer, K., Jaffe, W., et al. 2007, A&A, 474, 837

Urry, C. M., & Padovani, P. 1995, PASP, 107, 803

Vestergaard, M., & Peterson, B. M. 2006, ApJ, 641, 689

Voit, G. M. 1991, ApJ, 379, 122

Voit, G. M. 1992, MNRAS, 258, 841

Wandel, A., Peterson, B. M., & Malkan, M. A. 1999, ApJ, 526, 579

Wang, J.-M., & Zhang, E.-P. 2007, ApJ, 660, 1072

Woo, J.-H., Kim, J. H., Imanishi, M., & Park, D. 2012, AJ, 143, 49

Wu, X.-B., & Liu, F. K. 2004, ApJ, 614, 91

Xie, Y., Hao, L., & Li, A. 2014, ApJ, 794, L19

Xie, Y., Li, A., Hao, L., & Nikutta, R. 2015, ApJ, 808, 145

Xie, Y., Nikutta, R., Hao, L., & Li, A. 2016, Planet. Space Sci., 133, 23 (arXiv:1605.06999)

Zhu, L., Zhang, S. N., & Tang, S. 2009, ApJ, 700, 1173

Zhang, Z., Shi, Y., Rieke, G. H., et al. 2016, ApJ, 819, L27

This preprint was prepared with the AAS LaTeX macros v5.2.

Table 1. Model Parameters for 93 AGNs Showing Silicate Emission around 9.7 and 18 $\mu$m

| Source | $T_w^S$ (K) | $M_w^S$ ($M_\odot$) | $T_c^S$ (K) | $M_c^S$ ($M_\odot$) | $T_w^G$ (K) | $M_w^G$ ($M_\odot$) | $T_c^G$ (K) | $M_c^G$ ($M_\odot$) |
|---|---|---|---|---|---|---|---|---|
| (1) | (2) | (3) | (4) | (5) | (6) | (7) | (8) | (9) |
| PG0003+158 | 358.00±73.60 | 4.32E1 ± 2.00E1 | 174.33±7.98 | 2.53E3 ± 1.64E2 | 790.57±59.82 | 8.64±4.00 | 182.83±3.77 | 5.06E3 ± 3.28E2 |
| PG0003+199 | 317.95±1.06 | 2.77 ± 5.71E-2 | 40.00 ± 3.10 | 1.42E3 ± 2.51E1 | 744.55±4.43 | 5.54E-1±1.14E-2 | 187.60 ± 0.66 | 2.84E2 ± 5.05 |
| PG0026+129 | 203.95±2.70 | 1.32E1 ± 2.59E-1 | 193.68 ± 0.69 | 2.72E2 ± 6.92 | 671.86±3.34 | 2.65E0±5.18E-2 | 206.22 ± 0.68 | 4.95E2 ± 2.31E1 |
| PG0043+039 | 482.21 ± 17.11 | 3.17E1 ± 3.67 | 40.00 ± 0.00 | 4.45E4 ± 2.46E3 | 884.88±3.94 | 7.84E0±1.27 | 149.29 ± 0.79 | 1.47E4 ± 1.20E3 |
| PG0049+171 | 184.14±1.05 | 8.60E-1 ± 1.24E-1 | 184.20 ± 1.06 | 2.25E1 ± 5.85E-1 | 683.54 ± 12.93 | 1.72E-1±4.18E-2 | 219.69 ± 0.82 | 4.44E1 ± 1.92 |
| PG0050+124 | 410.84±3.06 | 1.64E1 ± 4.40E-1 | 68.29 ± 0.06 | 2.65E4 ± 1.32E3 | 545.32 ±1.11 | 1.42E1±5.17E-1 | 143.54 ± 0.16 | 1.17E4 ± 8.64E2 |
| PG0052+251 | 171.76±2.23 | 2.40E1 ± 5.78 | 173.53 ± 2.55 | 5.15E2 ± 3.78E1 | 565.33 ± 10.01 | 5.44E0±5.27 | 208.04 ± 1.59 | 9.25E2 ± 1.14E2 |
| PG0804+761 | 407.53±1.43 | 1.86E1 ± 1.98E-1 | 40.00 ± 0.00 | 1.70E4 ± 4.92E1 | 819.90 ±2.87 | 3.72E0±3.97E-2 | 164.88 ± 0.12 | 3.41E3 ± 9.86 |
| PG0844+349 | 338.14±2.85 | 5.86 ± 1.66E-1 | 113.33 ± 0.60 | 6.03E2 ± 2.17E1 | 699.13 ±5.87 | 1.17E0±3.32E-2 | 161.88 ± 0.41 | 5.42E2 ± 3.11E1 |
| PG0921+525 | 182.74±0.28 | 3.14E-1 ± 7.68E-3 | 182.81 ± 0.23 | 3.74E1 ± 2.66E-1 | 1131.80 ± 11.20 | 6.28E-2±1.58E-3 | 210.67 ± 0.19 | 6.16E1 ± 7.91E-1 |
| PG0923+201 | 380.40±8.37 | 2.74E1 ± 2.12 | 40.00 ± 0.00 | 2.13E4 ± 3.82E2 | 797.53 ±6.90 | 5.93E0±6.41E-1 | 154.97 ± 0.45 | 4.37E3 ± 1.20E2 |
| PG0947+396 | 266.70±3.48 | 5.09E1 ± 2.32 | 63.40 ± 1.72 | 2.57E4 ± 4.82E2 | 657.53 ±4.39 | 1.02E1±5.84E-1 | 155.23 ± 0.45 | 5.14E3 ± 1.47E2 |
| PG0953+414 | 340.04±5.05 | 3.66E1 ± 1.42 | 40.00 ± 0.00 | 1.93E4 ± 8.95E2 | 842.36 ± 10.77 | 7.33E0±2.83E-1 | 168.92 ± 0.79 | 4.10E3 ± 2.31E2 |
| PG1001+054 | 290.92±9.86 | 1.82E1 ± 2.80 | 71.50 ± 3.89 | 9.85E3 ± 6.15E2 | 735.20 ± 24.25 | 3.63E0±5.61E-1 | 160.26 ± 1.94 | 1.97E3 ± 1.23E2 |
| PG1004+130 | 468.54±3.29 | 4.54E1 ± 9.22E-1 | 40.00 ± 0.00 | 3.86E4 ± 4.71E2 | 698.83 ±3.42 | 9.09E0±1.84E-1 | 146.45 ± 0.21 | 1.51E4 ± 2.87E2 |
| PG1011-040 | 308.07±1.50 | 5.34 ± 1.00E-1 | 71.55 ± 0.64 | 3.08E3 ± 3.22E1 | 611.19 ±3.07 | 1.07E0±2.01E-2 | 161.83 ± 0.32 | 6.17E2 ± 6.45 |
| PG1012+008 | 373.64 ± 13.91 | 1.22E1 ± 1.74 | 70.35 ± 0.88 | 2.29E4 ± 1.69E3 | 608.69 ±4.53 | 1.06E1±2.04 | 157.00 ± 0.51 | 4.58E3 ± 6.27E2 |
| PG1048-090 | 361.13 ± 62.98 | 1.80E1 ± 6.59 | 176.05 ± 6.21 | 1.34E3 ± 1.32E2 | 893.65 ± 63.66 | 3.59E0±1.32 | 184.11 ± 2.88 | 2.68E3 ± 3.31E2 |
| PG1049-005 | 288.49±5.18 | 2.57E2 ± 2.02E1 | 72.93 ± 0.99 | 2.33E5 ± 5.33E3 | 633.50 ±1.73 | 5.93E1±6.37 | 148.37 ± 0.49 | 4.66E4 ± 1.07E3 |
| PG1048+342 | 150.00 ± 29.39 | 1.15E1 ± 4.29 | 143.79 ± 50.92 | 3.80E2 ± 2.04E2 | 716.78 ± 11.33 | 2.31E0±8.24 | 185.77 ± 4.41 | 7.60E2 ± 4.25E2 |
| PG1100+772 | 349.45±4.07 | 6.98E1 ± 2.22 | 40.00 ± 12.94 | 6.06E3 ± 3.06E2 | 754.47 ±7.05 | 1.40E1±4.43E-1 | 163.32 ± 1.24 | 9.94E3 ± 8.30E2 |
| PG1103-006 | 387.23 ± 13.03 | 8.87E1 ± 7.85 | 117.73 ± 8.59 | 7.08E3 ± 7.01E2 | 763.72 ± 17.04 | 1.77E1±1.57 | 163.36 ± 1.82 | 1.42E4 ± 1.40E3 |
| PG1114+445 | 262.72±2.61 | 2.93E1 ± 5.88E-1 | 143.85 ± 1.88 | 1.57E3 ± 8.30E1 | 667.64 ±3.48 | 5.87E0±1.18E-1 | 182.72 ± 0.30 | 2.90E3 ± 2.25E2 |
| PG1116+215 | 366.03±6.11 | 3.29E1 ± 1.52 | 40.00 ± 0.00 | 2.80E4 ± 9.90E3 | 902.47 ± 15.08 | 6.59E0±3.04E-1 | 164.80 ± 0.54 | 5.80E3 ± 7.06E3 |
| PG1121+422 | 280.10±5.52 | 1.86E1 ± 7.36E-1 | 172.63 ± 3.21 | 2.83E2 ± 9.47 | 801.03 ±9.87 | 3.72E0±1.47E-1 | 181.64 ± 1.68 | 5.65E2 ± 1.89E1 |
| PG1151+117 | 332.48 ± 95.07 | 1.70E1 ± 1.09E1 | 40.00 ± 9.65 | 9.87E3 ± 2.35E3 | 725.01 ± 72.48 | 3.40E0±7.46 | 158.87 ± 3.43 | 2.02E3 ± 2.07E3 |
| PG1202+281 | 320.80±1.82 | 2.91E1 ± 5.72E-1 | 47.34 ± 2.63 | 3.09E4 ± 1.51E2 | 644.61 ±3.43 | 5.83E0±1.14E-1 | 151.39 ± 0.17 | 6.18E3 ± 3.02E1 |
| PG1211+143 | 267.00±4.38 | 3.99E1 ± 2.28 | 118.08 ± 0.68 | 1.28E3 ± 4.38E1 | 632.66 ± 10.45 | 7.99E0±4.56E-1 | 167.74 ± 0.36 | 2.45E3 ± 1.17E2 |
| PG1216+069 | 315.83 ± 67.65 | 2.68E1 ± 2.13 | 148.30 ± 27.37 | 1.38E3 ± 6.14E2 | 814.50 ± 15.37 | 5.38E0±4.51E-1 | 204.81 ± 5.60 | 2.19E3 ± 1.07E3 |
| PG1229+204 | 276.58±5.27 | 3.94 ± 2.56E-1 | 115.50 ± 0.41 | 5.63E2 ± 2.02 | 696.31 ± 10.99 | 7.89E-1±5.13E-2 | 161.76 ± 0.11 | 1.13E3 ± 4.03 |
| PG1259+593 | 431.78±4.93 | 3.94E1 ± 1.63 | 117.00 ± 4.31 | 9.87E3 ± 1.87E3 | 1014.46 ±7.85 | 7.88E0±4.16E-1 | 226.28 ± 1.54 | 2.36E3 ± 6.97E2 |
| PG1302-102 | 324.63±2.81 | 1.23E2 ± 3.97 | 55.72 ± 1.44 | 1.11E5 ± 6.85E2 | 653.52 ±2.95 | 2.46E1±1.08 | 155.28 ± 0.20 | 2.22E4 ± 1.37E2 |
| PG1307+085 | 161.35±3.15 | 1.87E1 ± 5.40 | 161.47 ± 3.09 | 8.20E2 ± 9.29E1 | 708.55 ± 27.93 | 3.73E0±8.96 | 185.39 ± 1.91 | 1.43E3 ± 2.59E2 |
| PG1309+355 | 441.88 ± 118.63 | 1.50E1 ± 5.49E1 | 105.79 ± 1.67 | 9.14E3 ± 3.75E3 | 658.17 ± 68.58 | 1.18E1±4.37E1 | 167.12 ± 8.80 | 5.37E3 ± 5.52E3 |
| PG1310-108 | 160.55±0.49 | 1.00 ± 2.31E-2 | 160.64 ± 0.32 | 6.96E1 ± 8.27E-1 | 679.46 ±4.40 | 2.00E-1±4.62E-3 | 199.48 ± 0.19 | 1.03E2 ± 2.03 |
| PG1322+659 | 266.61±1.67 | 2.94E1 ± 4.52E-1 | 51.66 ± 1.37 | 1.85E4 ± 1.11E2 | 676.31 ±3.00 | 5.89E0±9.04E-2 | 151.36 ± 0.20 | 3.70E3 ± 2.21E1 |
| PG1341+258 | 284.24±2.73 | 5.82 ± 1.70E-1 | 58.28 ± 0.85 | 4.45E3 ± 3.63E1 | 658.15 ±5.67 | 1.16E0±3.40E-2 | 152.81 ± 0.27 | 8.90E2 ± 7.25 |
| PG1351+640 | 351.66±0.60 | 4.59E1 ± 2.74E-1 | 84.16 ± 0.38 | 7.07E3 ± 2.18E1 | 540.18 ±1.75 | 9.88E0±1.30E-1 | 133.05 ± 0.07 | 1.41E4 ± 4.37E1 |
| PG1352+183 | 248.21 ± 25.87 | 5.38E1 ± 3.09E1 | 40.00 ± 1.97 | 6.43E3 ± 1.36E3 | 335.40 ± 86.50 | 1.08E1±6.19 | 161.73 ± 5.22 | 1.29E3 ± 5.77E2 |
| PG1402+261 | 403.94±8.90 | 1.98E1 ± 1.58 | 69.50 ± 0.24 | 5.03E4 ± 5.33E2 | 661.52 ±5.08 | 1.38E1±1.57 | 142.40 ± 0.36 | 1.01E4 ± 1.07E2 |
| PG1404+226 | 315.15±5.32 | 3.37 ± 2.28E-1 | 64.89 ± 0.50 | 2.53E3 ± 2.80E1 | 600.81 ±4.64 | 1.69E0±1.59E-1 | 161.12 ± 0.43 | 5.07E2 ± 5.60 |
| PG1411+442 | 265.36 ± 17.48 | 2.35E1 ± 8.18 | 59.66 ± 2.18 | 7.16E3 ± 1.37E2 | 721.91 ± 49.45 | 4.70E0±1.65 | 171.08 ± 1.53 | 1.43E3 ± 2.75E1 |
| PG1416-129 | 183.99 ± 19.61 | 3.69E-1 ± 1.47 | 172.33 ± 1.38 | 1.54E2 ± 2.75 | 924.34 ± 29.30 | 7.38E-1±2.95 | 202.23 ± 0.96 | 3.08E2 ± 5.49 |
| PG1426+015 | 330.84±2.55 | 9.90 ± 2.96E-1 | 61.10 ± 0.13 | 1.33E4 ± 3.35E1 | 640.93 ±2.12 | 5.92E0±2.41E-1 | 163.35 ± 0.11 | 2.66E3 ± 6.71 |
| PG1435-067 | 319.81±3.71 | 9.28 ± 5.78E-1 | 40.00 ± 30.10 | 7.73E2 ± 1.09E2 | 729.28 ± 14.00 | 1.86E0±1.16E-1 | 182.86 ± 4.48 | 7.92E2 ± 1.23E2 |
| PG1444+407 | 434.56±6.63 | 2.75E1 ± 1.57 | 65.56 ± 0.92 | 4.88E4 ± 5.13E2 | 662.35 ±2.16 | 1.68E1±1.30 | 161.15 ± 0.36 | 9.77E3 ± 1.03E2 |
| PG1512+370 | 367.38±4.50 | 4.52E1 ± 1.80 | 90.10 ± 0.84 | 2.75E4 ± 6.92E2 | 818.86 ±5.81 | 9.26E0±5.43E-1 | 184.86 ± 0.85 | 5.50E3 ± 1.38E2 |
| PG1534+580 | 240.61 ± 31.24 | 1.59 ± 8.29 | 128.85 ± 43.61 | 1.07E2 ± 1.60E2 | 694.01 ± 85.59 | 3.18E-1±1.66 | 170.48 ± 6.01 | 2.14E2 ± 3.22E2 |
| PG1535+547 | 239.98±0.79 | 2.23 ± 1.89E-2 | 49.95 ± 0.54 | 6.48E2 ± 7.14E1 | 776.61 ±2.20 | 4.46E-1±3.78E-3 | 183.34 ± 0.15 | 1.30E2 ± 4.26E1 |

Table 1—Continued

| Source | $T_w^S$ (K) | $M_w^S$ ($M_\odot$) | $T_c^S$ (K) | $M_c^S$ ($M_\odot$) | $T_w^G$ (K) | $M_w^G$ ($M_\odot$) | $T_c^G$ (K) | $M_c^G$ ($M_\odot$) |
|---|---|---|---|---|---|---|---|---|
| (1) | (2) | (3) | (4) | (5) | (6) | (7) | (8) | (9) |
| PG1545+210 | 173.68 ± 38.91 | 2.39E1 ± 1.04E1 | 172.48 ± 3.50 | 7.86E2 ± 2.87E1 | 857.38 ± 19.41 | 4.84E0±1.92E1 | 199.93 ± 1.23 | 1.57E3 ± 7.94E1 |
| PG1552+085 | 401.77 ± 61.66 | 1.67 ± 6.81 | 72.47 ± 1.39 | 2.93E3 ± 9.96E1 | 602.90 ± 16.89 | 3.34E0±1.37E1 | 173.79 ± 0.89 | 5.87E2 ± 1.99E1 |
| PG1617+175 | 339.70 ± 26.44 | 1.25E1 ± 6.77 | 53.90 ± 2.02 | 5.92E3 ± 2.25E2 | 757.72 ± 55.33 | 2.50E0±1.36 | 163.43 ± 2.53 | 1.18E3 ± 4.50E1 |
| PG1626+554 | 314.90 ± 20.66 | 3.68 ± 1.27 | 225.05 ± 5.27 | 6.18E1 ± 5.03 | 834.28 ± 77.72 | 7.35E-1±1.01 | 214.70 ± 2.58 | 1.24E2 ± 1.37E1 |
| PG1700+518 | 365.49±8.00 | 1.43E2 ± 9.85 | 76.48 ± 0.34 | 2.07E5 ± 2.29E3 | 640.92 ±7.26 | 7.55E1±7.23 | 153.06 ± 0.34 | 4.14E4 ± 4.58E2 |
| PG1704+608 | 395.20±2.70 | 1.16E2 ± 2.15 | 40.00 ± 0.00 | 1.93E5 ± 6.08E3 | 837.88 ±4.76 | 2.31E1±4.31E-1 | 138.84 ± 0.19 | 8.70E4 ± 3.76E3 |
| PG2112+059 | 352.84±2.46 | 2.15E2 ± 8.04 | 100.75 ± 2.60 | 8.25E4 ± 8.20E3 | 819.08 ±3.03 | 4.71E1±2.20 | 190.72 ± 2.63 | 1.65E4 ± 1.64E3 |
| PG2209+184 | 288.22±2.85 | 3.16 ± 9.52E-2 | 60.48 ± 1.03 | 8.10E2 ± 1.07E1 | 716.31 ±6.56 | 6.32E-1±1.90E-2 | 176.17 ± 0.62 | 1.62E2 ± 2.14 |
| PG2214+139 | 314.14±1.03 | 7.78 ± 8.73E-2 | 51.91 ± 1.17 | 6.18E2 ± 9.14E1 | 827.31 ±3.17 | 1.56E0±1.75E-2 | 182.26 ± 0.18 | 5.02E2 ± 1.05E2 |
| PG2233+134 | 253.00 ± 26.06 | 1.55E2 ± 2.18E1 | 143.65 ± 4.18 | 5.98E3 ± 2.95E2 | 592.41 ± 15.16 | 3.11E1±4.93 | 155.43 ± 1.25 | 1.20E4 ± 5.89E2 |
| PG2251+113 | 334.92 ± 34.85 | 5.47E1 ± 8.93E1 | 40.00 ± 26.51 | 3.00E3 ± 2.09E2 | 735.66 ± 100.48 | 1.09E1±1.79E1 | 183.65 ± 7.21 | 6.01E3 ± 4.17E2 |
| PG2304+042 | 150.00 ± 17.07 | 5.04E-2 ± 3.08E-1 | 194.77 ± 1.46 | 1.22E1 ± 6.53E-1 | 1500.00 ± 356.30 | 1.20E-2±8.08E-2 | 217.36 ± 4.98 | 2.44E1 ± 1.31 |
| PG2308+098 | 197.34 ± 12.19 | 4.42 ± 1.14E1 | 197.39 ± 0.72 | 1.67E3 ± 3.68E1 | 871.36 ± 12.40 | 8.84E0±2.29E1 | 192.43 ± 1.63 | 3.34E3 ± 7.36E1 |
| 2MASSiJ081652.2+425829 | 319.66 ± 19.84 | 1.48E1 ± 5.86 | 40.00 ± 35.45 | 3.71E3 ± 1.42E3 | 719.47 ± 65.88 | 2.96E0±1.17 | 176.42 ± 18.26 | 7.64E2 ± 7.09E2 |
| 2MASSiJ095504.5+170556 | 178.45 ± 40.51 | 7.34 ± 3.20 | 172.85 ± 5.58 | 1.64E2 ± 8.58 | 731.20 ± 19.56 | 1.47E0±6.04 | 181.01 ± 1.92 | 3.27E2 ± 2.05E1 |
| 2MASSiJ130005.3+163214 | 150.00±0.00 | 1.74E1 ± 3.99 | 137.78 ± 2.74 | 5.40E2 ± 4.89E1 | 715.68 ± 14.96 | 3.48E0±7.52 | 189.57 ± 0.51 | 9.41E2 ± 1.26E2 |
| 2MASSiJ132917.5+121340 | 255.49 ± 82.96 | 2.08E1 ± 9.70 | 81.99 ± 9.98 | 3.25E3 ± 8.51E2 | 562.71 ± 37.76 | 5.22E0±9.53 | 179.31 ± 8.73 | 6.49E2 ± 1.70E2 |
| 2MASSiJ1402511+263117 | 191.28 ± 27.29 | 2.33 ± 8.62 | 156.37 ± 9.90 | 3.51E2 ± 3.52E1 | 729.98 ± 14.12 | 4.65E0±1.73E1 | 197.07 ± 2.02 | 7.01E2 ± 7.56E1 |
| 2MASSiJ145608.6+275008 | 330.00 ± 63.97 | 2.58E1 ± 5.95E1 | 84.98 ± 15.50 | 1.72E4 ± 1.34E4 | 698.81 ± 95.40 | 8.58E0±2.04E1 | 164.89 ± 13.87 | 3.44E3 ± 2.67E3 |
| 2MASSiJ151653.2+190048 | 323.31 ± 12.31 | 1.03E2 ± 1.58E1 | 40.00 ± 0.00 | 4.75E4 ± 6.65E2 | 683.70 ±6.98 | 2.86E1±6.09 | 156.70 ± 0.76 | 1.02E4 ± 1.49E2 |
| 2MASSiJ151901.5+183804 | 350.92 ± 23.98 | 4.37 ± 9.66E-1 | 83.62 ± 3.96 | 3.59E3 ± 4.69E2 | 821.46 ± 59.21 | 8.74E-1±2.51E-1 | 158.54 ± 3.72 | 7.18E2 ± 9.39E1 |
| 2MASSiJ154307.7+193751 | 246.49 ± 36.20 | 1.63E2 ± 3.89E1 | 40.00 ± 0.00 | 5.70E4 ± 7.63E3 | 597.44 ± 20.57 | 3.25E1±3.81E1 | 152.52 ± 1.94 | 1.14E4 ± 3.35E3 |
| 2MASSiJ222221.1+195947 | 312.89±6.62 | 3.64E1 ± 2.55 | 40.00 ± 0.00 | 2.03E4 ± 2.51E2 | 719.87 ± 13.54 | 7.29E0±5.11E-1 | 166.80 ± 0.58 | 4.07E3 ± 5.03E1 |
| 2MASSiJ223742.6+145614 | 262.58 ± 11.27 | 6.18E1 ± 7.75 | 71.60 ± 24.54 | 2.63E4 ± 8.85E3 | 586.67 ± 18.74 | 1.24E1±1.55 | 144.68 ± 9.83 | 5.25E3 ± 1.77E3 |
| 2MASSiJ234259.3+134750 | 338.21 ± 50.33 | 3.61E1 ± 1.94E1 | 96.94 ± 5.53 | 1.95E4 ± 3.72E3 | 606.38 ± 67.85 | 7.22E0±3.88 | 146.57 ± 6.14 | 3.90E3 ± 1.17E3 |
| 2MASSiJ234449.5+122143 | 296.00 ± 40.78 | 3.96E1 ± 1.77E1 | 71.45 ± 2.01 | 4.13E4 ± 2.45E3 | 625.95 ± 31.90 | 9.22E0±4.26 | 144.47 ± 1.91 | 8.25E3 ± 4.89E2 |
| 2MASXJ09210862+4538575 | 219.07 ± 49.13 | 6.97 ± 8.66 | 163.39 ± 9.07 | 1.55E2 ± 1.96E1 | 666.39 ± 131.72 | 1.39E0±4.00 | 200.06 ± 7.72 | 3.10E2 ± 4.21E1 |
| 2MASXJ00370409-0109081 | 295.44 ± 32.02 | 1.20 ± 3.08E-1 | 127.84 ± 37.46 | 1.89E1 ± 7.88 | 637.13 ± 52.61 | 2.39E-1±8.98E-2 | 178.78 ± 3.99 | 3.78E1 ± 1.61E1 |
| 2MASXJ02335161+0108136 | 634.16 ± 198.50 | 1.18E-2 ± 4.37E-3 | 64.09 ± 0.66 | 1.10E2 ± 7.82 | 1288.37 ± 140.98 | 2.35E-3±1.08E-3 | 132.70 ± 2.15 | 2.21E1 ± 1.56 |
| 2MASXJ07582810+3747121 | 345.77 ± 106.23 | 8.08E-2 ± 1.84E-1 | 58.13 ± 23.66 | 5.79E1 ± 4.24E1 | 931.25 ± 185.08 | 2.20E-2±5.18E-2 | 152.34 ± 11.18 | 2.93E1 ± 4.80E1 |
| 2MASXiJ0208238-002000 | 236.18±8.17 | 5.12 ± 6.54E-1 | 126.35 ± 8.32 | 9.27E1 ± 2.88E1 | 492.74 ± 17.14 | 1.02E0±1.31E-1 | 168.73 ± 2.05 | 1.85E2 ± 6.52E1 |
| 2MASXJ02061600-0017292 | 296.29±3.04 | 3.39 ± 1.13E-1 | 58.80 ± 4.61 | 5.57E2 ± 1.95E2 | 746.93 ±7.76 | 6.79E-1±2.25E-2 | 175.24 ± 0.81 | 1.87E2 ± 8.45E1 |
| 2MASXJ10493088+2257523 | 150.00 ± 10.34 | 1.22E-1 ± 3.72E-1 | 139.69 ± 9.98 | 1.04E2 ± 4.15 | 712.89 ±8.52 | 2.45E-1±7.50E-1 | 173.89 ± 0.57 | 2.08E2 ± 8.30 |
| 2MASXJ12485992-0109353 | 301.01±5.02 | 2.33E1 ± 1.59 | 42.06 ± 1.43 | 3.54E4 ± 2.62E2 | 490.22 ±6.89 | 4.66E0±3.18E-1 | 136.12 ± 0.29 | 7.07E3 ± 5.26E1 |
| 2MASXJ14070036+2827141 | 334.20±2.02 | 4.63E1 ± 9.03E-1 | 62.77 ± 0.08 | 5.47E4 ± 2.11E2 | 581.09 ±2.49 | 9.27E0±1.81E-1 | 134.13 ± 0.14 | 1.09E4 ± 4.23E1 |
| 2MASXJ02143357-0046002 | 267.91±3.67 | 2.45 ± 1.31E-1 | 56.11 ± 0.49 | 2.10E3 ± 1.18E1 | 539.30 ±6.50 | 4.89E-1±2.62E-2 | 153.40 ± 0.25 | 4.20E2 ± 2.36 |
| 2MASXJ09234300+2254324 | 237.82±4.77 | 6.93 ± 8.41E-1 | 112.27 ± 3.56 | 1.38E2 ± 3.10E1 | 575.01 ± 13.89 | 1.39E0±1.68E-1 | 171.89 ± 0.95 | 2.77E2 ± 6.95E1 |
| 2MASXJ12170991+0711299 | 302.86 ± 26.60 | 5.82E-2 ± 2.24E-1 | 57.72 ± 3.07 | 6.02E1 ± 1.30E1 | 566.17 ± 47.07 | 3.81E-2±1.47E-1 | 143.98 ± 13.98 | 1.20E1 ± 1.37E1 |
| 2MASXJ12232410+0240449 | 270.26 ± 29.61 | 4.20E-1 ± 7.78E-2 | 170.29 ± 9.67 | 5.35 ± 9.59E-1 | 710.58 ± 31.95 | 8.39E-2±1.56E-2 | 190.11 ± 1.87 | 1.07E1 ± 2.27 |
| 2MASXJ13381586+0432330 | 370.52±4.78 | 5.01E-1 ± 2.07E-2 | 63.94 ± 0.22 | 3.38E2 ± 9.51 | 985.22 ± 15.52 | 1.00E-1±4.15E-3 | 159.66 ± 0.33 | 1.22E2 ± 4.98 |
| 2MASXJ13495283+0204456 | 207.83±4.27 | 2.52 ± 1.09E-1 | 129.11 ± 1.38 | 4.83E1 ± 7.08E-1 | 534.18 ±5.39 | 5.04E-1±2.18E-2 | 168.67 ± 0.53 | 9.65E1 ± 1.42 |
| 2MASXJ23044349-0841084 | 295.60±1.63 | 5.41 ± 9.96E-2 | 62.65 ± 0.12 | 6.90E3 ± 2.83E1 | 721.66 ±4.11 | 1.08E0±1.99E-2 | 150.29 ± 0.16 | 1.38E3 ± 5.65 |
| SDSSJ115138.24+004946.4 | 334.95 ± 148.97 | 3.62 ± 4.29 | 155.57 ± 7.42 | 1.77E2 ± 1.85E1 | 696.58 ± 154.45 | 7.23E-1±1.58 | 193.56 ± 6.91 | 3.54E2 ± 3.71E1 |
| SDSSJ170246.09+602818.8 | 325.32 ± 165.85 | 3.21E-1 ± 4.02E-1 | 51.97 ± 22.73 | 1.62E2 ± 6.62E1 | 512.92 ± 77.13 | 8.84E-2±2.60E-1 | 137.93 ± 7.20 | 3.85E1 ± 7.19E1 |

Table 2. Model Parameters for 30 AGNs Which Show No Silicate Emission but a Featureless Thermal Continuum

| Source | $T_w^S$ | $M_w^S$ | $T_c^S$ | $M_c^S$ | $T_w^G$ | $M_w^G$ | $T_c^G$ | $M_c^G$ |
|---|---|---|---|---|---|---|---|---|
| | (K) | ($M_\odot$) | (K) | ($M_\odot$) | (K) | ($M_\odot$) | (K) | ($M_\odot$) |
| (1) | (2) | (3) | (4) | (5) | (6) | (7) | (8) | (9) |
| PG0838+770 | 383.27 ± 23.92 | 4.53 ± 8.96E-1 | 65.69 ±0.16 | 6.98E3 ± 3.89E2 | 552.66 ±9.14 | 5.89 ± 1.19 | 150.94 ± 0.18 | 3.83E3 ± 3.02E2 |
| PG1226+023 | 245.43 ±0.53 | 3.09E2 ± 1.01 | 40.00 ±0.00 | 1.34E5 ± 2.51E3 | 686.41 ±0.65 | 6.18E1 ± 2.01E-1 | 152.17 ± 0.06 | 3.90E4 ± 1.13E3 |
| PG1354+213 | 521.75 ± 22.11 | 3.69 ± 5.67E-1 | 52.09 ±4.04 | 4.14E4 ± 9.19E2 | 713.85 ±5.54 | 7.39 ± 1.32 | 155.59 ± 0.39 | 8.28E3 ± 2.66E2 |
| PG1427+480 | 150.00 ± 75.01 | 1.44E1 ± 1.48E1 | 72.71 ±3.53 | 3.66E4 ± 3.27E3 | 624.51 ± 26.38 | 7.88 ± 8.23 | 149.61 ± 2.12 | 7.33E3 ± 6.55E2 |
| PG1448+273 | 239.30 ±1.20 | 5.19 ± 6.88E-2 | 40.00 ±0.00 | 3.74E3 ± 9.85 | 607.59 ±2.16 | 1.04 ± 1.38E-2 | 171.10 ± 0.10 | 7.50E2 ± 2.12 |
| PG1501+106 | 178.91 ±1.10 | 4.25 ± 5.59E-2 | 48.99 ±0.27 | 5.04E3 ± 6.90 | 606.14 ±2.14 | 8.51E-1 ± 1.12E-2 | 166.72 ± 0.06 | 1.01E3 ± 1.38 |
| PG1543+489 | 291.97 ±2.11 | 1.18E2 ± 2.60 | 85.60 ±0.15 | 1.98E5 ± 1.30E3 | 570.60 ±1.07 | 9.47E1 ± 2.86 | 163.69 ± 0.21 | 3.96E4 ± 2.60E2 |
| 2MASSiJ010835.1+214818 | 184.20 ± 10.74 | 1.68E2 ± 7.13 | 73.28 ±1.07 | 7.98E4 ± 1.53E3 | 599.78 ±6.37 | 3.35E1 ± 1.43 | 158.67 ± 0.71 | 1.60E4 ± 6.32E2 |
| 2MASSiJ024807.3+145957 | 150.00 ± 32.16 | 1.71E1 ± 3.71 | 70.70 ±1.11 | 6.23E3 ± 4.01E2 | 485.88 ± 23.01 | 4.75 ± 1.89 | 146.55 ± 2.27 | 1.25E3 ± 8.02E1 |
| 2MASSiJ082311.3+435318 | 150.00 ± 13.68 | 6.49E1 ± 1.09E1 | 74.37 ±2.94 | 2.76E4 ± 1.70E3 | 566.30 ± 24.85 | 1.30E1 ± 2.20 | 158.99 ± 2.54 | 5.75E3 ± 5.99E2 |
| 2MASSiJ145410.1+195648 | 150.00 ±0.52 | 8.04E1 ± 2.71E1 | 98.49 ± 25.43 | 2.98E3 ± 4.03E3 | 620.35 ± 21.97 | 1.61E1 ± 4.76E1 | 162.54 ± 3.15 | 3.54E3 ± 4.90E3 |
| 2MASXJ17223993+3052521 | 150.00 ±0.05 | 1.62 ± 2.77 | 64.56 ±3.48 | 2.82E3 ± 1.94E2 | 476.09 ± 15.79 | 1.53 ± 2.65 | 143.04 ± 2.05 | 5.63E2 ± 3.88E1 |
| 2MASXJ13130577+0127561 | 150.00 ± 37.35 | 2.55E-2 ± 5.32E-2 | 154.25 ± 30.08 | 3.13 ± 7.66E-1 | 813.23 ± 193.63 | 5.19E-3 ± 2.33E-2 | 170.28 ± 4.49 | 6.26 ± 1.58 |
| SDSSJ090738.71+564358.2 | 150.00 ±0.00 | 1.41 ± 7.77E-1 | 68.76 ±1.55 | 1.80E3 ± 2.63E2 | 433.34 ± 65.60 | 1.24 ± 9.42E-1 | 138.17 ± 5.04 | 3.60E2 ± 5.27E1 |
| 2MASXJ13130565-0210390 | 239.94 ± 21.18 | 1.79 ± 9.33E-1 | 59.06 ±1.65 | 1.00E3 ± 5.75E2 | 605.56 ± 13.36 | 8.50E-1 ± 5.75E-1 | 158.14 ± 0.96 | 4.29E2 ± 3.53E2 |
| SDSSJ124035.81-002919.4 | 234.95 ± 15.11 | 6.42 ± 3.82 | 47.57 ±4.20 | 4.77E3 ± 1.24E2 | 523.27 ± 27.32 | 1.28 ± 7.67E-1 | 144.28 ± 1.16 | 9.55E2 ± 2.50E1 |
| 2MASXJ15055659+0342267 | 260.53 ±2.21 | 3.37 ± 9.97E-2 | 60.44 ±0.18 | 3.39E3 ± 1.32E1 | 588.28 ±4.49 | 6.75E-1 ± 1.99E-2 | 151.76 ± 0.17 | 6.77E2 ± 2.63 |
| 2MASXJ09191322+5527552 | 237.54 ± 41.58 | 3.25 ± 7.86E-1 | 58.53 ±0.72 | 2.48E3 ± 1.98E1 | 565.31 ± 11.69 | 7.43E-1 ± 1.09 | 152.32 ± 0.48 | 4.96E2 ± 3.96 |
| SDSSJ101536.21+005459.3 | 150.00 ±0.00 | 1.92E1 ± 7.46E-1 | 137.51 ±1.52 | 4.15E2 ± 2.02E1 | 489.77 ±5.63 | 3.84 ± 1.49E-1 | 163.49 ± 0.46 | 8.29E2 ± 5.15E1 |
| SDSSJ164840.15+425547.6 | 150.00 ± 63.25 | 1.78 ± 5.35 | 62.28 ±5.46 | 3.68E3 ± 5.79E2 | 473.91 ± 36.12 | 1.58 ± 4.83 | 139.21 ± 4.10 | 7.36E2 ± 1.16E2 |
| SDSSJ091414.34+023801.7 | 186.93 ± 39.59 | 1.37 ± 2.68 | 63.66 ±7.25 | 1.43E3 ± 2.01E2 | 461.95 ± 51.19 | 4.55E-1 ± 9.29E-1 | 138.76 ± 4.10 | 2.87E2 ± 4.02E1 |
| 2MASXJ12384342+0927362 | 150.00 ±0.00 | 2.27E1 ± 2.26 | 106.73 ±1.92 | 1.25E3 ± 6.21E1 | 472.61 ±3.80 | 4.53 ± 4.10 | 151.59 ± 0.32 | 2.50E3 ± 1.58E2 |
| 2MASXJ16164729+3716209 | 172.57 ±7.27 | 7.62E1 ± 5.10 | 40.00 ± 25.60 | 5.73E3 ± 3.38E2 | 458.47 ±4.28 | 1.54E1 ± 1.39 | 140.99 ± 1.24 | 1.15E4 ± 6.76E2 |
| 2MASXJ11230133+4703088 | 265.83 ± 24.90 | 7.07E-2 ± 1.59E-2 | 59.62 ±1.05 | 1.23E2 ± 3.12 | 781.16 ± 65.83 | 1.41E-2 ± 3.18E-3 | 161.03 ± 1.10 | 2.46E1 ± 6.23E-1 |
| 2MASXJ11110693+0228477 | 150.00 ± 25.49 | 2.65 ± 4.10E-1 | 67.55 ±0.52 | 5.76E2 ± 1.15E1 | 467.19 ±7.51 | 7.11E-1 ± 2.17E-1 | 165.19 ± 1.31 | 1.15E2 ± 2.30 |
| 2MASSiJ1448250+355946 | 280.42 ±3.96 | 1.70E1 ± 1.25 | 68.10 ±0.23 | 9.34E3 ± 2.77E3 | 499.67 ±5.73 | 6.40 ± 7.16E-1 | 133.97 ± 0.62 | 6.25E3 ± 2.33E3 |
| SDSSJ164019.66+403744.4 | 150.00 ±2.41 | 6.47 ± 2.37E1 | 137.20 ±5.40 | 4.33E2 ± 1.12E2 | 474.61 ± 78.43 | 1.29 ± 5.42 | 151.75 ± 8.34 | 4.30E2 ± 1.70E2 |
| SDSSJ104058.79+581703.3 | 229.68 ± 96.48 | 1.45 ± 9.23E-1 | 40.00 ±3.30 | 8.74E2 ± 8.44E1 | 514.64 ± 44.30 | 2.91E-1 ± 9.53E-1 | 147.45 ± 3.01 | 1.75E2 ± 1.98E1 |
| UGC05984 | 235.37 ± 22.94 | 3.49E-1 ± 1.55 | 59.41 ±1.00 | 9.82E2 ± 5.76E1 | 535.89 ± 79.68 | 6.98E-2 ± 3.11E-1 | 138.12 ± 2.54 | 1.96E2 ± 1.15E1 |
| UGC06527 | 218.61 ±1.50 | 3.05 ± 4.19E-2 | 60.02 ±0.23 | 1.51E3 ± 5.12 | 567.10 ±2.08 | 6.10E-1 ± 8.38E-3 | 159.92 ± 0.14 | 3.01E2 ± 1.02 |

Table 3. Model Parameters for 24 AGNs Which Show a Thermal Continuum Superimposed with PAH Features

| Source | $T_w^S$ (K) | $M_w^S$ ($M_\odot$) | $T_c^S$ (K) | $M_c^S$ ($M_\odot$) | $T_w^G$ (K) | $M_w^G$ ($M_\odot$) | $T_c^G$ (K) | $M_c^G$ ($M_\odot$) |
|---|---|---|---|---|---|---|---|---|
| (1) | (2) | (3) | (4) | (5) | (6) | (7) | (8) | (9) |
| PG0007+106 | 264.22 ± 3.52 | 1.34E1 ± 7.21E-1 | 59.13 ± 0.23 | 1.71E4 ± 5.29E1 | 624.16±3.28 | 4.60 ± 3.29E-1 | 146.49 ± 0.12 | 3.42E3 ± 1.06E1 |
| PG0157+001 | 342.59 ± 0.69 | 1.07E2 ± 7.54E-1 | 63.67 ± 0.14 | 9.94E5 ± 4.06E3 | 558.03±0.90 | 2.14E1 ± 1.51E-1 | 116.62 ± 0.07 | 1.99E5 ± 8.12E2 |
| PG0923+129 | 184.57 ± 0.82 | 4.91 ± 3.59E-2 | 57.39 ± 0.14 | 2.33E3 ± 4.81 | 549.11±1.06 | 9.81E-1 ± 7.19E-3 | 156.94 ± 0.09 | 4.66E2 ± 9.62E-1 |
| PG0934+013 | 207.87 ± 2.91 | 6.91 ± 1.95E-1 | 65.89 ± 0.09 | 3.55E3 ± 1.54E1 | 505.09±3.45 | 1.38 ± 3.89E-2 | 142.56 ± 0.15 | 7.10E2 ± 3.08 |
| PG1022+519 | 199.99 ± 2.04 | 2.46 ± 2.52E-1 | 64.38 ± 0.14 | 1.75E3 ± 1.52E1 | 509.99±1.94 | 1.05 ± 1.46E-1 | 138.17 ± 0.34 | 3.49E2 ± 3.03 |
| PG1115+407 | 150.00 ± 7.09 | 1.36E1 ± 8.85 | 73.56 ± 6.62 | 1.22E4 ± 2.04E3 | 617.87 ± 17.67 | 6.25 ± 4.18 | 158.95 ± 3.95 | 2.44E3 ± 4.08E2 |
| PG1119+120 | 239.27 ± 3.08 | 7.45 ± 5.97E-1 | 65.26 ± 0.18 | 7.74E3 ± 3.41E1 | 478.03±1.95 | 4.98 ± 5.27E-1 | 147.76 ± 0.18 | 1.55E3 ± 6.82 |
| PG1126-041 | 150.00 ± 0.00 | 2.88 ± 2.01E-1 | 67.04 ± 0.06 | 1.16E4 ± 2.23E1 | 770.16±3.85 | 1.94 ± 1.99E-1 | 155.06 ± 0.07 | 2.32E3 ± 4.45 |
| PG1149-110 | 210.57 ± 2.44 | 3.45 ± 6.47E-2 | 49.91 ± 0.39 | 3.89E3 ± 1.08E1 | 605.99±3.26 | 6.91E-1 ± 1.29E-2 | 151.38 ± 0.10 | 7.78E2 ± 2.15 |
| PG1244+026 | 267.05 ± 2.18 | 2.61 ± 9.20E-2 | 68.36 ± 0.15 | 1.79E3 ± 1.12E2 | 482.88±2.54 | 1.75 ± 8.76E-2 | 143.43 ± 0.26 | 7.83E2 ± 7.03E1 |
| PG1415+451 | 215.73 ± 2.14 | 2.16E1 ± 1.49 | 66.63 ± 0.37 | 9.46E3 ± 4.82E1 | 573.56±1.88 | 5.25 ± 5.13E-1 | 154.77 ± 0.19 | 1.89E3 ± 9.64 |
| PG1425+267 | 288.67 ± 9.53 | 1.31E2 ± 1.62E1 | 73.65 ± 1.09 | 8.95E4 ± 2.30E3 | 655.00±3.73 | 2.74E1 ± 5.37 | 156.77 ± 0.56 | 1.79E4 ± 4.90E2 |
| PG1519+226 | 247.49 ± 2.56 | 1.57E1 ± 7.42E-1 | 70.14 ± 0.47 | 1.11E4 ± 8.56E1 | 637.60±1.84 | 6.68 ± 4.77E-1 | 163.31 ± 0.28 | 2.21E3 ± 1.71E1 |
| PG1612+261 | 223.24 ± 1.19 | 3.15E1 ± 2.78E-1 | 40.00 ± 0.00 | 2.51E4 ± 7.41E1 | 610.56±1.51 | 6.30 ± 5.56E-2 | 150.61 ± 0.10 | 5.01E3 ± 1.50E1 |
| PG1613+658 | 150.00 ± 0.00 | 1.26E2 ± 8.70 | 68.19 ± 0.07 | 5.41E4 ± 1.36E2 | 571.74±1.05 | 2.94E1 ± 3.54 | 155.68 ± 0.08 | 1.08E4 ± 2.72E1 |
| PG2130+099 | 150.00 ± 0.00 | 1.06E1 ± 1.70E-1 | 66.86 ± 0.19 | 1.21E4 ± 3.47E1 | 609.57±1.15 | 5.88 ± 1.34E-1 | 159.42 ± 0.10 | 2.42E3 ± 6.95 |
| 2MASSiJ165939.7+183436 | 150.00 ± 2.60 | 5.45E1 ± 9.40E1 | 76.87 ± 8.09 | 5.25E4 ± 1.25E4 | 492.49 ± 21.82 | 3.57E1 ± 6.19E1 | 153.14 ± 5.03 | 1.05E4 ± 2.49E3 |
| 2MASXJ08381094+2453427 | 250.83 ± 3.62 | 1.04 ± 4.96E-2 | 62.80 ± 0.20 | 1.15E3 ± 7.04 | 595.64±7.61 | 2.07E-1 ± 9.93E-3 | 152.54 ± 0.25 | 2.30E2 ± 1.41 |
| 2MASXJ22533142+0048252 | 191.06 ± 6.43 | 8.76 ± 8.54E-1 | 89.88 ± 31.24 | 2.15E2 ± 2.44E1 | 457.59±9.73 | 1.75 ± 2.23E-1 | 154.25 ± 2.55 | 4.30E2 ± 4.89E1 |
| 2MASXJ15085397-0011486 | 244.12 ± 4.23 | 2.24 ± 7.37E-2 | 45.04 ± 0.75 | 3.80E3 ± 1.75E1 | 707.77±7.34 | 4.47E-1 ± 1.47E-2 | 154.11 ± 0.17 | 7.59E2 ± 3.50 |
| 2MASXJ14175951+2508124 | 216.15 ± 1.76 | 4.55 ± 1.21E-1 | 63.11 ± 0.06 | 2.34E3 ± 6.80 | 477.36±3.04 | 9.10E-1 ± 2.41E-2 | 140.46 ± 0.12 | 4.67E2 ± 1.36 |
| 2MASXJ12042964+2018581 | 281.38 ± 15.51 | 1.12 ± 1.34E-1 | 65.10 ± 0.14 | 1.55E3 ± 1.16E1 | 538.85±7.81 | 5.90E-1 ± 1.15E-1 | 145.77 ± 0.35 | 3.10E2 ± 2.32 |
| 2MASXJ10032788+5541535 | 218.90 ± 15.85 | 4.83 ± 1.15 | 58.48 ± 3.03 | 2.01E3 ± 8.48E1 | 502.65 ± 26.73 | 9.65E-1 ± 2.85E-1 | 158.26 ± 1.69 | 4.02E2 ± 1.76E1 |
| 2MASSJ16593976+1834367 | 237.46 ± 29.89 | 6.83E1 ± 1.40E2 | 73.17 ± 7.24 | 7.24E4 ± 1.06E4 | 507.00 ± 24.51 | 4.55E1 ± 9.60E1 | 150.69 ± 3.81 | 1.45E4 ± 2.12E3 |

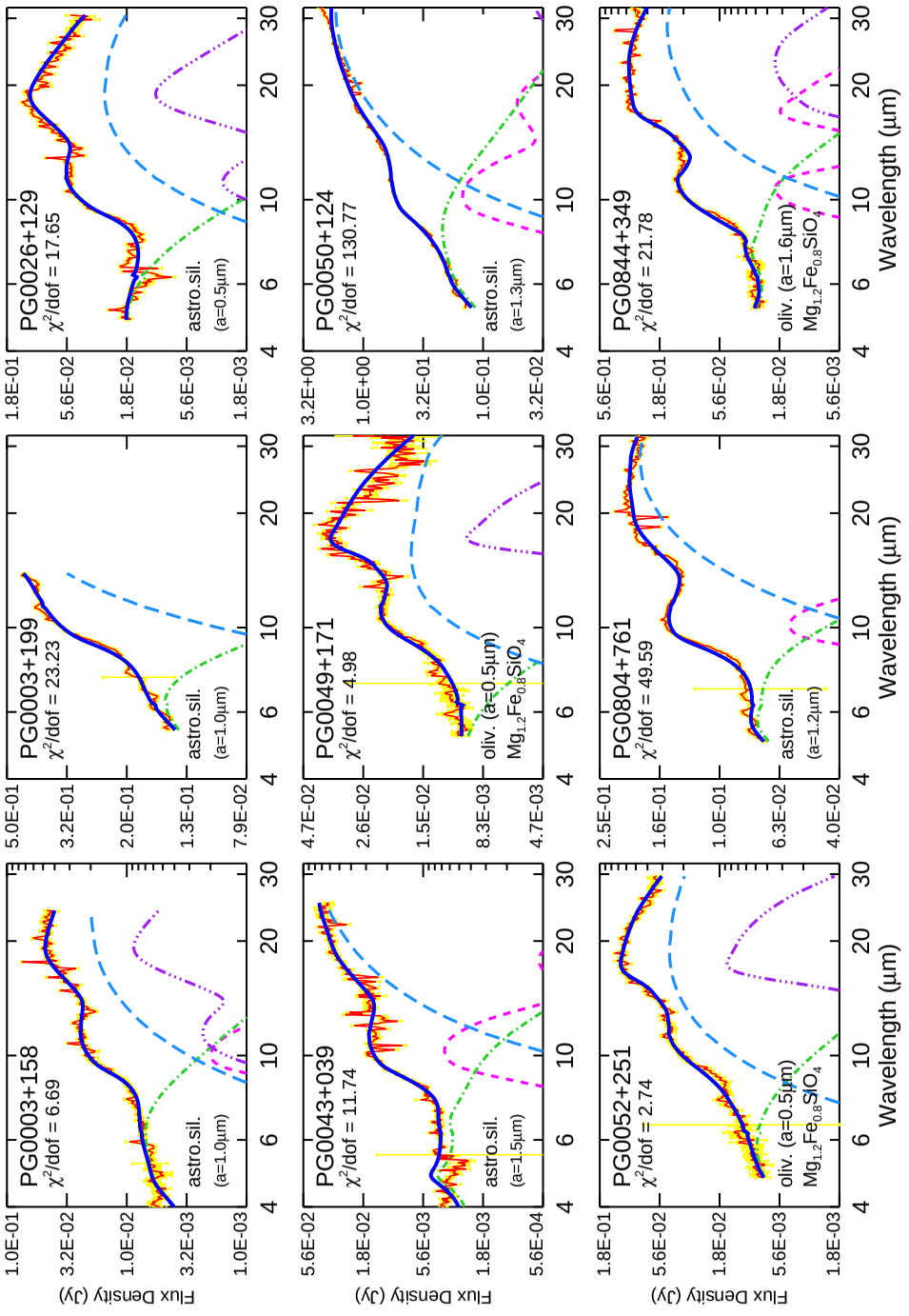


Fig. 1.— Comparison of the *Spitzer*/IRS spectra (red solid lines) of the PG quasars PG0003+158, PG0003+199, PG0026+129, PG0043+039, PG0049+171, PG0050+124, PG0052+251, PG0804+761, PG0844+349 which show silicate emission around 9.7 and 18 $\mu$m with the model spectra (blue solid lines) which are the sum of warm silicate (magenta short dashed lines), cold silicate (purple dash-dot-dotted lines), warm graphite (green dash-dotted lines), and cold graphite (light blue long dashed lines). Also shown are the observed 1$\sigma$ errors (yellow vertical lines).

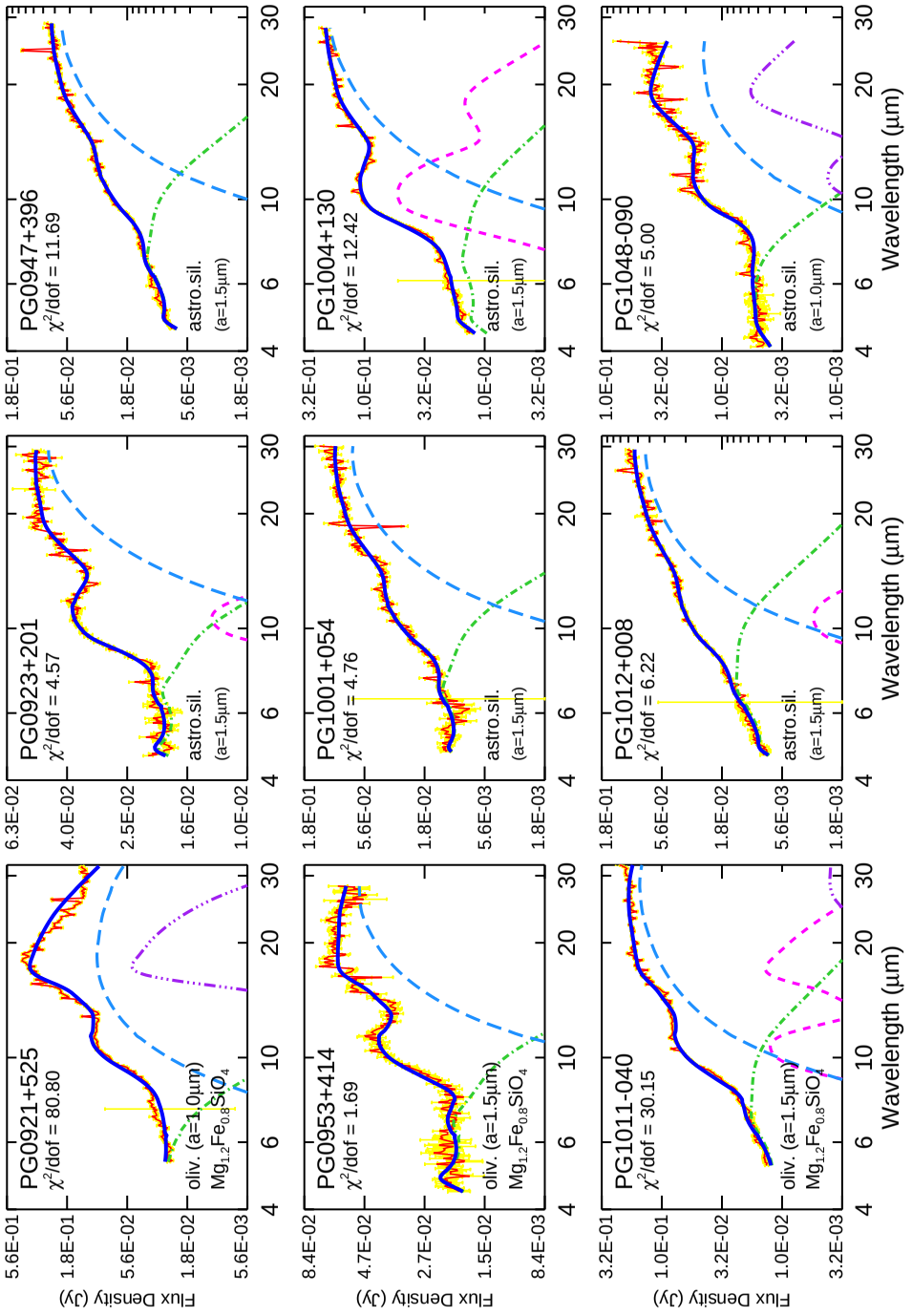


Fig. 1.— Continued, but for the PG quasars PG0921+525, PG0923+201, PG0947+396, PG0953+414, PG1001+054, PG1004+130, PG1011-040, PG1012+008, and PG1048-090.

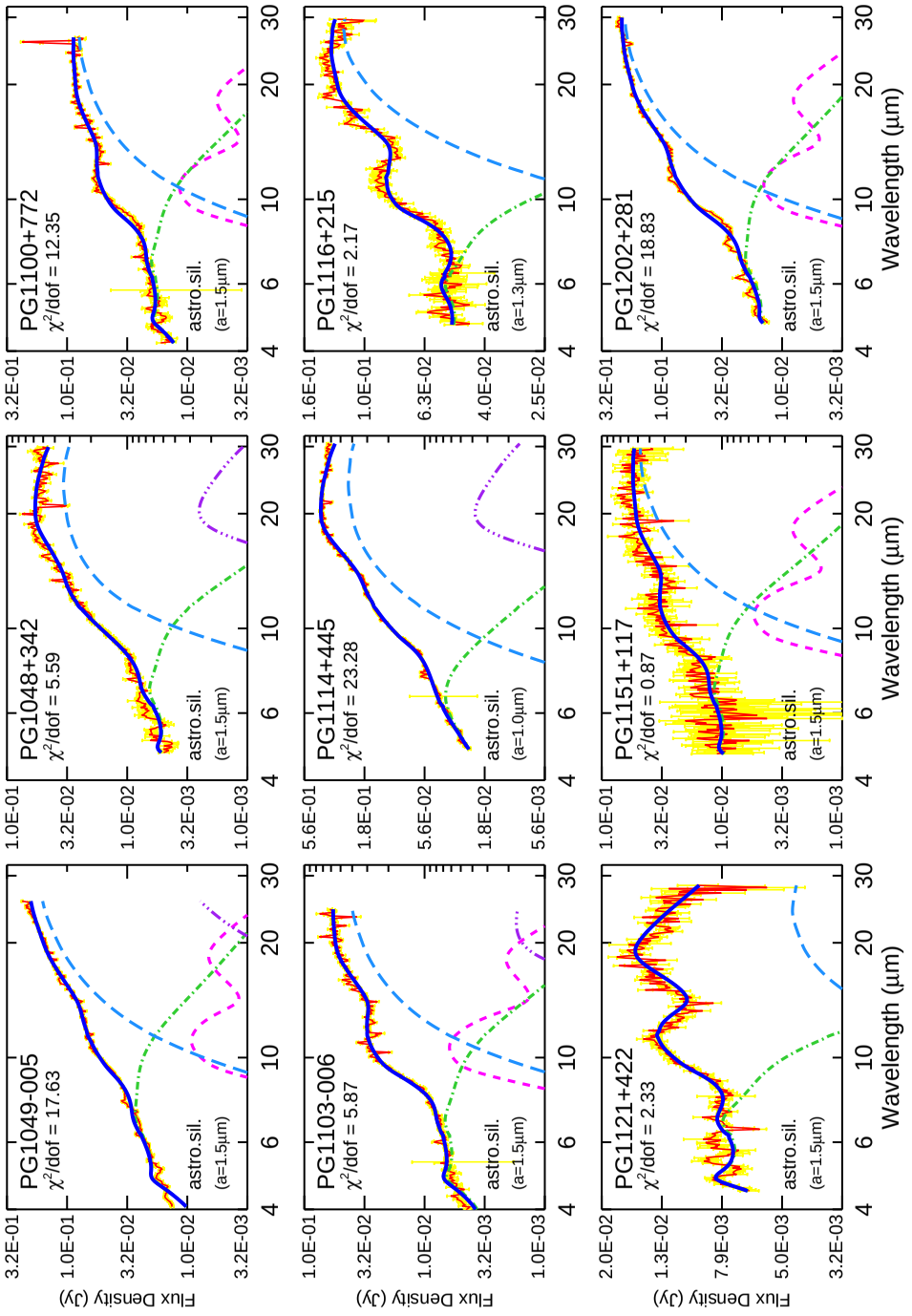


Fig. 1.— Continued, but for the PG quasars PG1049-005, PG1048+342, PG1100+772, PG1103-006, PG1114+445, PG1116+215, PG1121+422, PG1151+117, and PG1202+281.

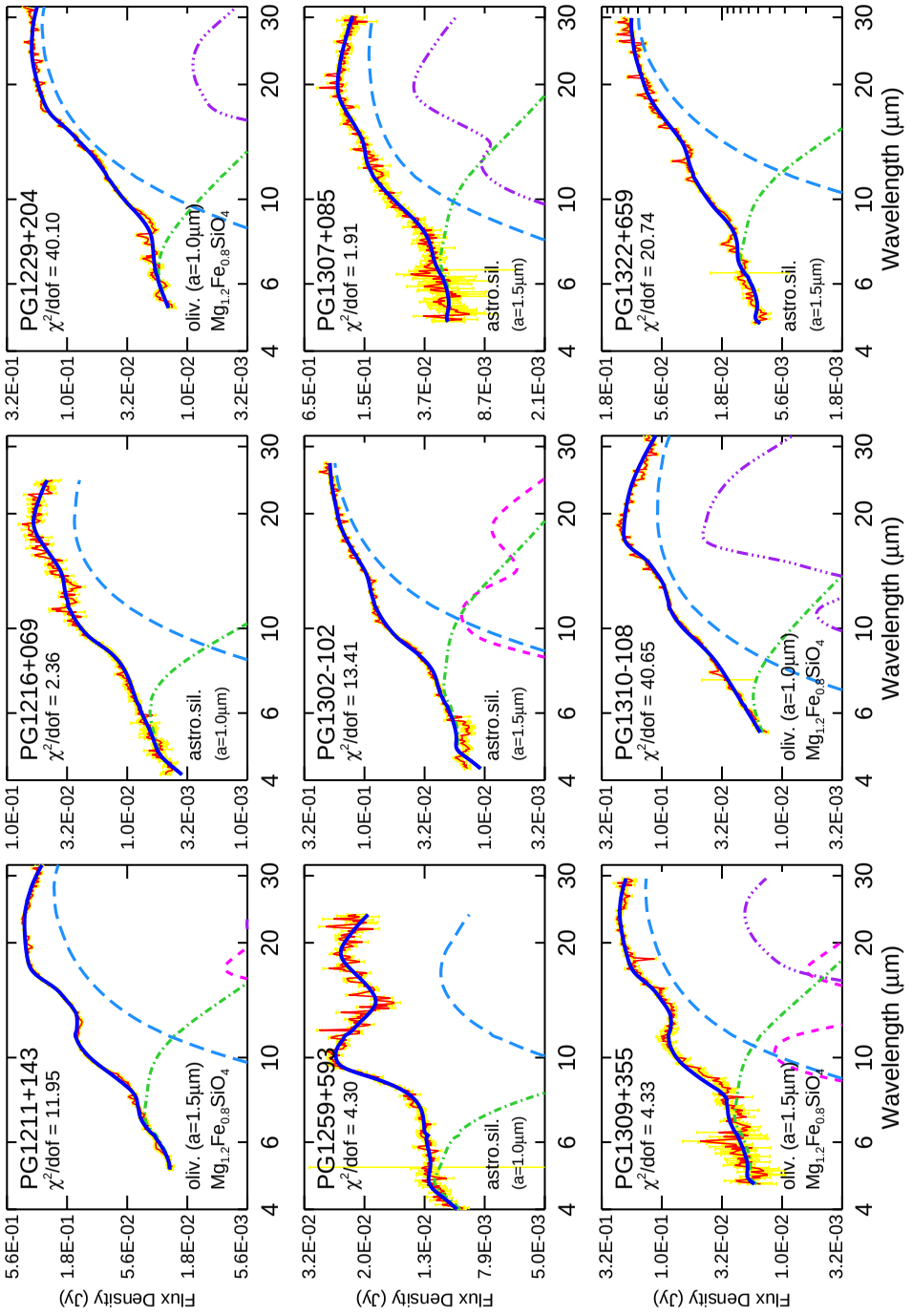


Fig. 1.— Continued, but for the PG quasars PG1211+143, PG1216+069, PG1229+204, PG1259+593, PG1302-102, PG1307+085, PG1309+355, PG1310-108, and PG1322+659.

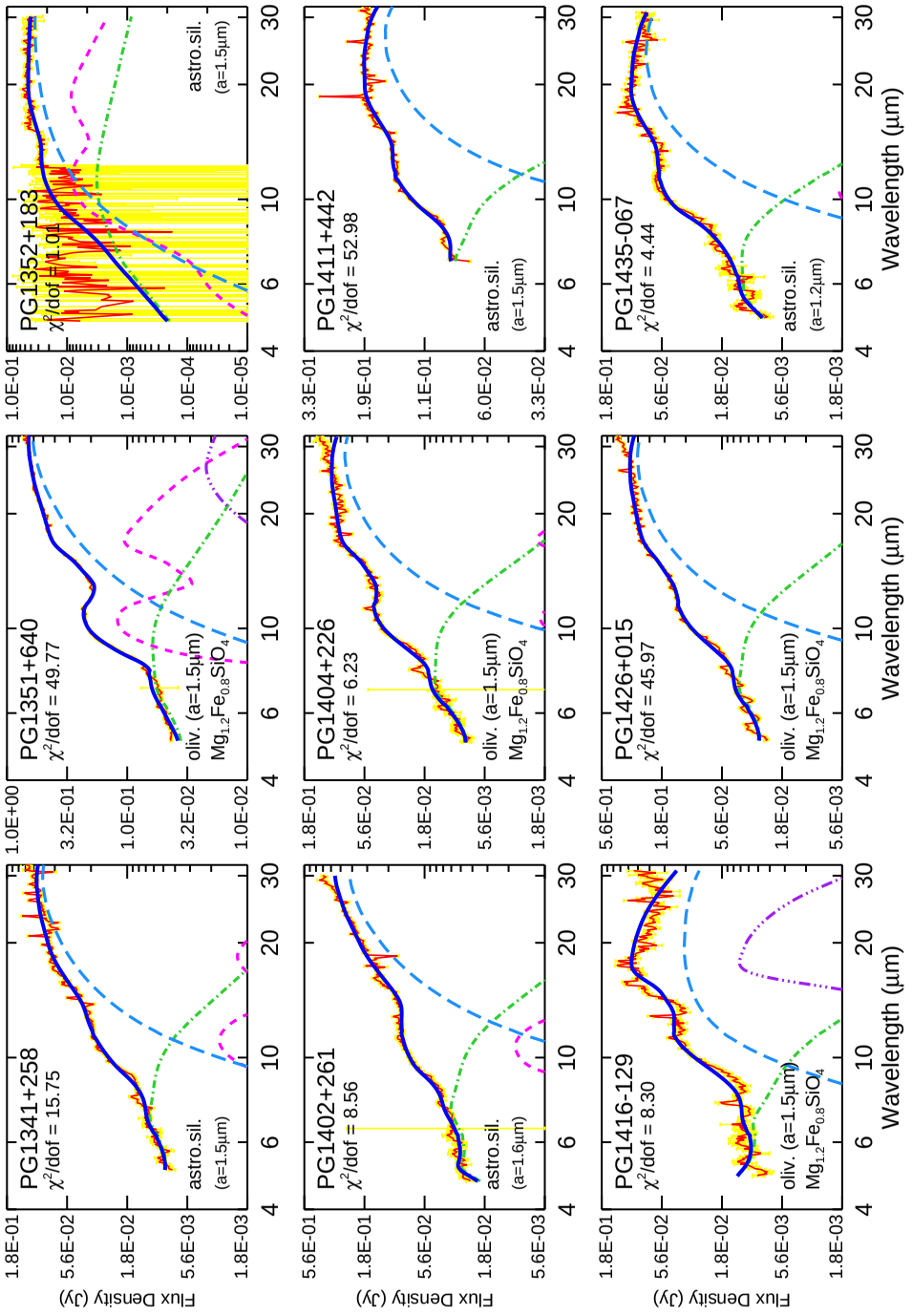


Fig. 1.— Continued, but for the PG quasars PG1341+258, PG1351+640, PG1352+183, PG1402+261, PG1404+226, PG1411+442, PG1416-129, PG1426+015, and PG1435-067.

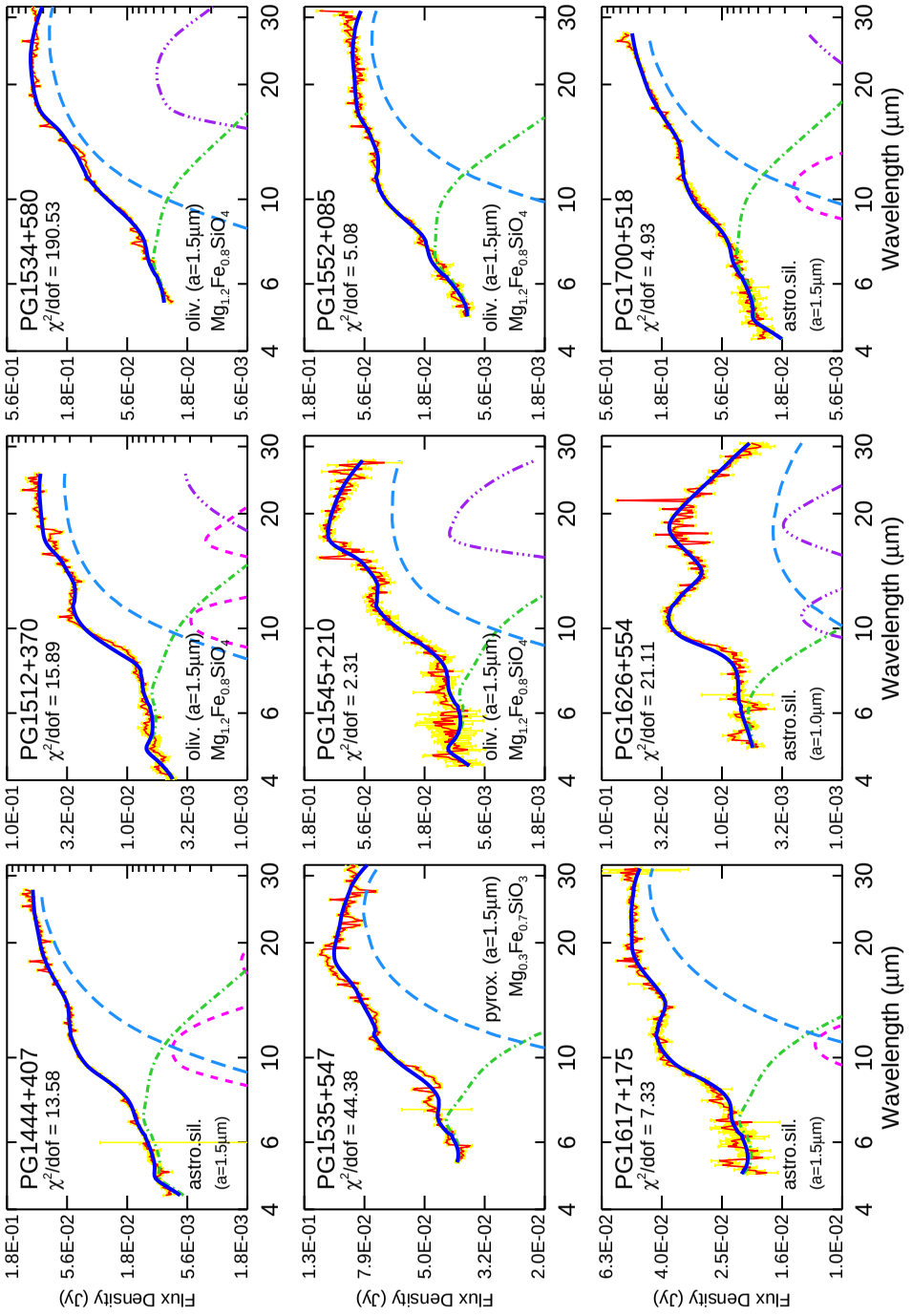


Fig. 1.— Continued, but for the PG quasars PG1444+407, PG1512+370, PG1534+580, PG1535+547, PG1545+210, PG1552+085, PG1617+175, PG1626+554, and PG1700+518.

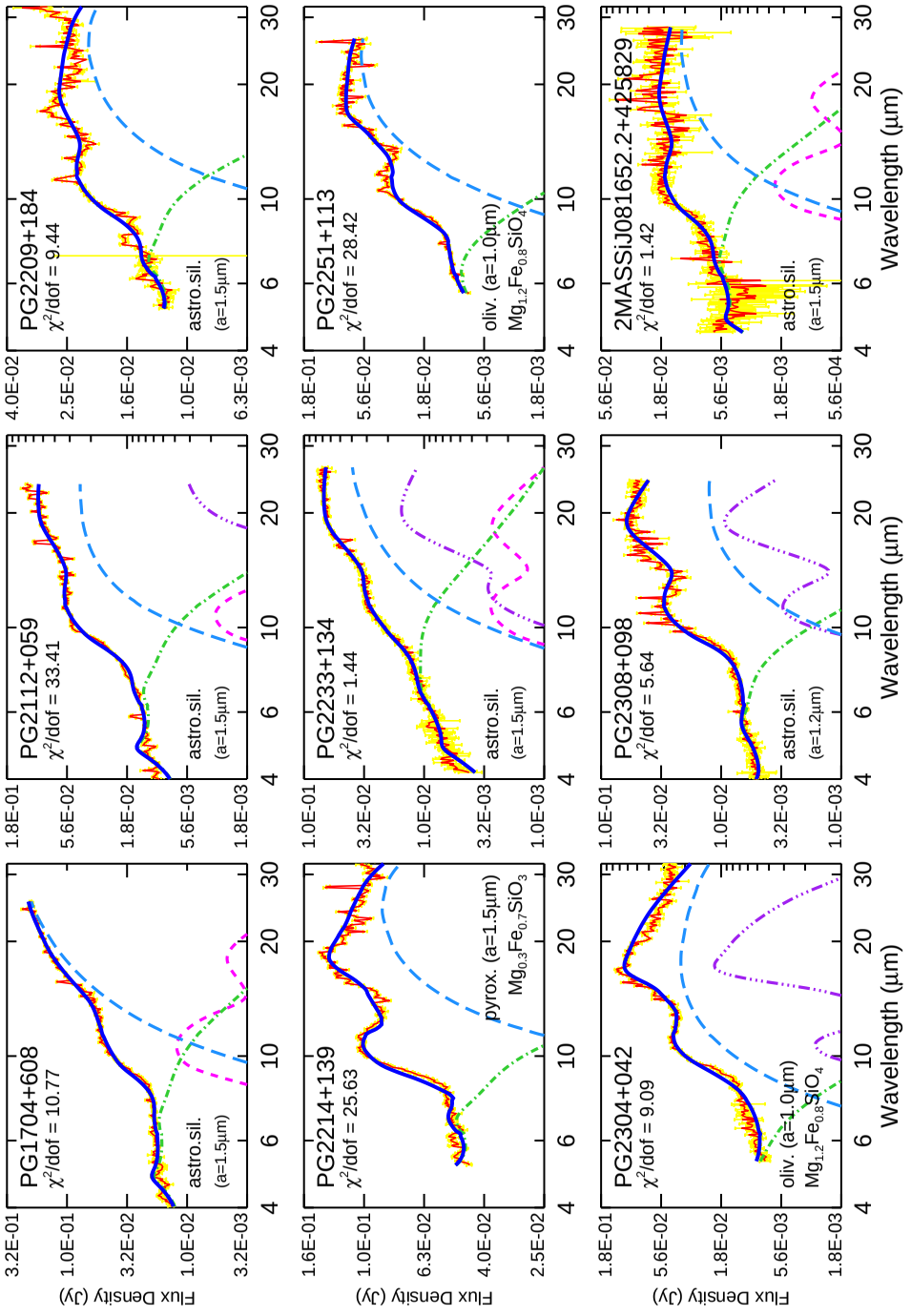


Fig. 1.— Continued, but for the PG quasars PG1704+608, PG2112+059, PG2209+184, PG2214+139, PG2233+134, PG2251+113, PG2304+042, PG2308+098 and the *2MASS* quasar 2MASSiJ081652.2+425829.

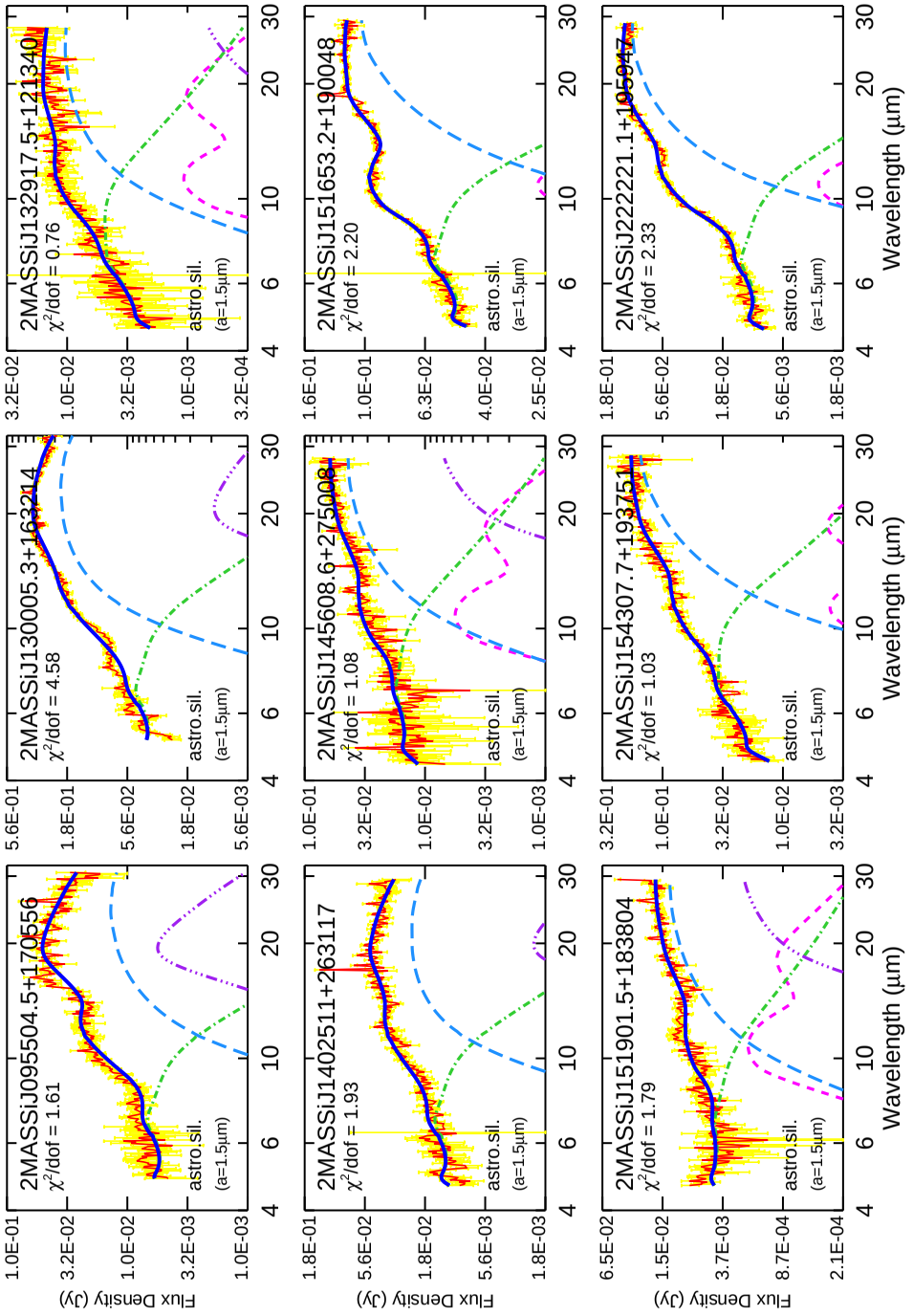


Fig. 1.— Continued, but for the *2MASS* quasars 2MASSiJ095504.5+170556, 2MASSiJ130005.3+163214, 2MASSiJ132917.5+121340, 2MASSiJ1402511+263117, 2MASSiJ145608.6+275008, 2MASSiJ151653.2+190048, 2MASSiJ151901.5+183804, 2MASSiJ154307.7+193751, and 2MASSiJ222221.1+195947.

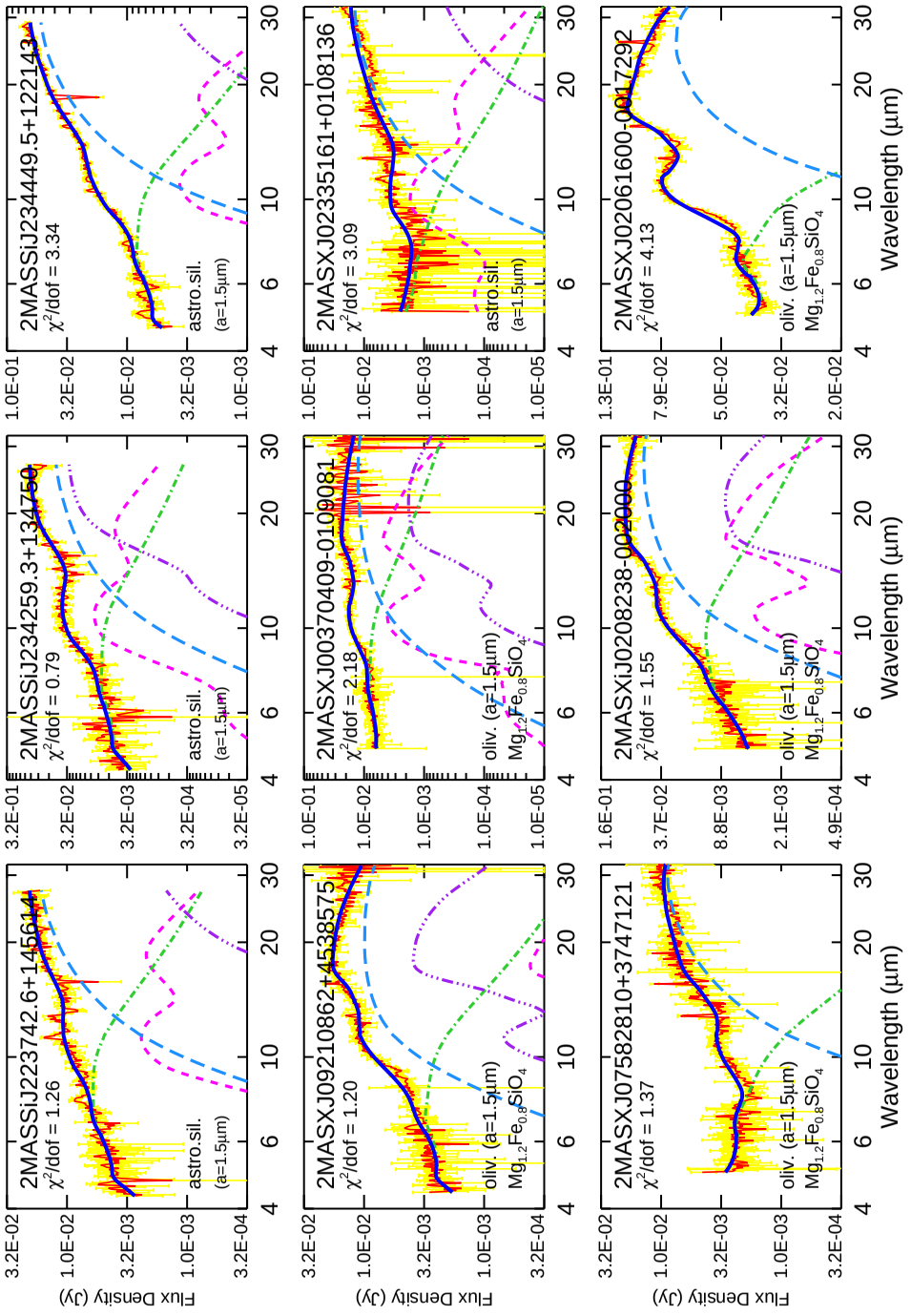


Fig. 1.— Continued, but for the *2MASS* quasars 2MASSiJ223742.6+145614, 2MASSiJ234259.3+134750, 2MASSiJ234449.5+122143 and the S$^3$AGA AGNs 2MASXJ09210862+4538575, 2MASXJ00370409-0109081, 2MASXJ02335161+0108136, 2MASXJ07582810+3747121, 2MASXiJ0208238-002000, and 2MASXJ02061600-0017292.

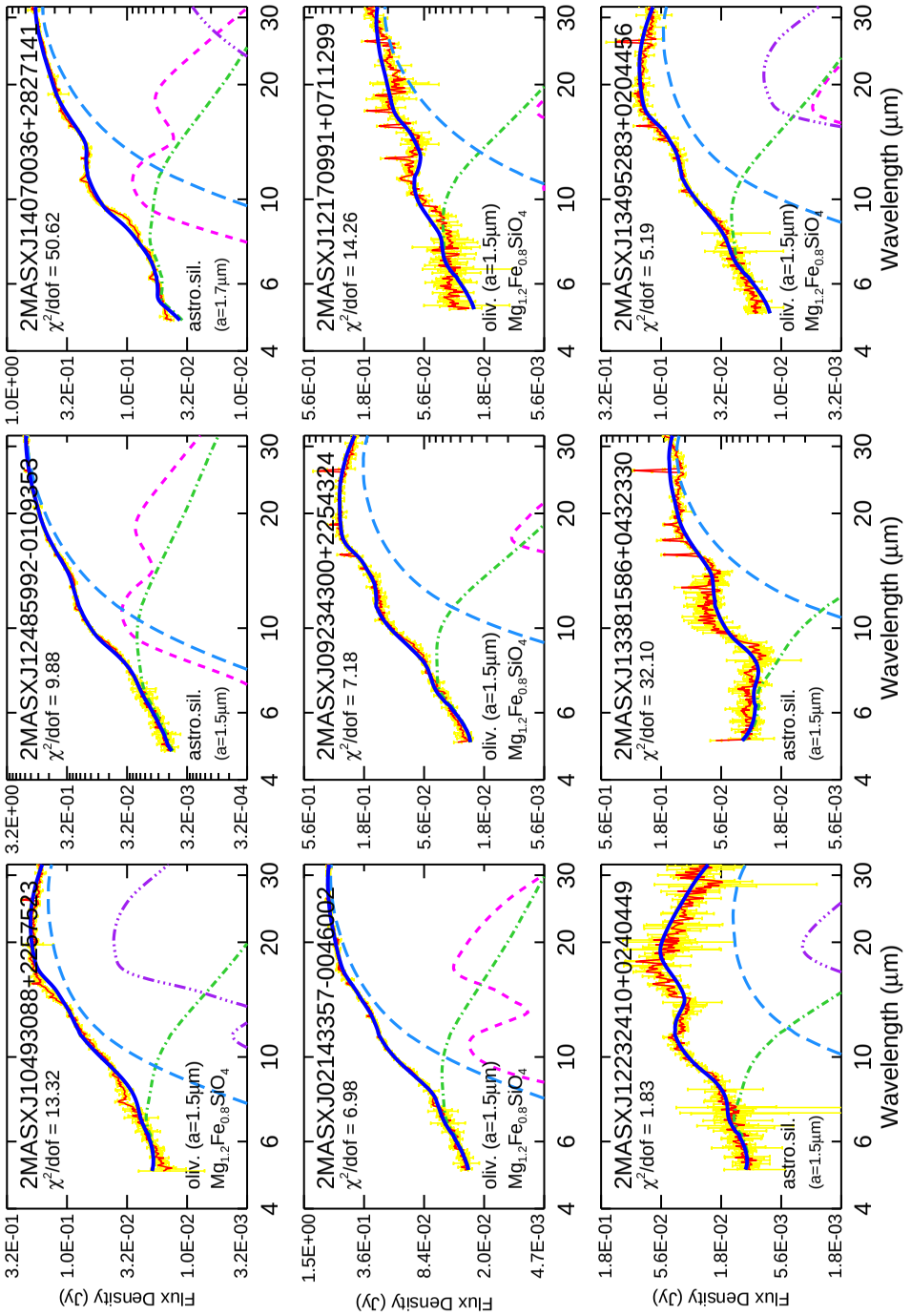


Fig. 1.— Continued, but for the S$^3$AGA AGNs 2MASXJ10493088+2257523, 2MASXJ12485992-0109353, 2MASXJ14070036+2827141, 2MASXJ02143357-0046002, 2MASXJ09234300+2254324, 2MASXJ12170991+0711299, 2MASXJ12232410+0240449, 2MASXJ13381586+0432330, and 2MASXJ13495283+0204456.

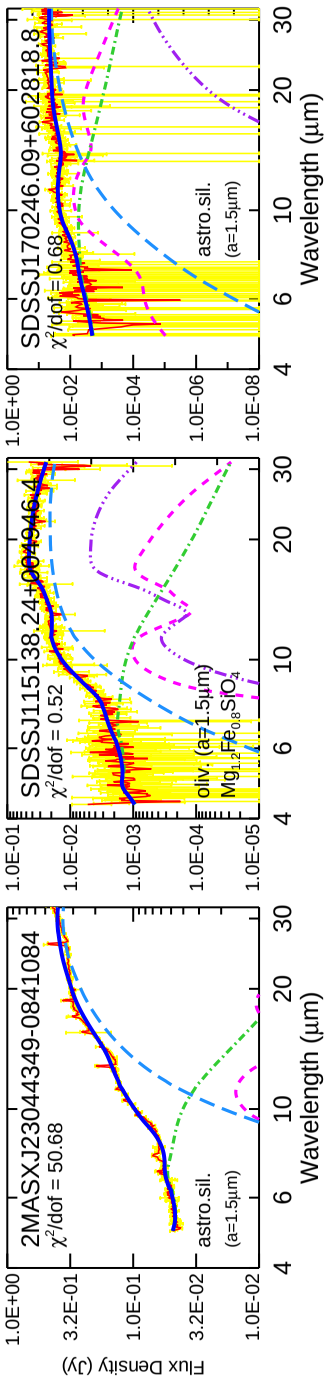


Fig. 1.— Continued, but for the S$^3$AGA AGNs 2MASXJ23044349-0841084, SDSSJ115138.24+004946.4, and SDSSJ170246.09+602818.8.

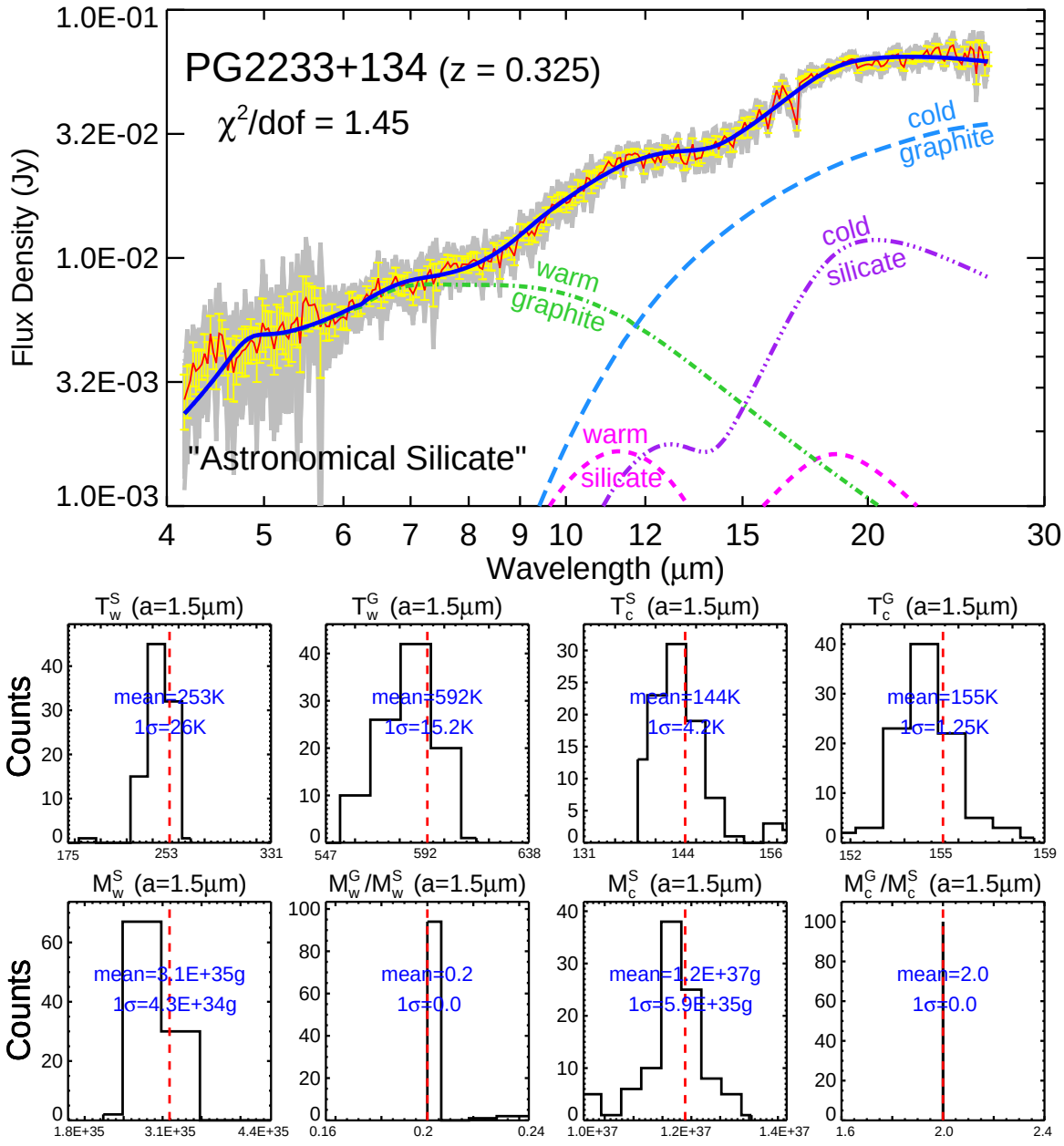


Fig. 2.— Estimating the uncertainties of the model parameters from Monte-Carlo simulation, with PG 2233+134 as an example. The top panel compares the *Spitzer*/IRS spectrum (red solid line) of PG 2233+134, as well as the observed $1\sigma$ error (yellow vertical lines) and the random spectrum generated from Monte-Carlo simulation (gray lines), with the model spectrum (blue solid line) which is the sum of warm silicate (magenta short dashed lines), cold silicate (purple dash-dot-dotted lines), warm graphite (green dash-dotted lines), and cold graphite (light blue long dashed lines). The middle panels show the distributions of the dust temperatures derived from 100 Monte-Carlo simulations for warm silicate, warm graphite, cold silicate and cold graphite. The bottom panels show the mass and mass-ratio distributions derived from 100 Monte-Carlo simulations for warm silicate or graphite, and cold silicate or graphite.

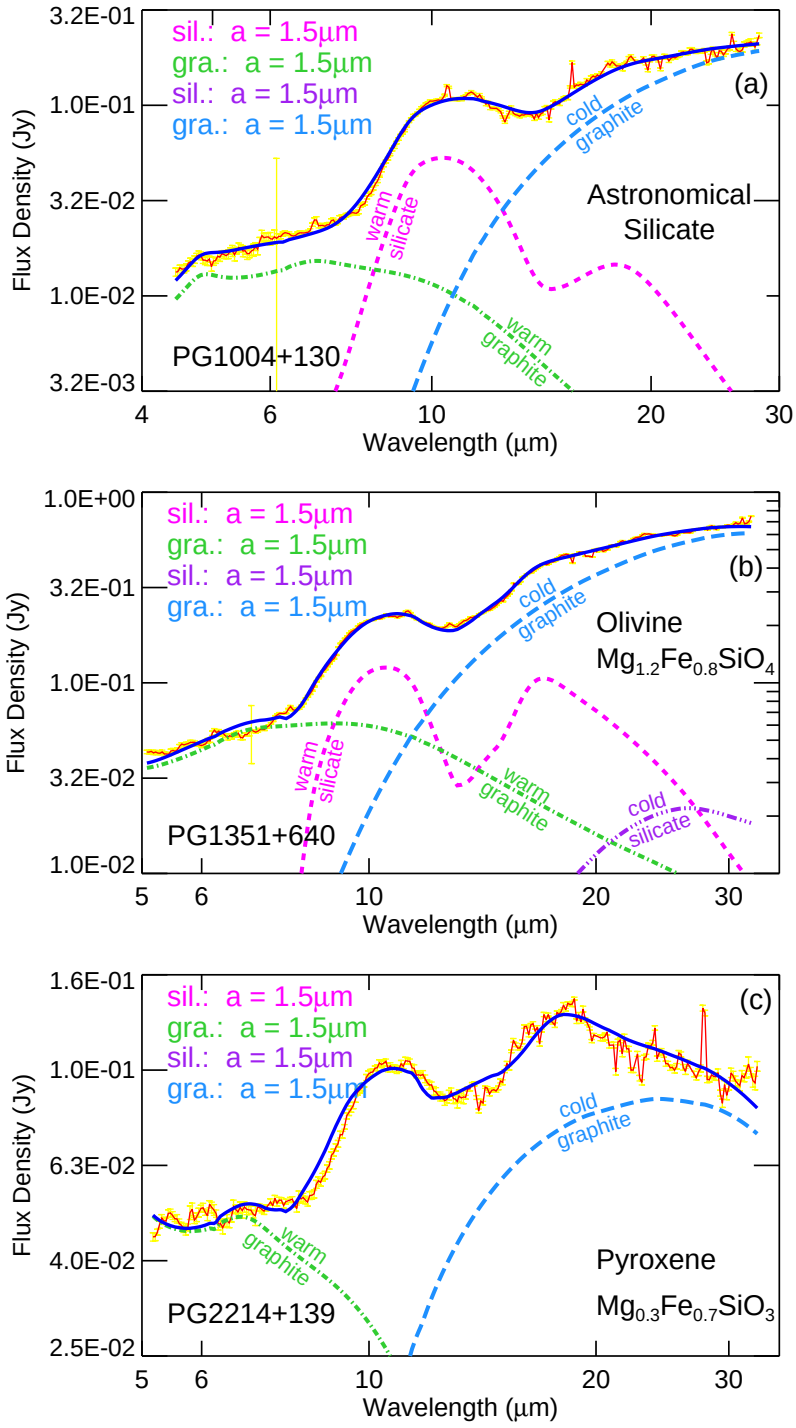


Fig. 3.— Illustrating the model fits to the *Spitzer*/IRS spectra of three PG quasars which require different silicate compositions: "astronomical silicate" for PG 1004+130 (a), olivine $Mg_{1.2}Fe_{0.8}SiO_4$ for PG 1351+640 (b), and pyroxene $Mg_{0.3}Fe_{0.7}SiO_3$ for PG 2214+139 (c). In each sub-figure, we plot the *Spitzer*/IRS spectrum (solid red line), the observed $1\sigma$ error (yellow vertical lines), the model spectrum (blue solid line) and the four fitting components: warm silicate (magenta short dashed line), cold silicate (purple dash-dot-dotted line), warm graphite (green dash-dotted line), and cold graphite (light blue long dashed line).

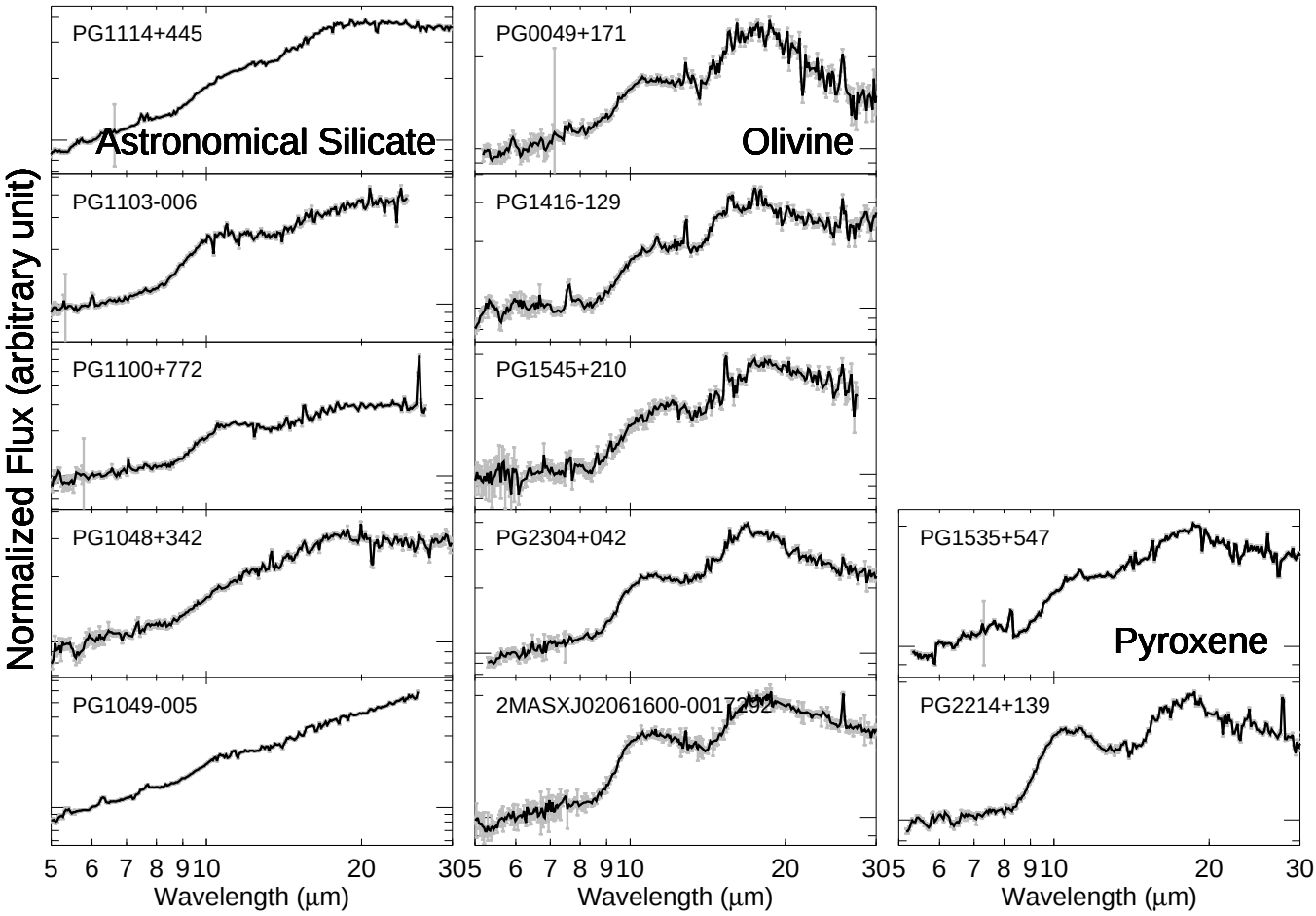


Fig. 4.— Illustrations of the *Spitzer*/IRS spectra of those AGNs for which the best fits favor "astronomical silicate" (left), amorphous olivine (middle), and amorphous pyroxene (right).

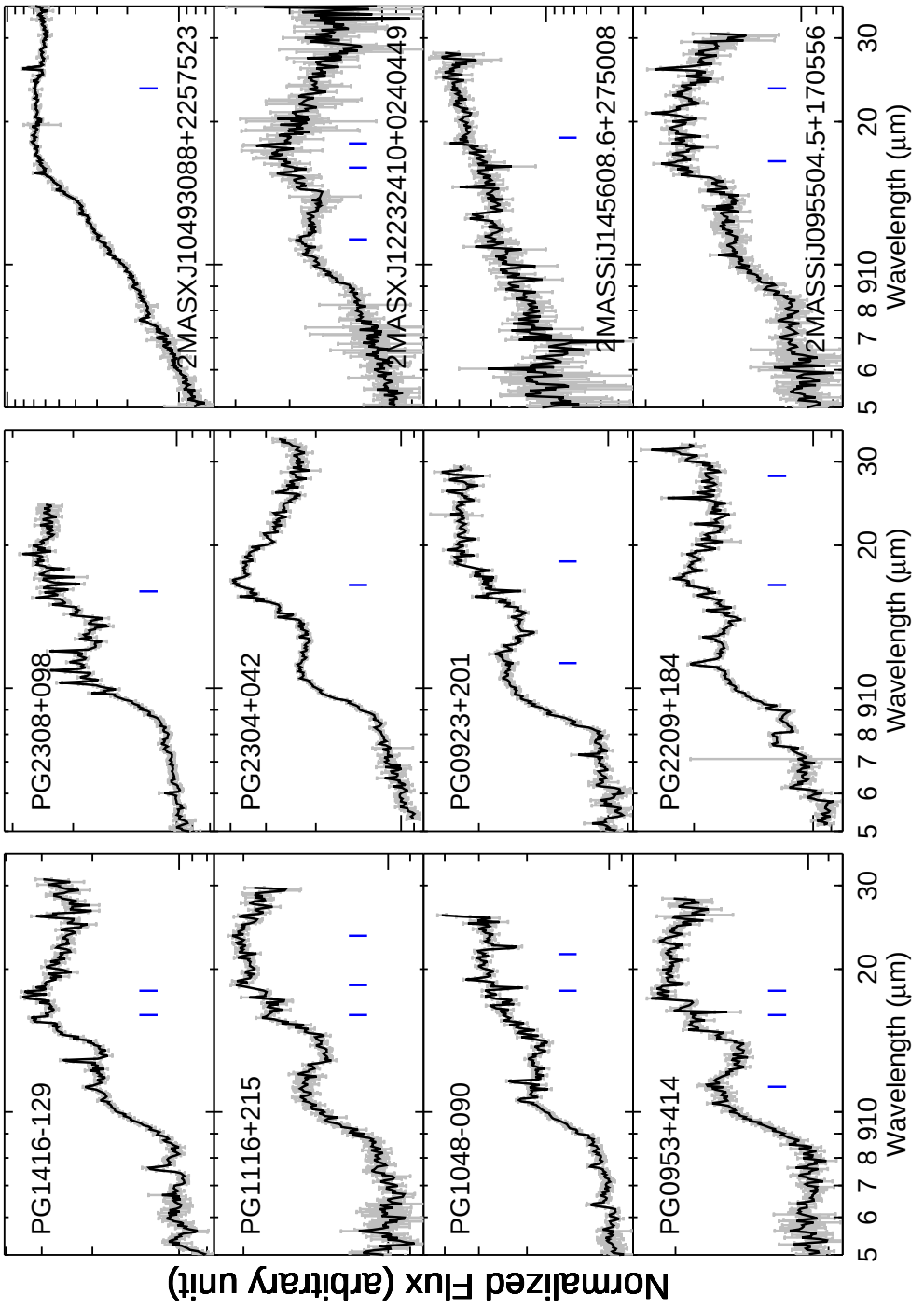


Fig. 5.— *Spitzer*/IRS spectra of those sources which exhibit crystalline silicate emission features.

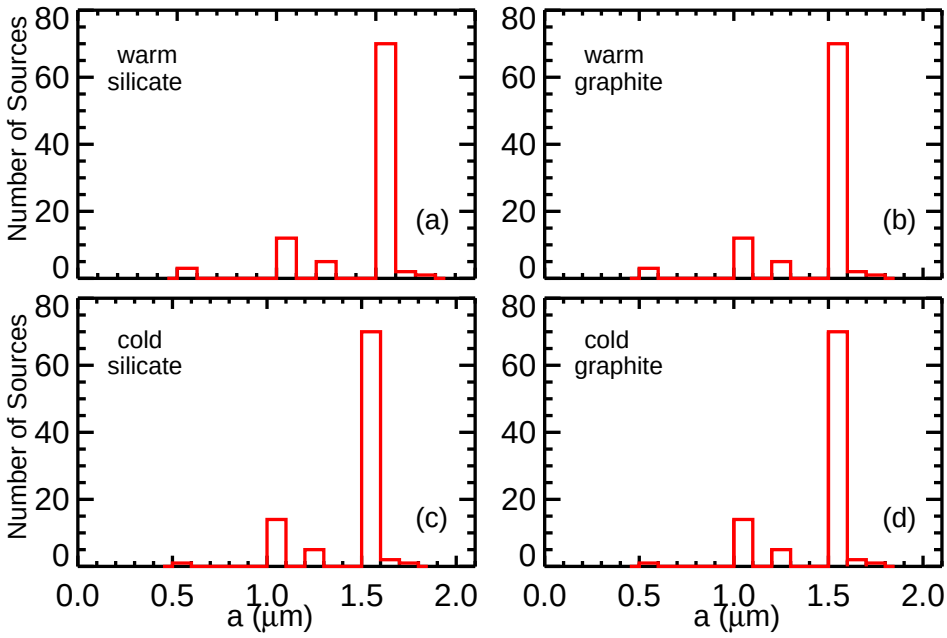


Fig. 6.— Histogram of the sizes of (a) the warm silicate component, (b) the warm graphite component, (c) the cold silicate component, and (d) the cold graphite component derived for 93 sources which exhibit the 9.7 and 18 $\mu$m silicate emission features.

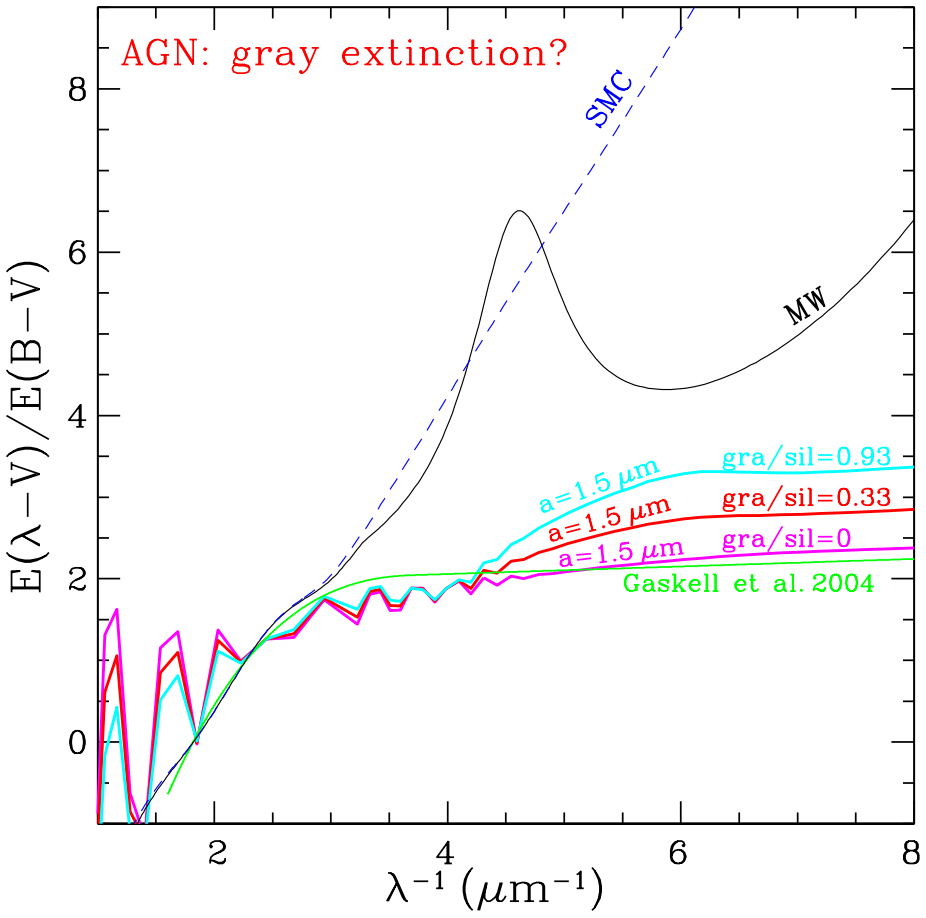


Fig. 7.— Comparison of the extinction curves of the Milky Way (black solid line) and the SMC (blue dashed line) with that of Gaskell et al. (2004) derived from composite quasar spectra (green solid line) and that calculated from spherical silicate and graphite grains of radii $a = 1.5\,\mu$m with a mass mixing ratio of $M_{\rm carb}/M_{\rm sil} = 0$ (magenta solid line), $M_{\rm carb}/M_{\rm sil} = 0.33$ (red solid line), and $M_{\rm carb}/M_{\rm sil} = 0.93$ (cyan solid line). The sawtooth-like structures seen in the calculated extinction curves at $\lambda^{-1} < 2.5\,\mu{\rm m}^{-1}$ will be smoothed out if a distribution of grain sizes is considered. Note that at $\lambda^{-1} > 2.5\,\mu{\rm m}^{-1}$ the extinction curve of spherical silicate dust of radii $a = 1.5\,\mu$m (magenta solid line) closely agrees with the AGN extinction curve of Gaskell et al. (2004).

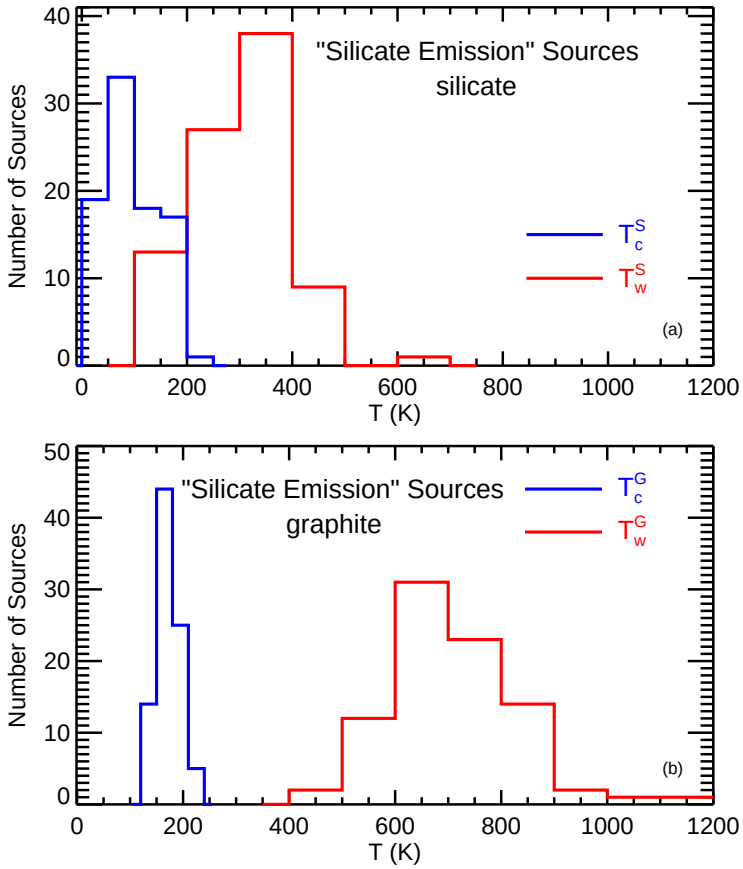


Fig. 8.— Histograms of dust temperatures of the warm silicate component (red line in upper panel), the cold silicate component (blue line in upper panel), the warm graphite component (red line in bottom panel), and the cold graphite component (blue line in bottom panel) derived for 93 sources which exhibit the 9.7 and 18 $\mu$m silicate emission features.

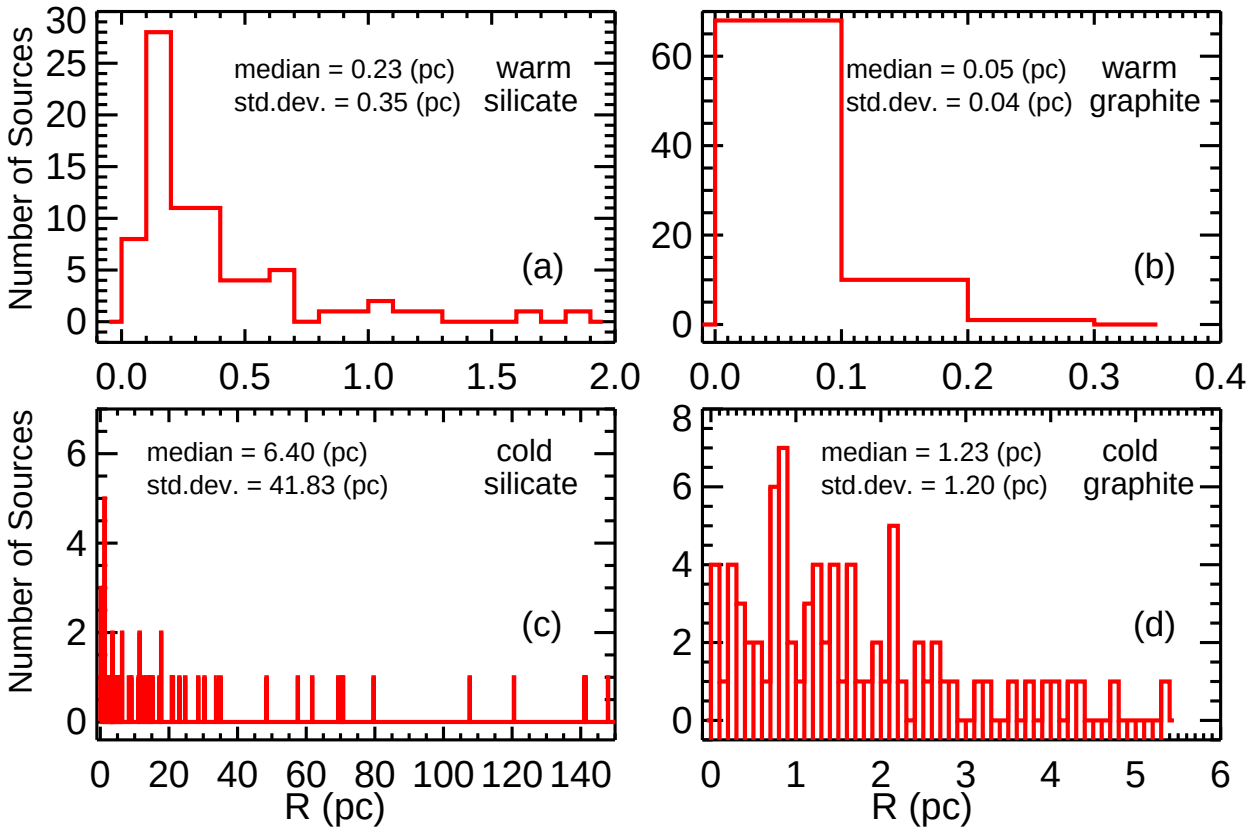


Fig. 9.— Histograms of the distances of the dust from the central engine for those 93 "silicate emission" sources: warm silicate (a), warm graphite (b), cold silicate (c), and cold graphite (d).

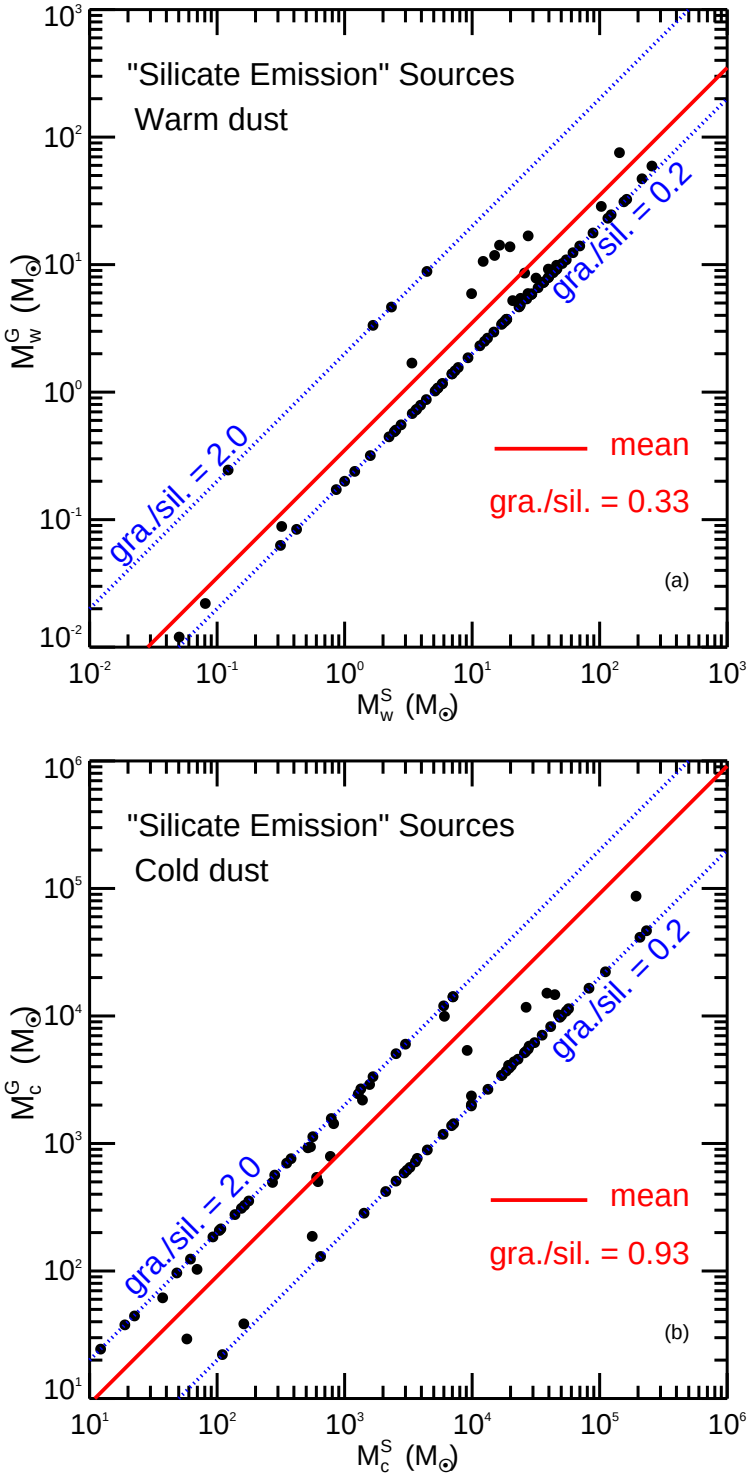


Fig. 10.— Dust mass ratios of warm graphite to warm silicate ($M_{\rm w}^{\rm G}/M_{\rm w}^{\rm S}$; upper panel) and of cold graphite to cold silicate ($M_{\rm c}^{\rm G}/M_{\rm c}^{\rm S}$; bottom panel) derived for those 93 "silicate emission" sources. The blue dotted lines show the upper ($M_{\rm c}^{\rm G}/M_{\rm c}^{\rm S} = 2.0$) and lower ($M_{\rm c}^{\rm G}/M_{\rm c}^{\rm S} = 0.2$) boundaries. The red solid lines show the mean mass ratios derived from our model.

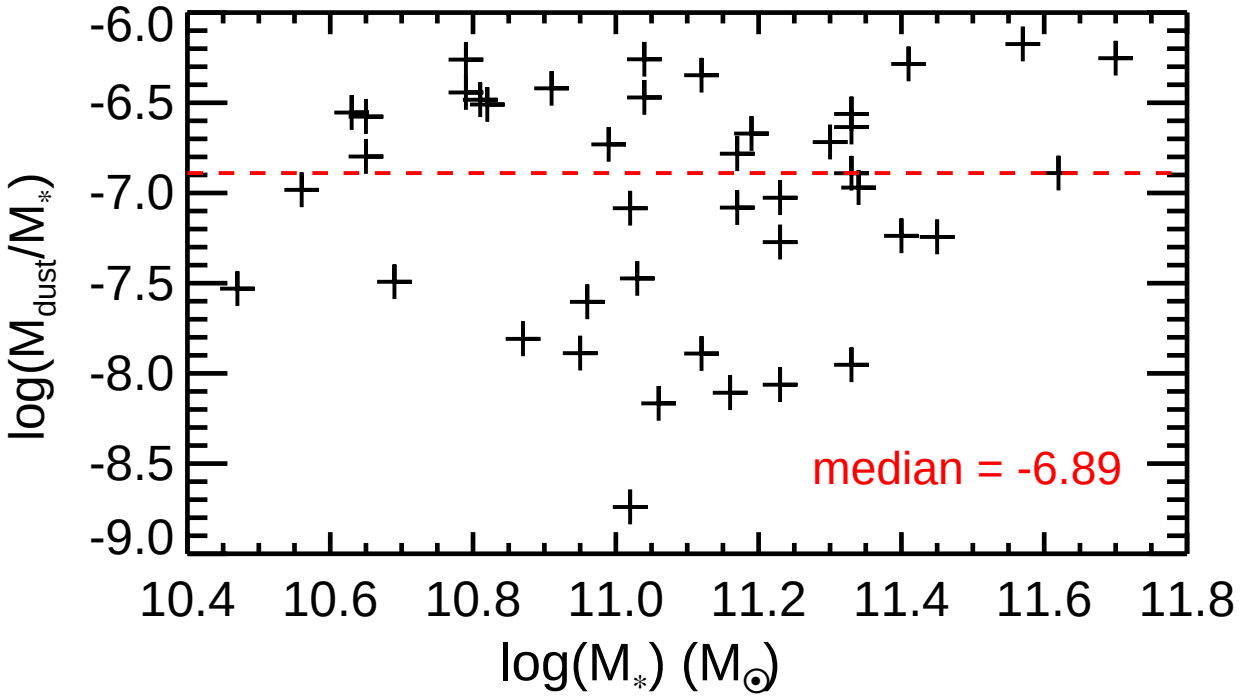


Fig. 11.— Comparison of the stellar mass ($M_\star$) of the host galaxies of 39 PG quasars and two *2MASS* quasars with the total dust mass ($M_{\rm dust}$) obtained by summing over all four dust components (i.e., $M_{\rm dust} = M_{\rm w}^{\rm S} + M_{\rm c}^{\rm S} + M_{\rm w}^{\rm G} + M_{\rm c}^{\rm G}$). The horizontal dashed line plots the median ratio of $\langle M_{\rm dust}/M_\star \rangle \approx 1.3 \times 10^{-7}$.

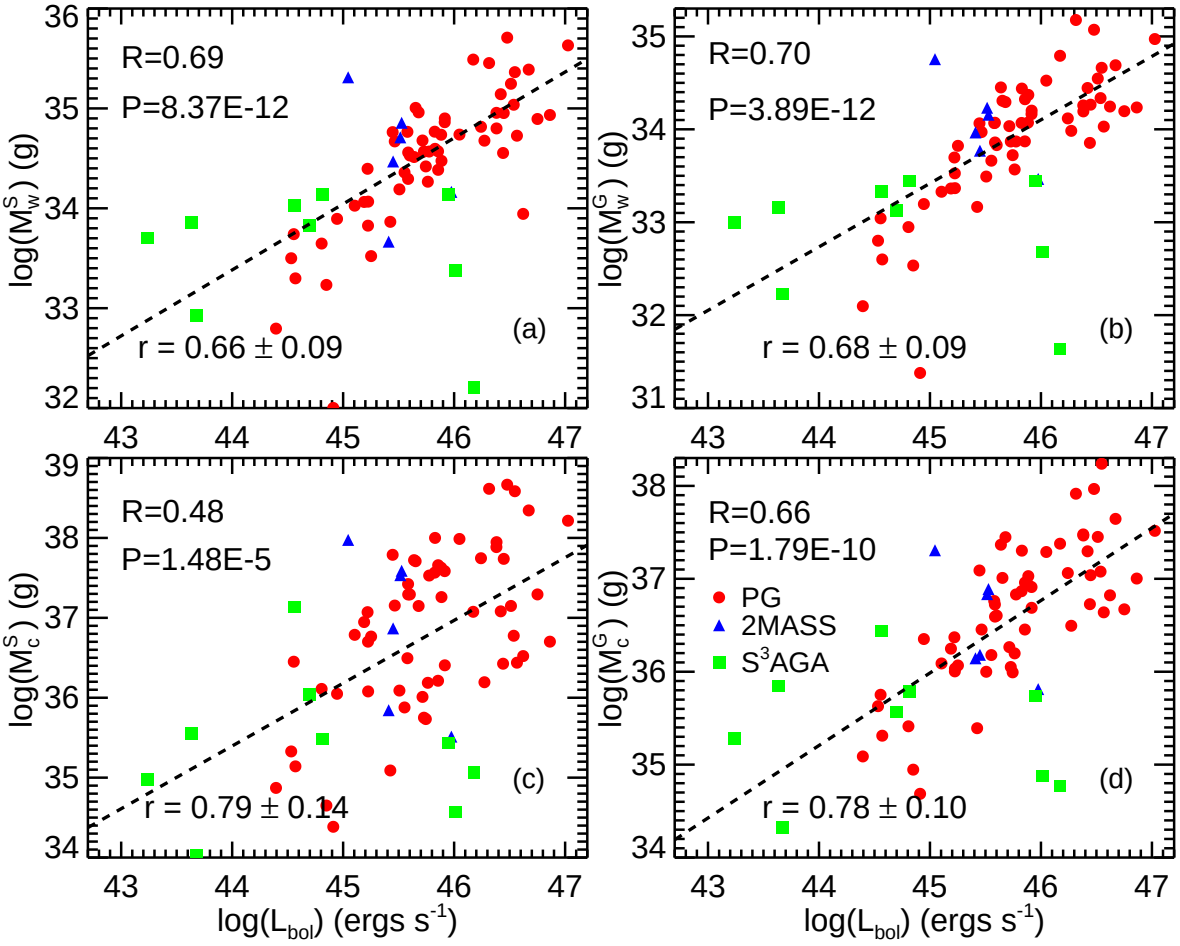


Fig. 12.— Correlation of the bolometric luminosity $L_{\rm bol}$ [approximated by $7 \times \lambda L_\lambda(5100\,\text{Å})$] with the mass of the warm silicate component ($M_{\rm w}^{\rm S}$; a), the warm graphite component ($M_{\rm w}^{\rm G}$; b), the cold silicate component ($M_{\rm c}^{\rm S}$; c), and the cold graphite component ($M_{\rm c}^{\rm G}$; d). In each panel, the PG quasars are shown as red circles, the *2MASS* quasars are shown as blue triangles, and the S$^3$AGA AGNs are shown as green squares. Also labeled in each panel are the Pearson correlation coefficient ($R$) and the probability ($P$) of no correlation as well as the slope of the linear relation (dashed lines).

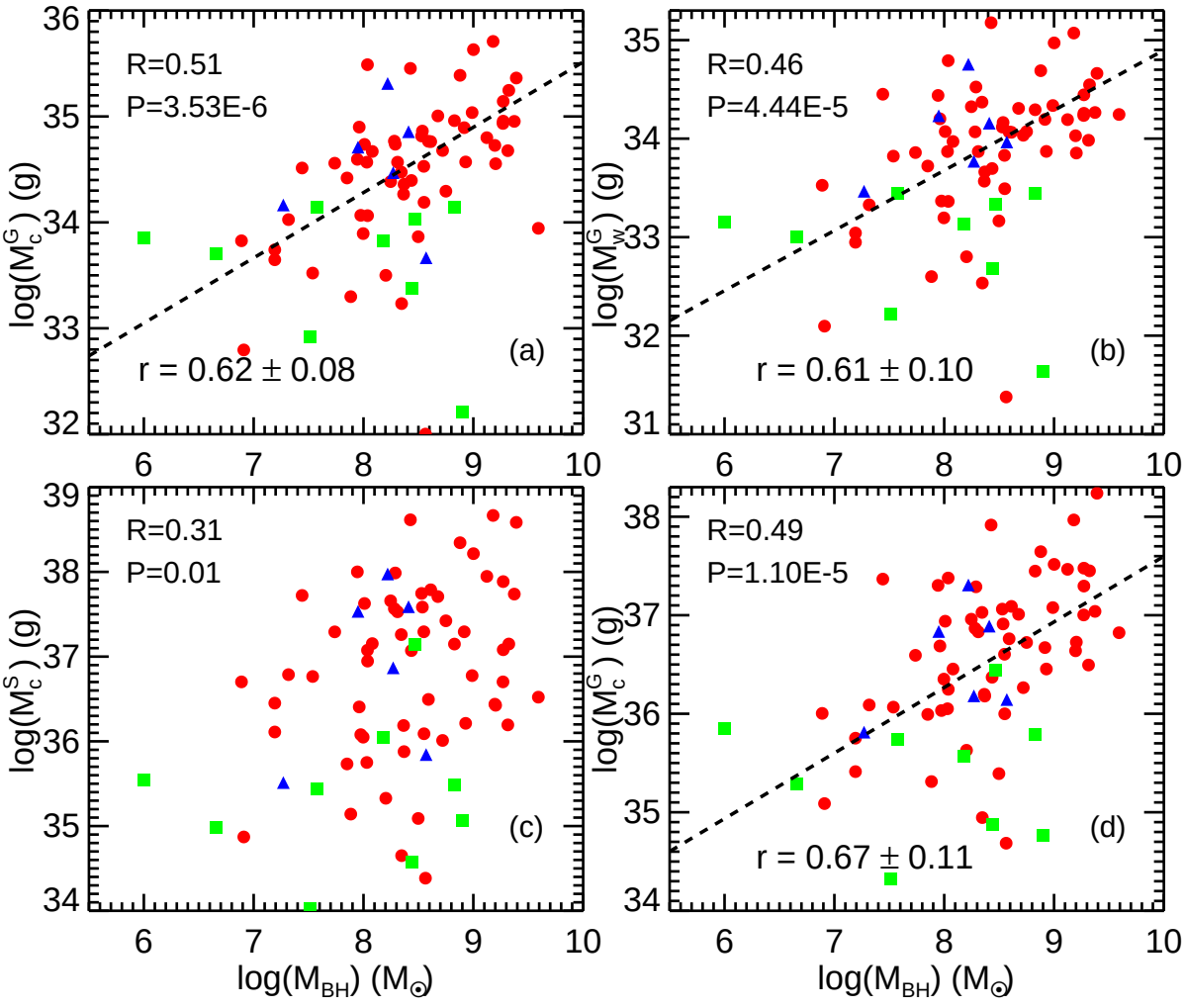


Fig. 13.— Correlation of the black hole mass ($M_{\rm BH}$) with the mass of warm silicate ($M_{\rm w}^{\rm S}$; a), warm graphite ($M_{\rm w}^{\rm G}$; b), cold silicate ($M_{\rm c}^{\rm S}$; c), and cold graphite ($M_{\rm c}^{\rm G}$; d). In each panel, the PG quasars are shown as red circles, the *2MASS* quasars are shown as blue triangles, and the S$^3$AGA AGNs are shown as green squares. The Pearson correlation coefficient ($R$) and the probability ($P$) of no correlation as well as the slope of the linear relation are also labeled in each panel.

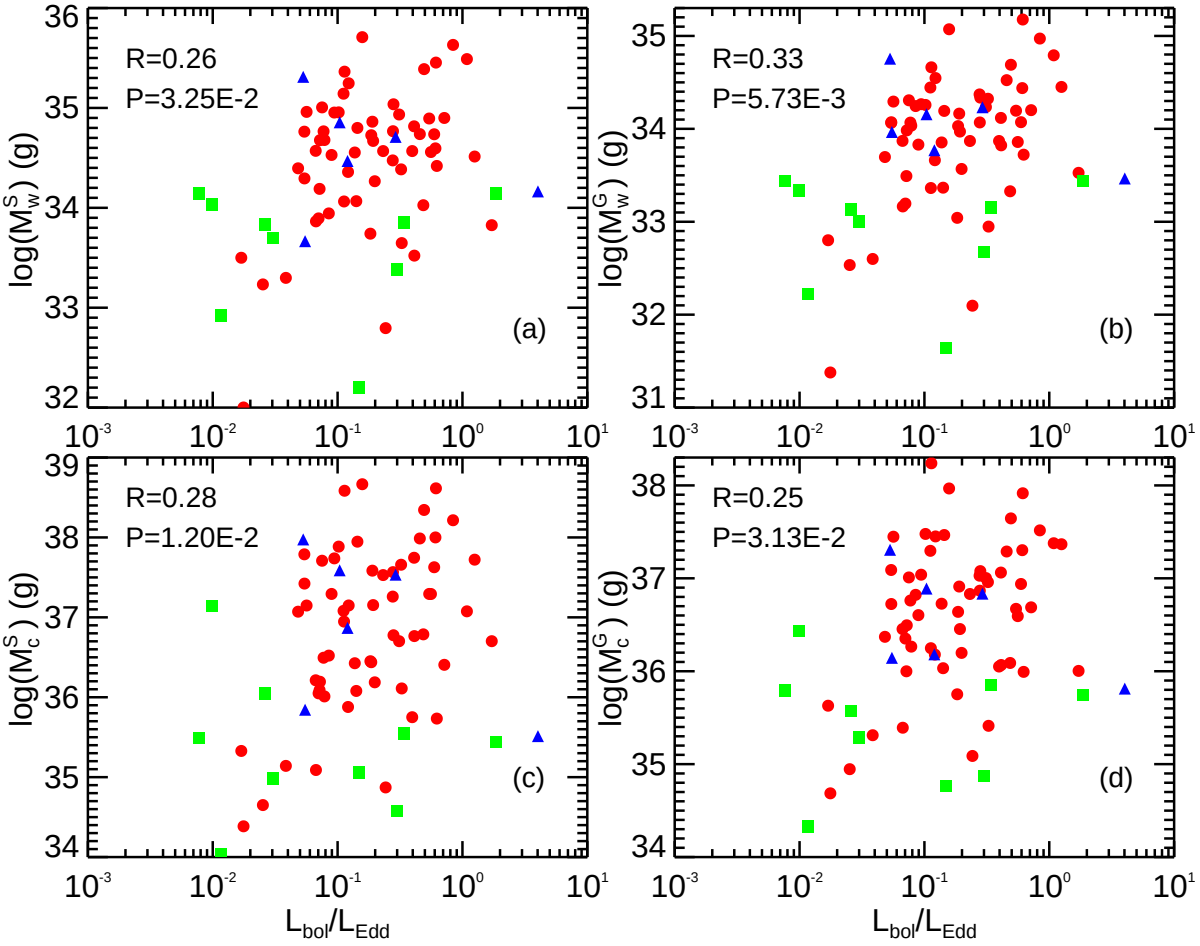


Fig. 14.— Correlation of the Eddington ratio (represented by $L_{\rm bol}/L_{\rm Edd}$) with the mass of warm silicate ($M_{\rm w}^{\rm S}$; a), warm graphite ($M_{\rm w}^{\rm G}$; b), cold silicate ($M_{\rm c}^{\rm S}$; c), and cold graphite ($M_{\rm c}^{\rm G}$; d). In each panel, the PG quasars are shown as red circles, the *2MASS* quasars are shown as blue triangles, and the S$^3$AGA AGNs are shown as green squares.

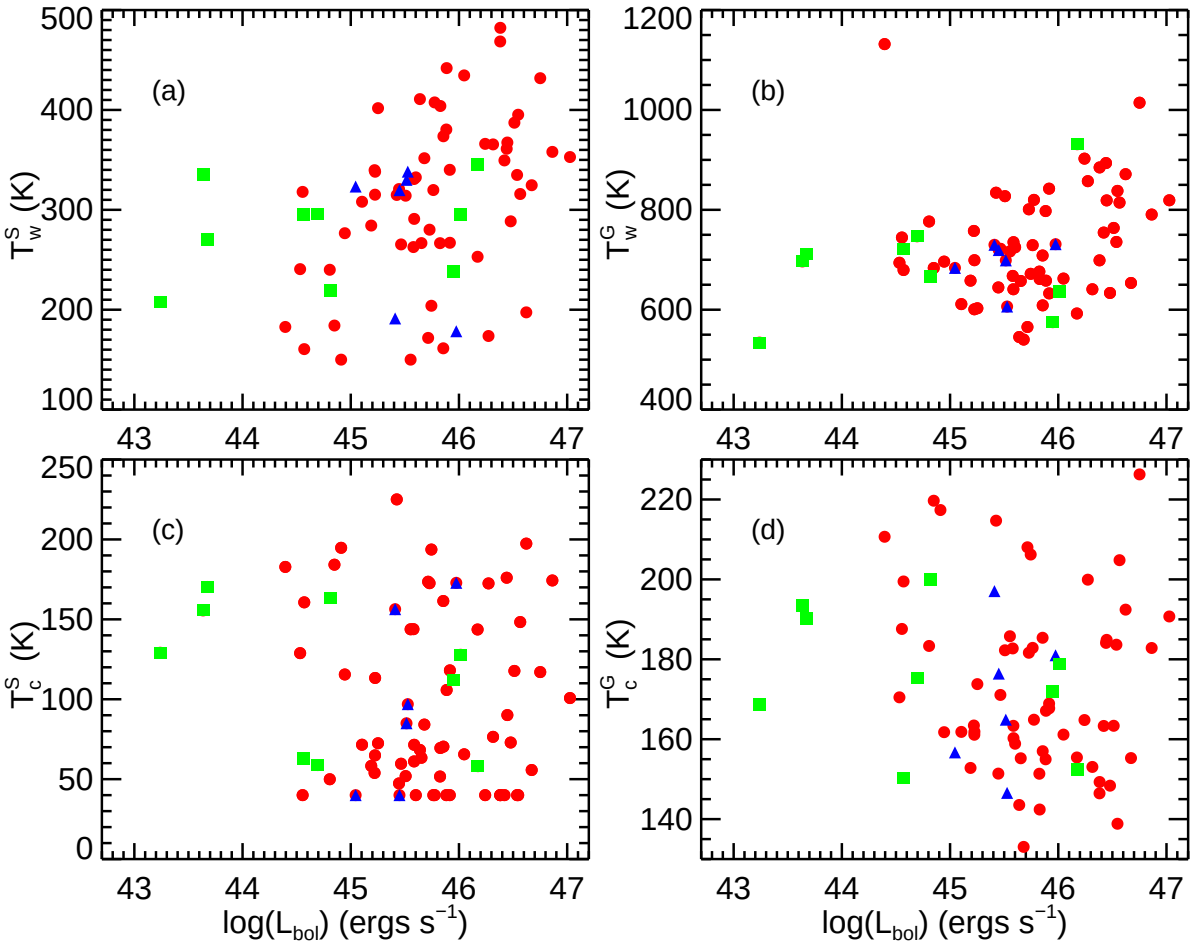


Fig. 15.— Correlation of the bolometric luminosity with the temperature of the warm silicate component ($T_{\rm w}^{\rm S}$; a), the warm graphite component ($T_{\rm w}^{\rm G}$; b), the cold silicate component ($T_{\rm c}^{\rm S}$; c), and the cold graphite component ($T_{\rm c}^{\rm G}$; d). In each panel, the PG quasars are shown as red circles, the *2MASS* quasars are shown as blue triangles, and the S$^3$AGA AGNs are shown as green squares.

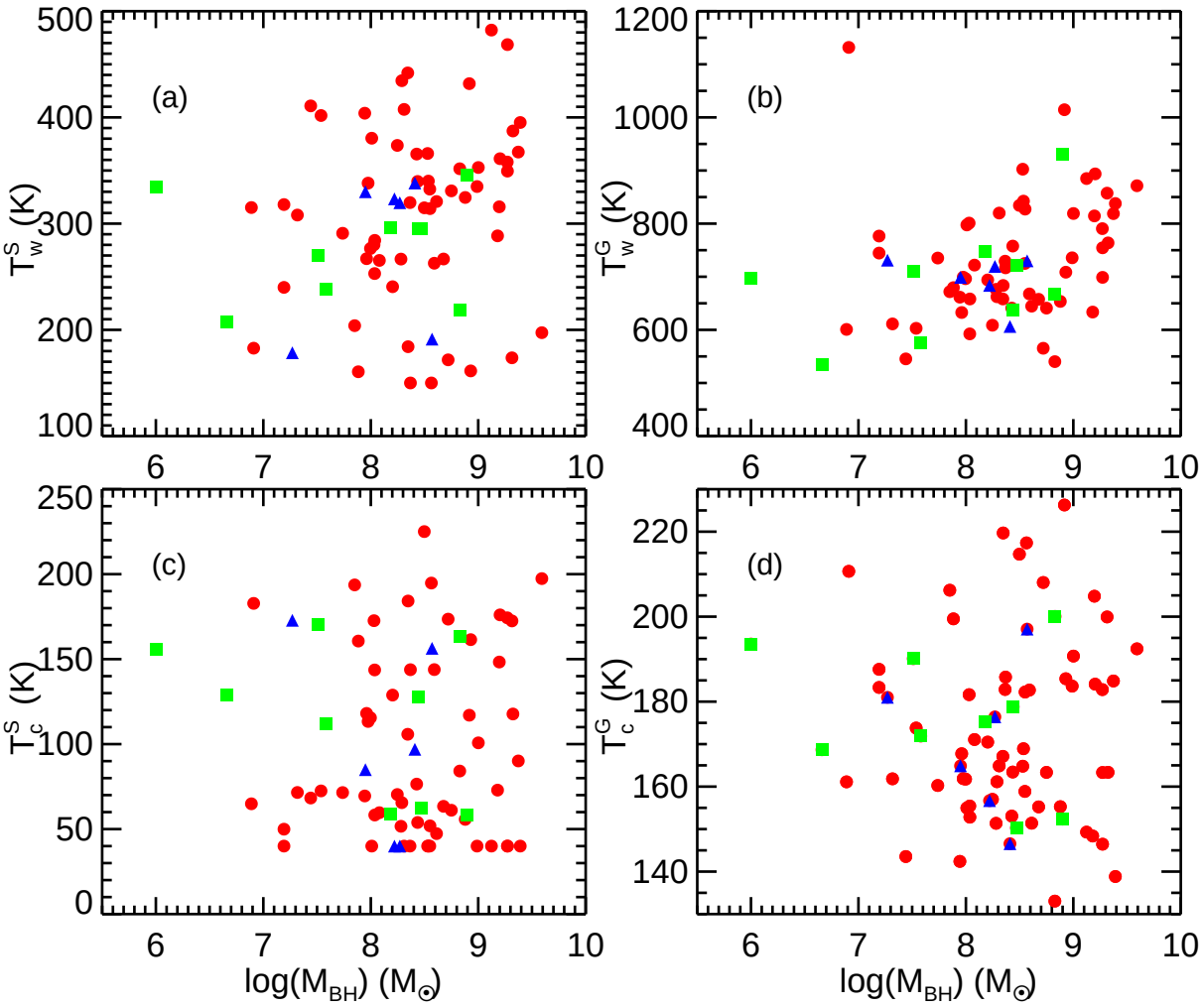


Fig. 16.— Correlation of the black hole mass ($M_{\rm BH}$) with the temperature of warm silicate ($T_{\rm w}^{\rm S}$; a), warm graphite ($T_{\rm w}^{\rm G}$; b), cold silicate ($T_{\rm c}^{\rm S}$; c), and cold graphite ($T_{\rm c}^{\rm G}$; d). In each panel, the PG quasars are shown as red circles, the *2MASS* quasars are shown as blue triangles, and the S$^3$AGA AGNs are shown as green squares.

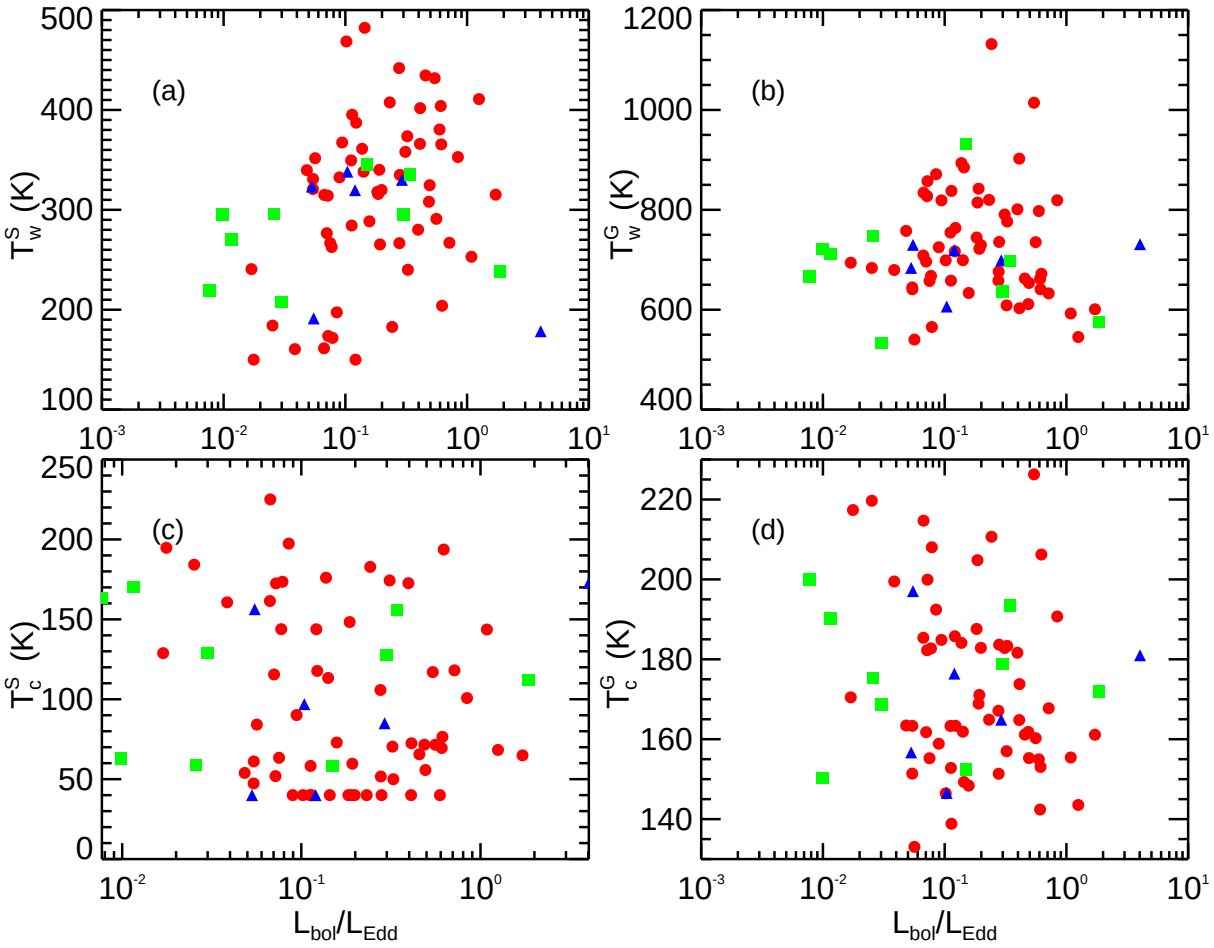


Fig. 17.— Correlation of the Eddington ratio $L_{\rm bol}/L_{\rm Edd}$ with the temperature of warm silicate ($T_{\rm w}^{\rm S}$; a), warm graphite ($T_{\rm w}^{\rm G}$; b), cold silicate ($T_{\rm c}^{\rm S}$; c), and cold graphite ($T_{\rm c}^{\rm G}$; d). In each panel, the PG quasars are shown as red circles, the *2MASS* quasars are shown as blue triangles, and the S$^3$AGA AGNs are shown as green squares.

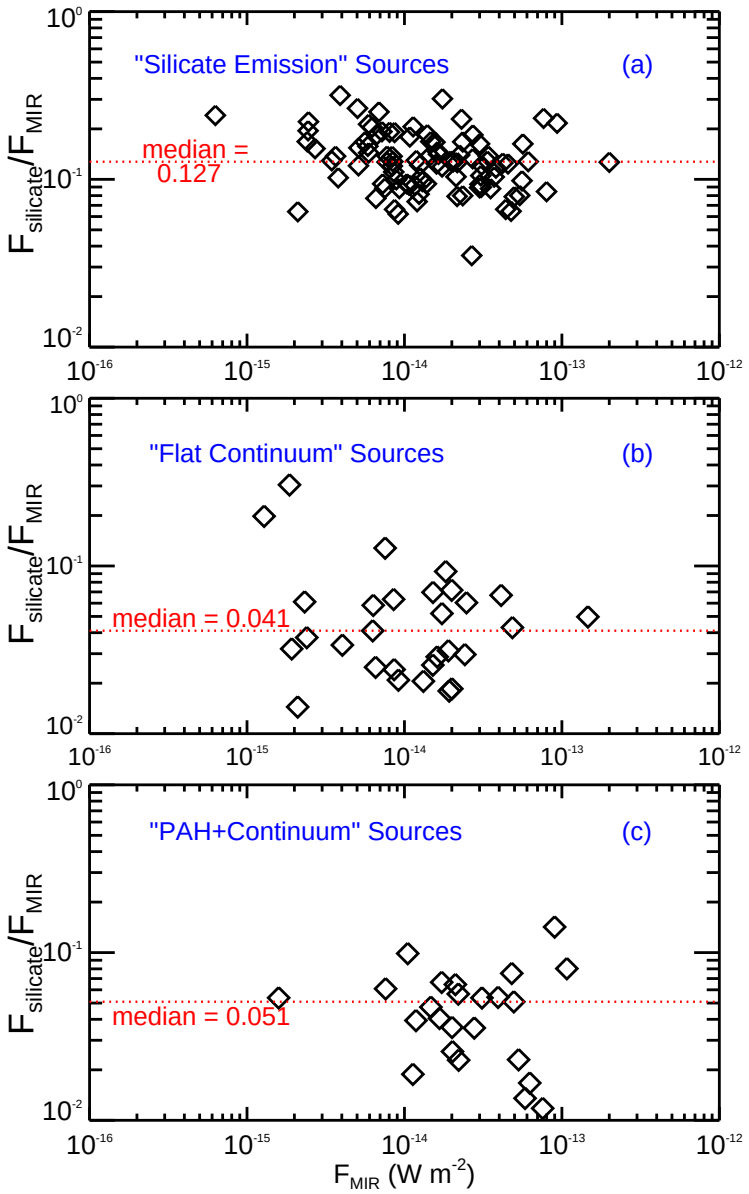


Fig. 18.— Fractional fluxes emitted in the 9.7 and 18 $\mu$m silicate features ($F_{\rm silicate}$) relative to the total mid-IR emission at $\sim$5–38 $\mu$m ($F_{\rm MIR}$) for the "silicate emission" sources (a), the "flat continuum" sources (b), and the "PAH + continuum" sources (c). For the latter two classes of sources, $F_{\rm silicate}$ is actually an upper limit. The dashed horizontal line shows the mean fraction $\langle F_{\rm silicate}/F_{\rm MIR}\rangle$.

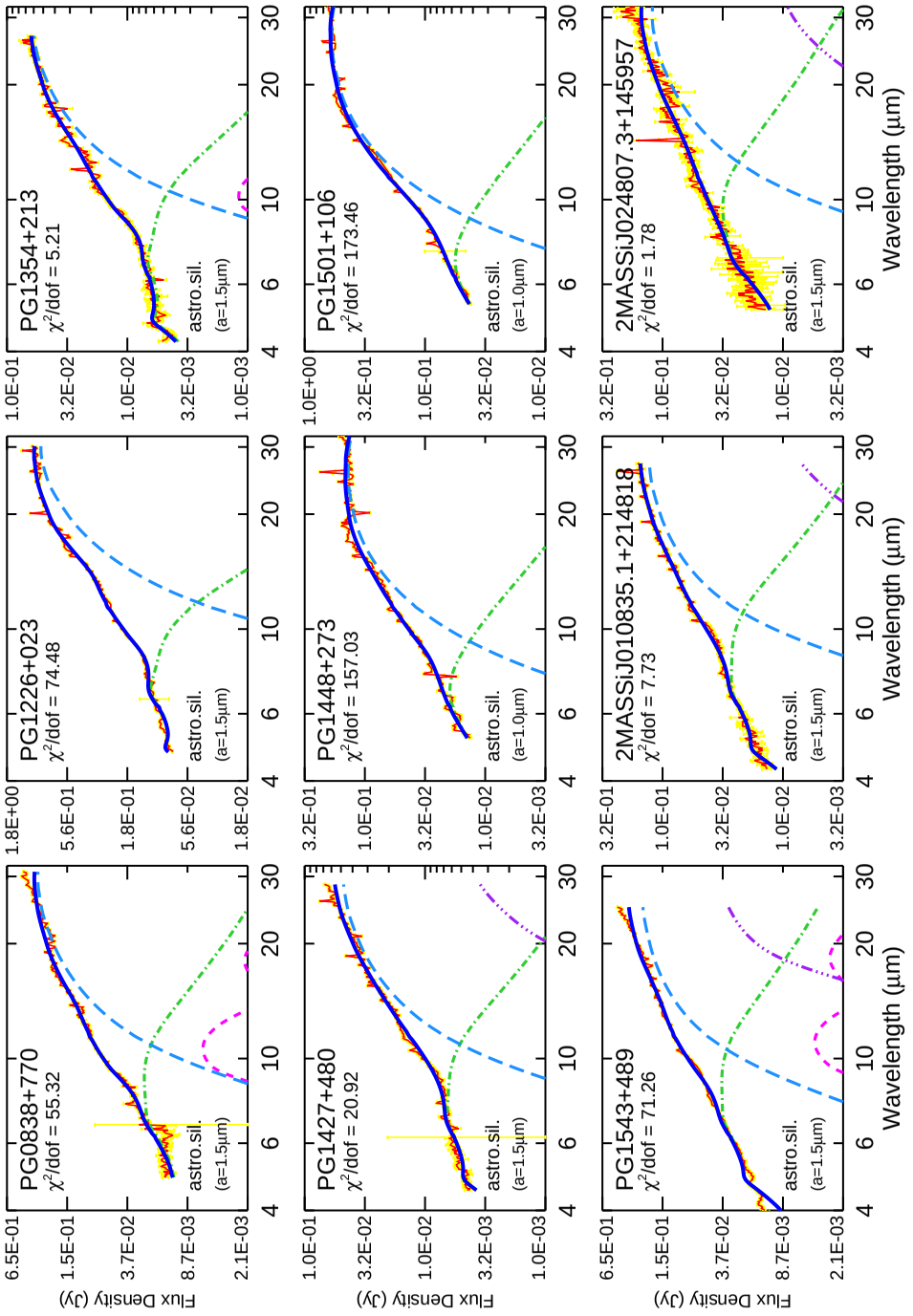


Fig. 19.— Comparison of the *Spitzer*/IRS spectra (red solid lines) of the PG quasars PG0838+770, PG1226+023, PG1354+213, PG1427+480, PG1448+273, PG1501+106, PG1543+489 and the *2MASS* quasars 2MASSiJ010835.1+214818 and 2MASSiJ024807.3+145957 which show a featureless thermal continuum with the model spectra (blue solid lines) which are the sum of warm silicate (magenta short dashed lines), cold silicate (purple dash-dot-dotted lines), warm graphite (green dash-dotted lines), and cold graphite (light blue long dashed lines). Also shown are the observed $1\sigma$ errors (yellow vertical lines).

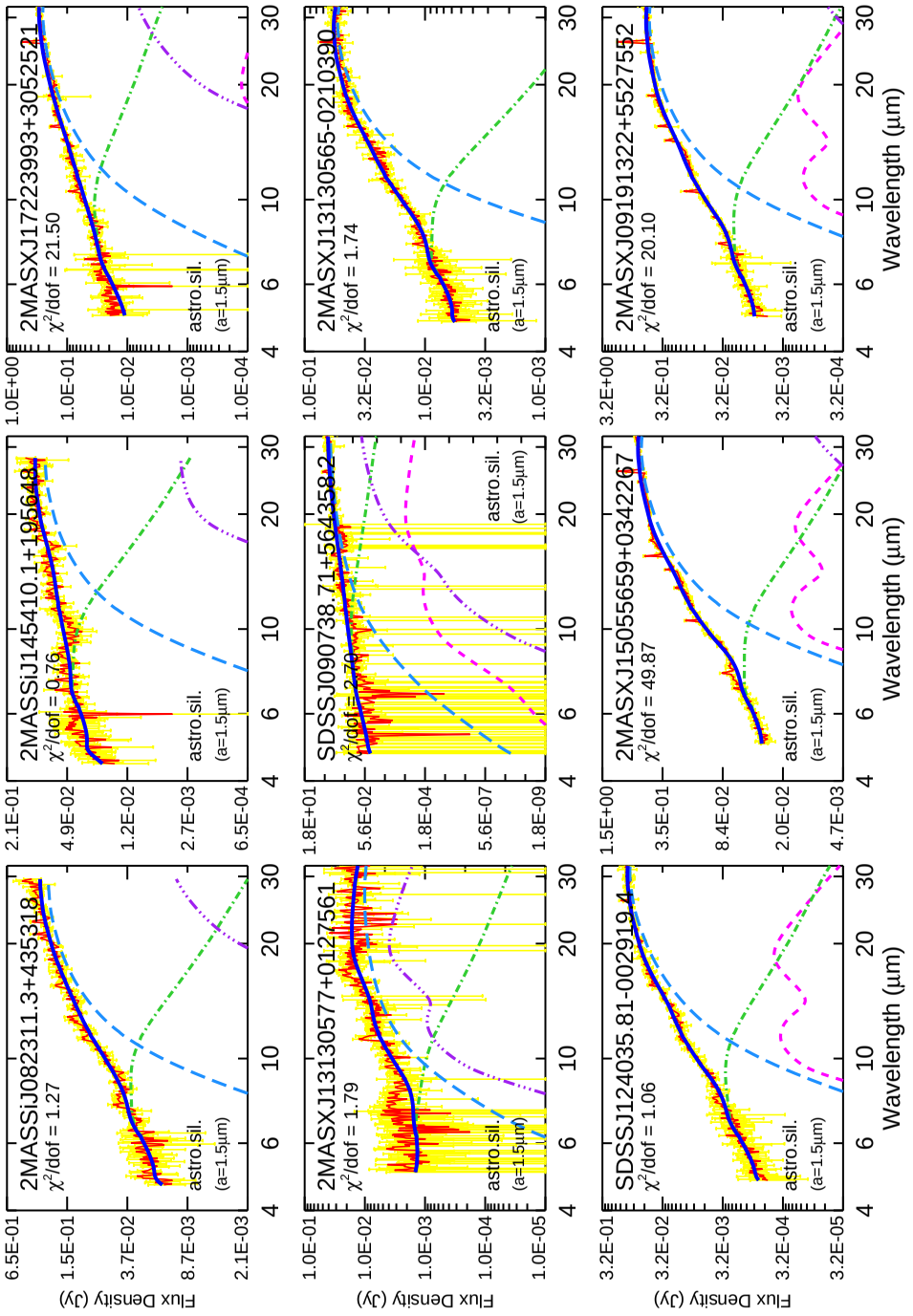


Fig. 19.— Continued, but for the *2MASS* quasars 2MASSiJ082311.3+435318, and 2MASSiJ145410.1+195648 and the S$^3$AGA AGNs 2MASXJ17223993+3052521, 2MASXJ13130577+0127561, SDSSJ090738.71+564358.2, 2MASXJ13130565-0210390, SDSSJ124035.81-002919.4, 2MASXJ15055659+0342267, and 2MASXJ09191322+5527552.

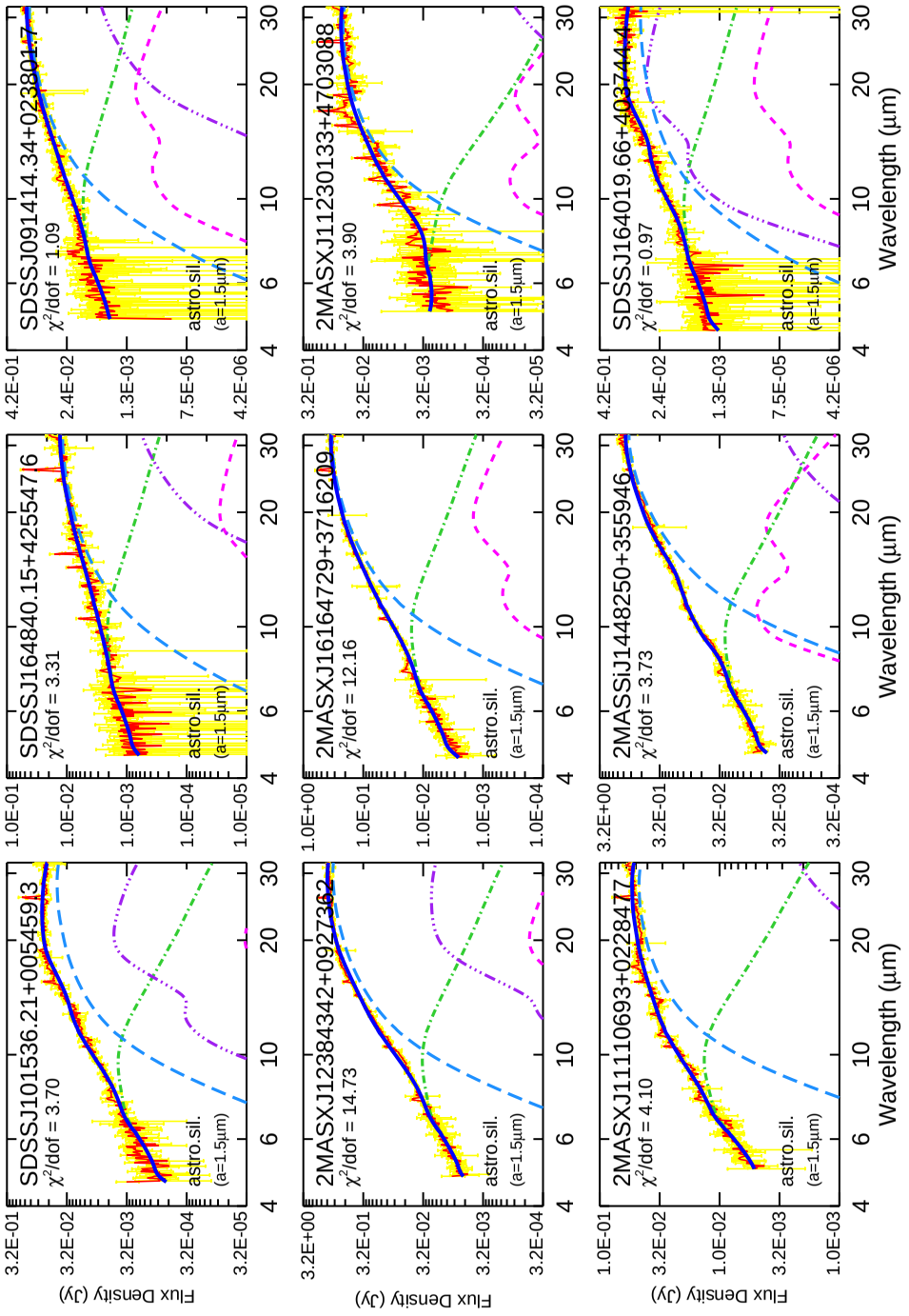


Fig. 19.— Continued, but for the S$^3$AGA AGNs, SDSSJ101536.21+005459.3, SDSSJ164840.15+425547.6, SDSSJ091414.34+023801.7, 2MASXJ12384342+0927362, 2MASXJ16164729+3716209, 2MASXJ11230133+4703088, 2MASXJ11110693+0228477, 2MASSiJ1448250+355946, and SDSSJ164019.66+403744.4.

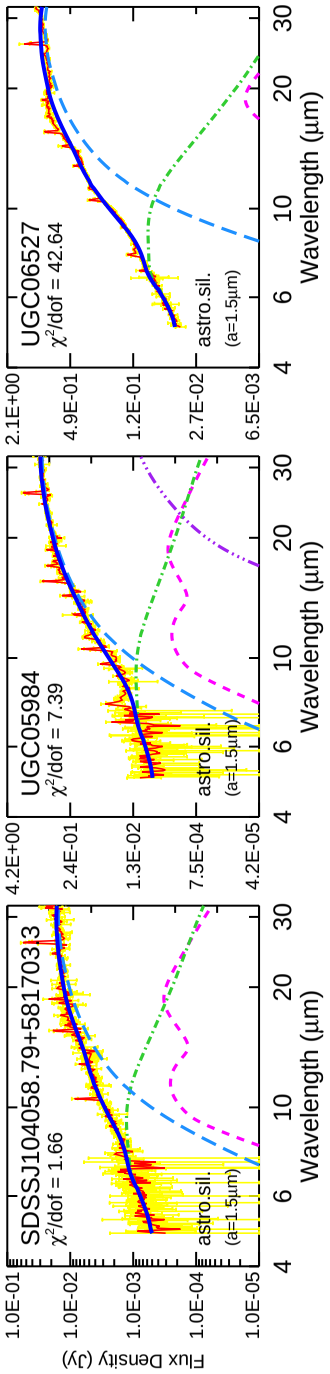


Fig. 19.— Continued, but for the S$^3$AGA AGNs SDSSJ104058.79+581703.3, UGC05984 and UGC06527.

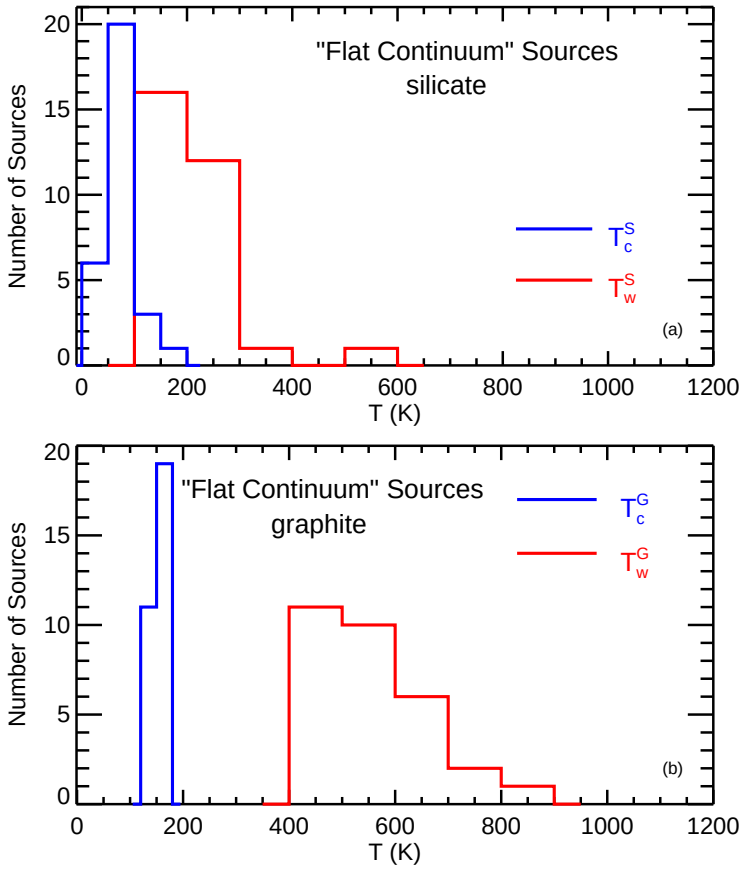


Fig. 20.— Same as Figure 8 but for those 30 "flat continuum" sources which show a featureless thermal continuum.

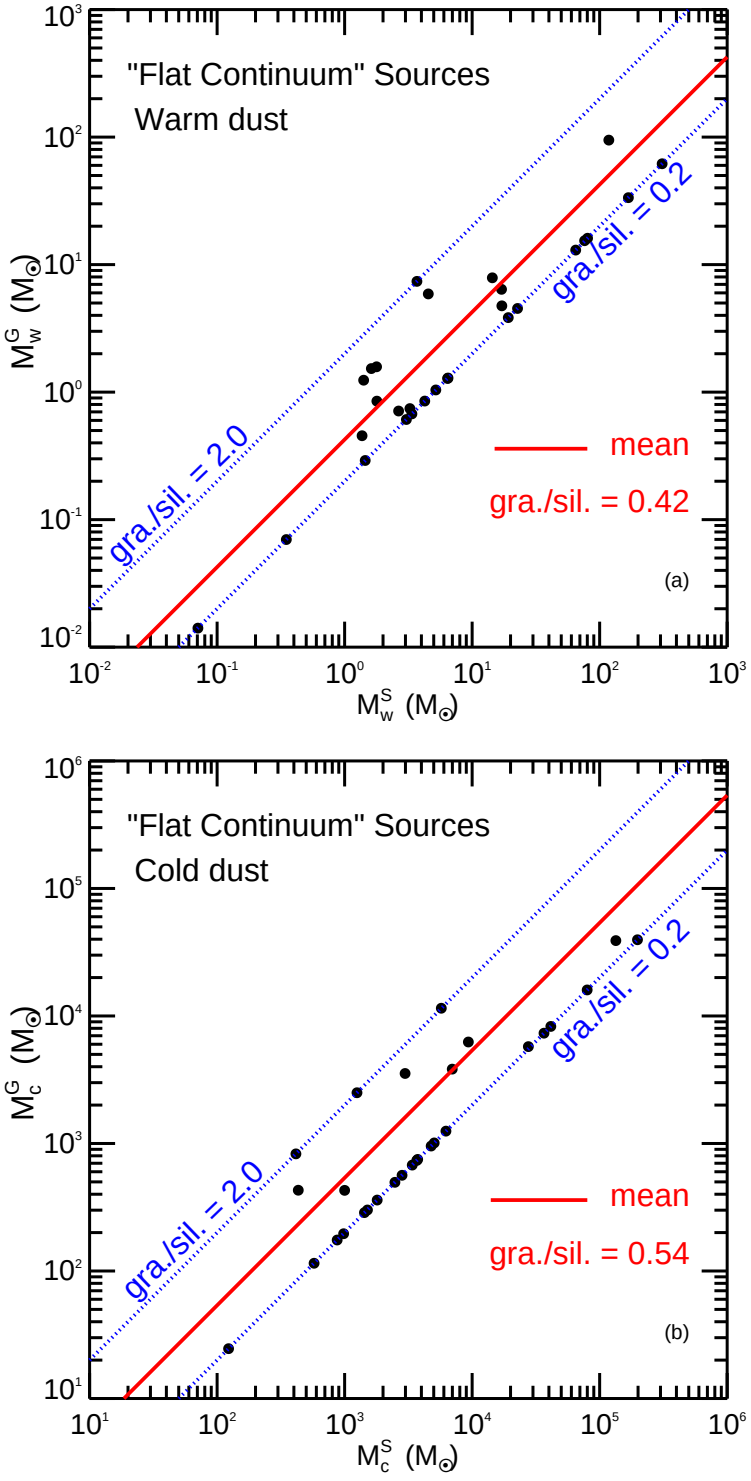


Fig. 21.— Same as Figure 10 but for the 30 "flat continuum" sources which show a featureless thermal continuum.

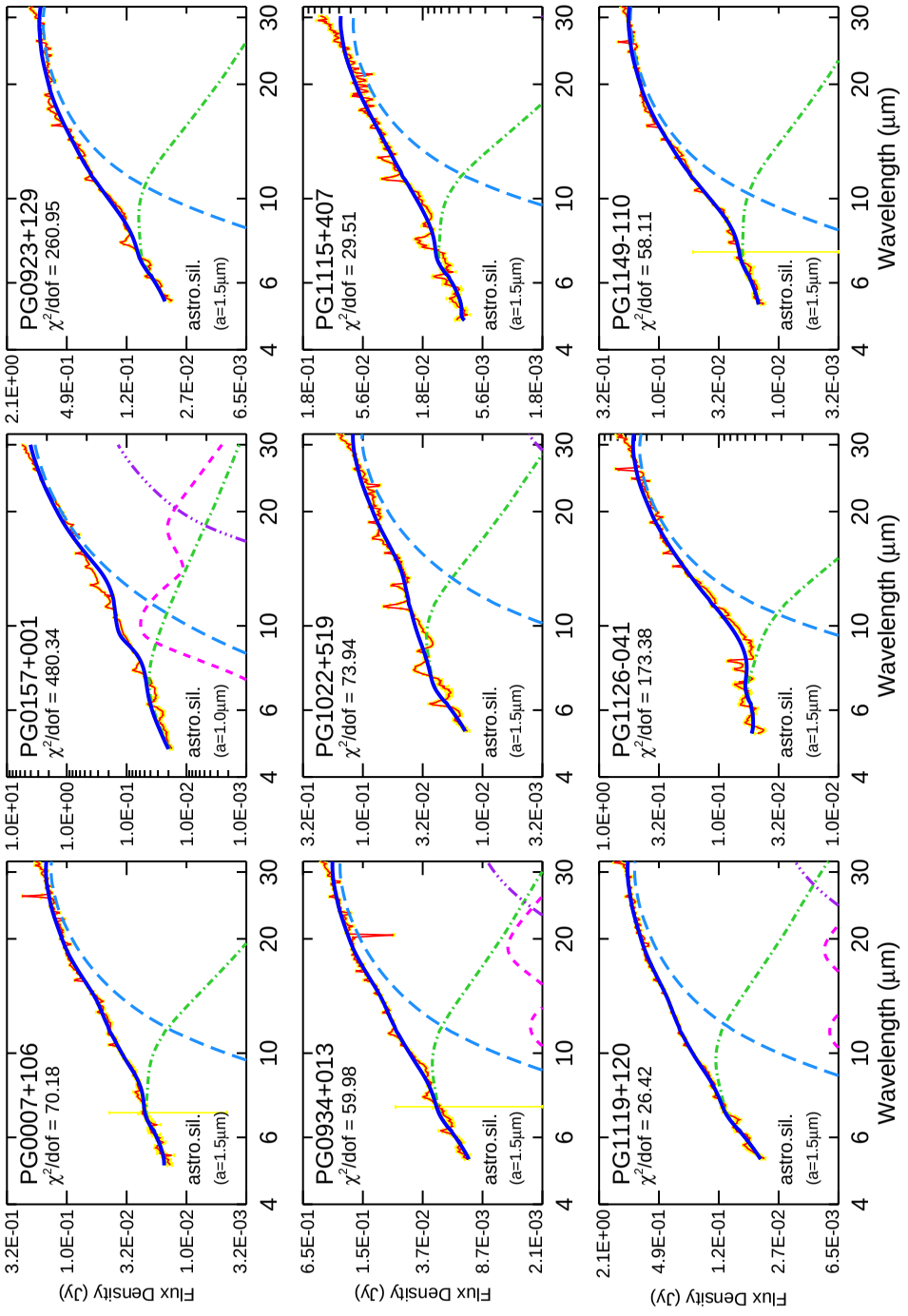


Fig. 22.— Comparison of the *Spitzer*/IRS spectra (red solid lines) of the PG quasars PG0007+106, PG0157+001, PG0923+129, PG0934+013, PG1022+519, PG1115+407, PG1119+120, PG1126-041, and PG1149-110 which show a thermal continuum superimposed by PAH features with the model spectra (blue solid lines) which are the sum of warm silicate (magenta short dashed lines), cold silicate (purple dash-dot-dotted lines), warm graphite (green dash-dotted lines), and cold graphite (light blue long dashed lines). Also shown are the observed $1\sigma$ errors (yellow vertical lines).

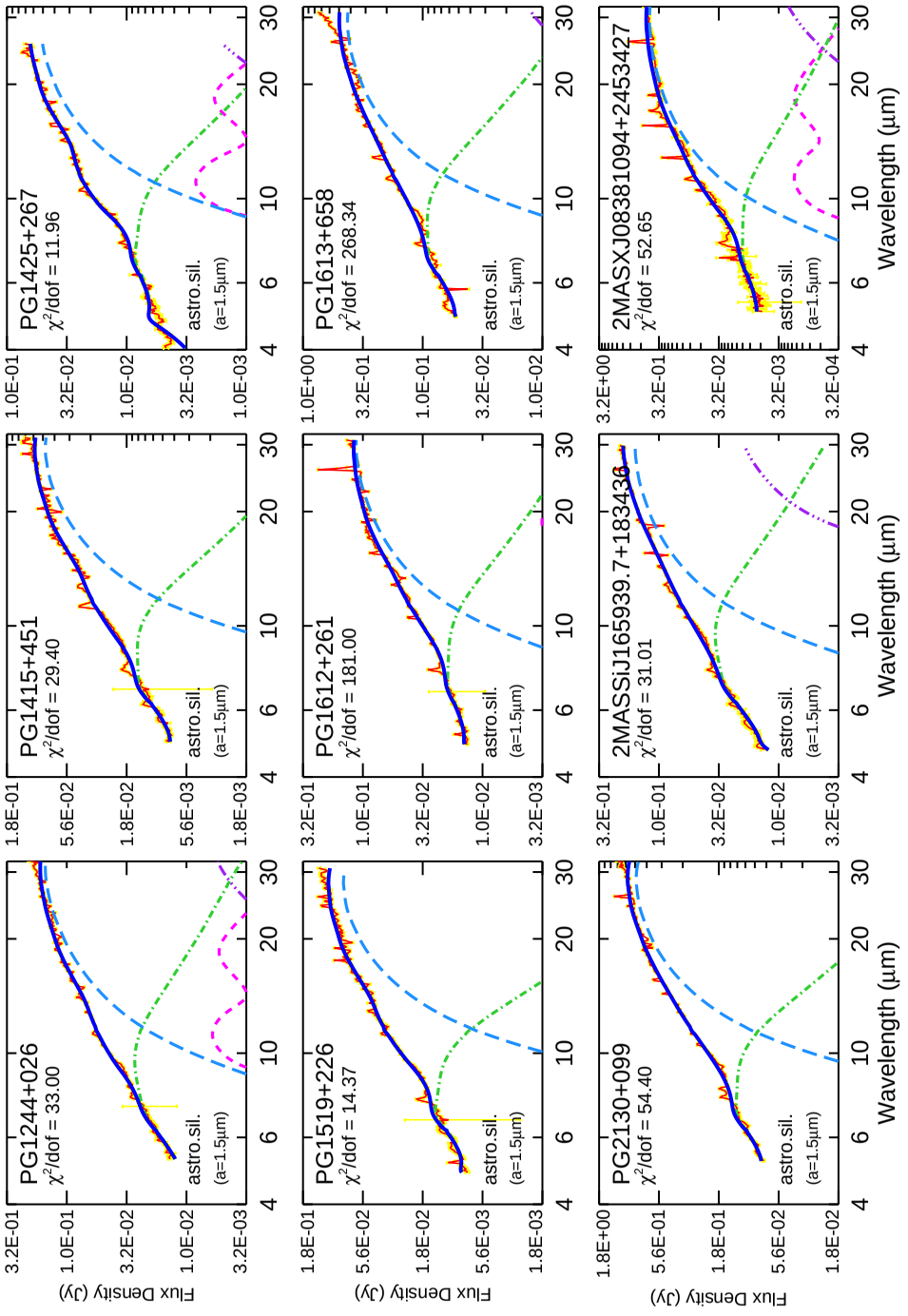


Fig. 22.— Continued, but for the PG quasars PG1244+026, PG1415+451, PG1425+267, PG1519+226, PG1612+261, PG1613+658, PG2130+099, the *2MASS* quasar 2MASSiJ165939.7+183436, and the S$^3$AGA AGN 2MASXJ08381094+2453427.

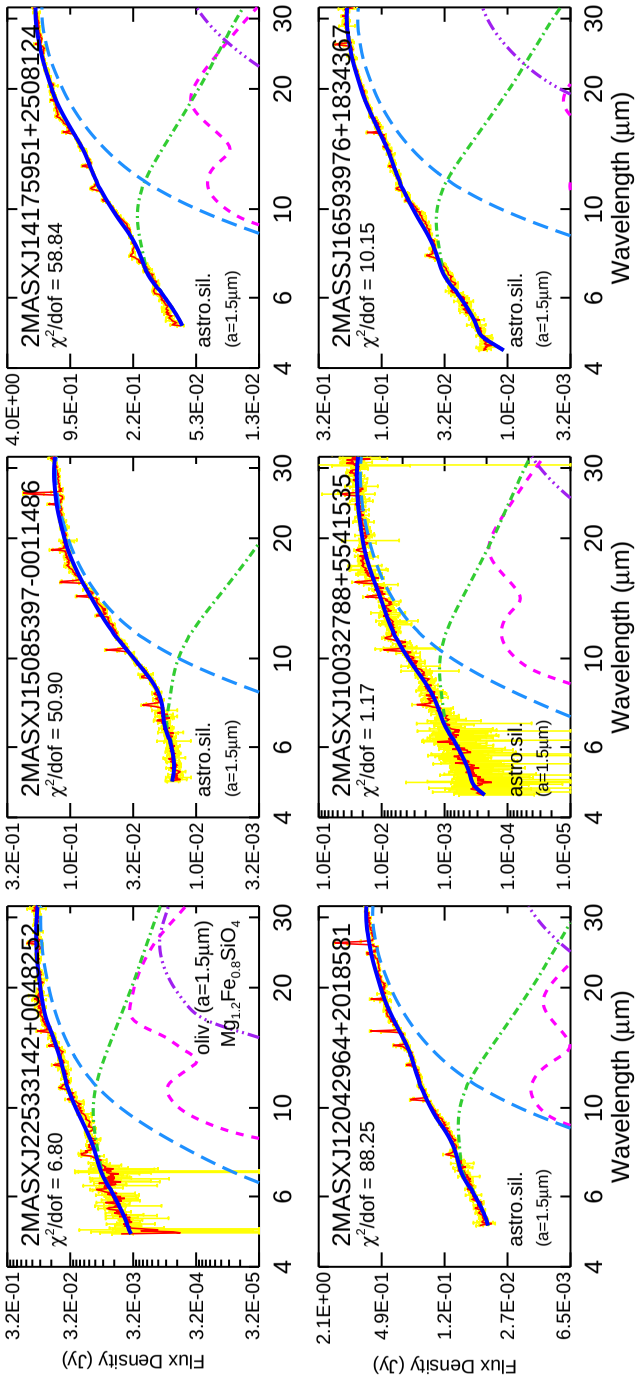


Fig. 22.— Continued, but for the S$^3$AGA AGNs 2MASXJ22533142+0048252, 2MASXJ15085397-0011486, 2MASXJ14175951+2508124, 2MASXJ12042964+2018581, 2MASXJ10032788+5541535, and 2MASSJ16593976+1834367.

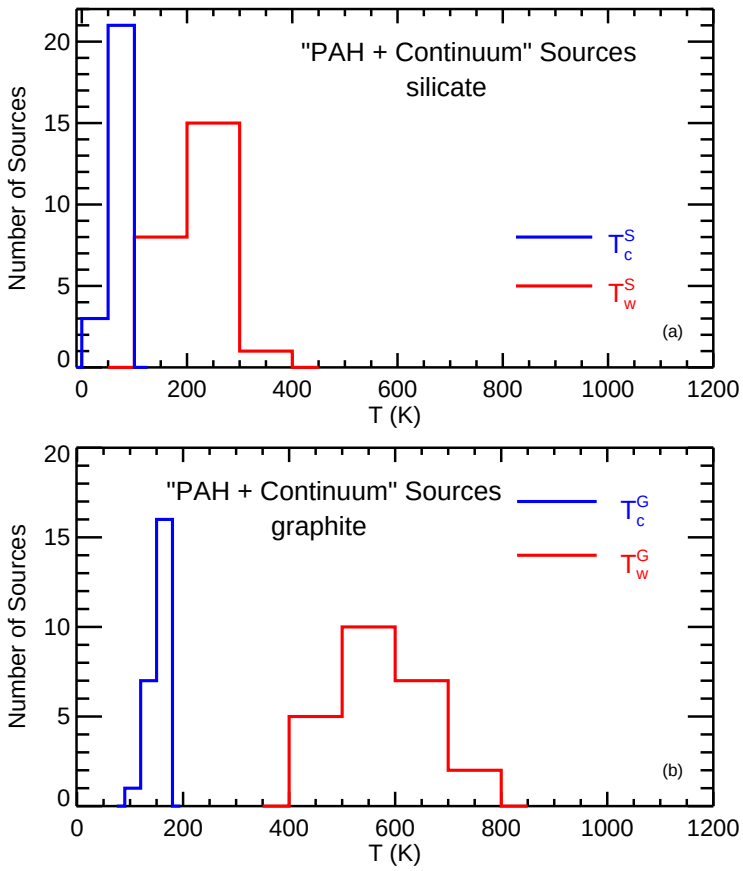


Fig. 23.— Same as Figure 8 but for those 24 sources which show a thermal continuum superimposed with PAH features.

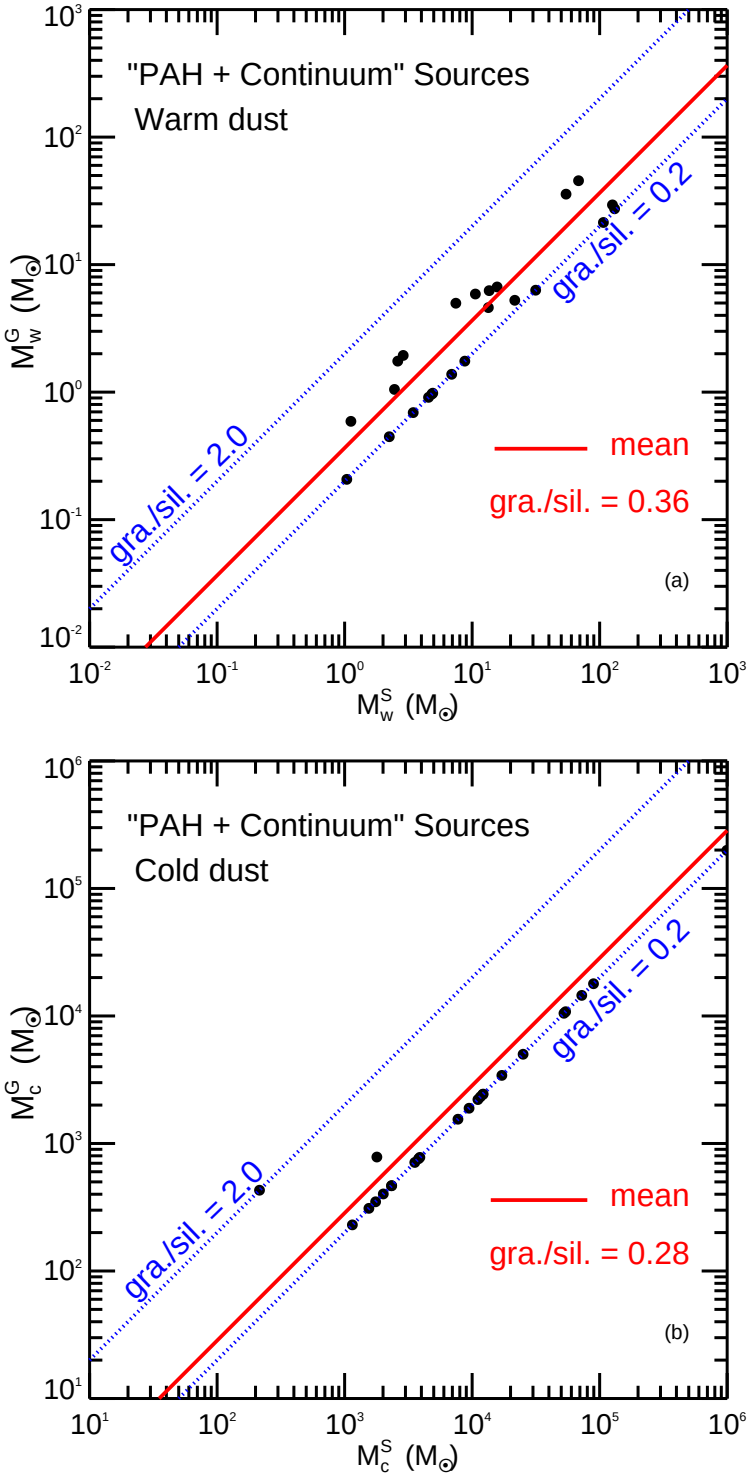


Fig. 24.— Same as Figure 10 but for the 24 sources which show a featureless thermal continuum superimposed with PAH features.

Table 4. Basic Parameters of All 93 Sources from Our PG Quasar Sample, *2MASS* Quasar Sample, and S$^3$AGA AGN Sample. These Sources All Show Silicate Emission around 9.7 and 18 $\mu$m.

| Source | R.A. | Dec. | Redshift | Type | $\lambda L_\lambda(5100\text{Å})$ ($\mathrm{ergs\,s^{-1}}$) | $\lg(M_{\rm BH})$ ($M_\odot$) | Reference |
|---|---|---|---|---|---|---|---|
| (1) | (2) | (3) | (4) | (5) | (6) | (7) | (8) |
| PG0003+158 | 00h05m59.20s | +16d09m49.0s | 0.450 | 1.0 | $46.018^{+0.033}_{-0.036}$ | $9.270^{+0.088}_{-0.110}$ | Ves2006 |
| PG0003+199 | 00h06m19.52s | +20d12m10.5s | 0.025 | 1.0 | $43.710^{+0.011}_{-0.011}$ | $7.192^{+0.081}_{-0.099}$ | Mar2003 |
| PG0026+129 | 00h29m13.60s | +13d16m03.0s | 0.142 | 1.0 | $44.900^{+0.070}_{-0.070}$ | $7.850^{+0.120}_{-0.120}$ | N1987, Kaspi2000 |
| PG0043+039 | 00h45m47.27s | +04d10m24.4s | 0.384 | 1.0 | $45.537^{+0.030}_{-0.032}$ | $9.123^{+0.085}_{-0.105}$ | Ves2006 |
| PG0049+171 | 00h51m54.80s | +17d25m58.4s | 0.064 | 1.0 | $44.004^{+0.011}_{-0.011}$ | $8.347^{+0.079}_{-0.097}$ | Ves2006 |
| PG0050+124 | 00h53m34.94s | +12d41m36.2s | 0.061 | 1.0 | $44.794^{+0.097}_{-0.126}$ | $7.441^{+0.093}_{-0.119}$ | Ves2006 |
| PG0052+251 | 00h54m52.10s | +25d25m38.0s | 0.155 | 1.0 | $44.870^{+0.070}_{-0.070}$ | $8.720^{+0.100}_{-0.100}$ | N1987, Kaspi2000 |
| PG0804+761 | 08h10m58.60s | +76d02m42.0s | 0.100 | 1.0 | $44.930^{+0.070}_{-0.070}$ | $8.310^{+0.010}_{-0.010}$ | N1987, Kaspi2000 |
| PG0844+349 | 08h47m42.40s | +34d45m04.0s | 0.064 | 1.0 | $44.380^{+0.010}_{-0.010}$ | $7.975^{+0.082}_{-0.101}$ | Mar2003 |
| PG0921+525 | 09h25m12.87s | +52d17m10.5s | 0.035 | 1.0 | $43.550^{+0.120}_{-0.120}$ | $6.910^{+0.120}_{-0.120}$ | SG1983, WPM1999 |
| PG0923+201 | 09h25m54.72s | +19d54m05.1s | 0.190 | 1.0 | $45.038^{+0.018}_{-0.019}$ | $8.009^{+0.082}_{-0.101}$ | Ves2006 |
| PG0947+396 | 09h50m48.39s | +39d26m50.5s | 0.206 | 1.0 | $44.808^{+0.020}_{-0.021}$ | $8.677^{+0.081}_{-0.099}$ | Ves2006 |
| PG0953+414 | 09h56m52.39s | +41d15m22.3s | 0.239 | 1.0 | $45.300^{+0.060}_{-0.060}$ | $8.270^{+0.060}_{-0.090}$ | Ves2002 |
| PG1001+054 | 10h04m20.14s | +05d13m00.5s | 0.161 | 1.0 | $44.711^{+0.017}_{-0.017}$ | $7.738^{+0.081}_{-0.099}$ | Ves2006 |
| PG1004+130 | 10h07m26.10s | +12d48m56.2s | 0.240 | 1.0 | $45.536^{+0.022}_{-0.023}$ | $9.272^{+0.084}_{-0.104}$ | Ves2006 |
| PG1011-040 | 10h14m20.69s | -04d18m40.5s | 0.058 | 1.0 | $44.259^{+0.012}_{-0.012}$ | $7.317^{+0.079}_{-0.097}$ | Ves2006 |
| PG1012+008 | 10h14m54.90s | +00d33m37.4s | 0.185 | 1.0 | $45.011^{+0.021}_{-0.022}$ | $8.247^{+0.082}_{-0.101}$ | Ves2006 |
| PG1048-090 | 10h51m29.90s | -09d18m10.0s | 0.344 | 1.0 | $45.596^{+0.027}_{-0.029}$ | $9.203^{+0.085}_{-0.105}$ | Ves2006 |
| PG1049-005 | 10h51m51.44s | -00d51m17.7s | 0.357 | 1.0 | $45.633^{+0.028}_{-0.030}$ | $9.180^{+0.085}_{-0.106}$ | Ves2006 |
| PG1048+342 | 10h51m43.90s | +33d59m26.7s | 0.167 | 1.0 | $44.708^{+0.018}_{-0.019}$ | $8.369^{+0.081}_{-0.099}$ | Ves2006 |
| PG1100+772 | 11h04m13.69s | +76d58m58.0s | 0.313 | 1.0 | $45.575^{+0.026}_{-0.027}$ | $9.272^{+0.085}_{-0.105}$ | Ves2006 |
| PG1103-006 | 11h06m31.77s | -00d52m52.5s | 0.425 | 1.0 | $45.667^{+0.033}_{-0.036}$ | $9.323^{+0.086}_{-0.107}$ | Ves2006 |
| PG1114+445 | 11h17m06.40s | +44d13m33.3s | 0.144 | 1.0 | $44.734^{+0.017}_{-0.017}$ | $8.591^{+0.081}_{-0.099}$ | Ves2006 |
| PG1116+215 | 11h19m08.68s | +21d19m18.0s | 0.177 | 1.0 | $45.397^{+0.018}_{-0.019}$ | $8.529^{+0.083}_{-0.103}$ | Ves2006 |
| PG1121+422 | 11h24m39.18s | +42d01m45.0s | 0.234 | 1.0 | $44.883^{+0.022}_{-0.023}$ | $8.030^{+0.081}_{-0.100}$ | Ves2006 |
| PG1151+117 | 11h53m49.27s | +11d28m30.4s | 0.176 | 1.0 | $44.756^{+0.020}_{-0.021}$ | $8.549^{+0.081}_{-0.099}$ | Ves2006 |
| PG1202+281 | 12h04m42.11s | +27d54m11.8s | 0.165 | 1.0 | $44.601^{+0.027}_{-0.029}$ | $8.612^{+0.081}_{-0.099}$ | Ves2006 |
| PG1211+143 | 12h14m17.70s | +14d03m12.6s | 0.085 | 1.0 | $45.071^{+0.014}_{-0.014}$ | $7.961^{+0.082}_{-0.101}$ | Ves2006 |
| PG1216+069 | 12h19m20.93s | +06d38m38.5s | 0.334 | 1.0 | $45.721^{+0.027}_{-0.028}$ | $9.196^{+0.085}_{-0.106}$ | Ves2006 |
| PG1229+204 | 12h32m03.60s | +20d09m29.2s | 0.063 | 1.0 | $44.100^{+0.012}_{-0.012}$ | $7.997^{+0.080}_{-0.098}$ | Mar2003 |
| PG1259+593 | 13h01m12.93s | +59d02m06.7s | 0.472 | 1.0 | $45.906^{+0.034}_{-0.037}$ | $8.917^{+0.087}_{-0.109}$ | Ves2006 |
| PG1302-102 | 13h05m33.01s | -10d33m19.4s | 0.286 | 1.0 | $45.827^{+0.024}_{-0.026}$ | $8.879^{+0.086}_{-0.107}$ | Ves2006 |
| PG1307+085 | 13h09m47.00s | +08d19m48.2s | 0.155 | 1.0 | $45.010^{+0.028}_{-0.028}$ | $8.930^{+0.096}_{-0.123}$ | Mar2003 |
| PG1309+355 | 13h12m17.80s | +35d15m21.0s | 0.183 | 1.0 | $45.041^{+0.019}_{-0.020}$ | $8.344^{+0.082}_{-0.100}$ | Ves2006 |
| PG1310-108 | 13h13m05.78s | -11d07m42.4s | 0.035 | 1.0 | $43.725^{+0.010}_{-0.011}$ | $7.884^{+0.079}_{-0.097}$ | Ves2006 |
| PG1322+659 | 13h23m49.52s | +65d41m48.2s | 0.168 | 1.0 | $44.980^{+0.098}_{-0.126}$ | $8.281^{+0.094}_{-0.120}$ | Ves2006 |
| PG1341+258 | 13h43m56.75s | +25d38m47.7s | 0.087 | 1.0 | $44.344^{+0.097}_{-0.126}$ | $8.037^{+0.092}_{-0.117}$ | Ves2006 |
| PG1351+640 | 13h53m15.83s | +63d45m45.7s | 0.087 | 1.0 | $44.835^{+0.014}_{-0.015}$ | $8.828^{+0.081}_{-0.099}$ | Ves2006 |
| PG1352+183 | 13h54m35.69s | +18d05m17.5s | 0.158 | 1.0 | $44.816^{+0.017}_{-0.017}$ | $8.423^{+0.081}_{-0.099}$ | Ves2006 |
| PG1402+261 | 14h05m16.21s | +25d55m34.1s | 0.164 | 1.0 | $44.983^{+0.017}_{-0.018}$ | $7.944^{+0.081}_{-0.100}$ | Ves2006 |
| PG1404+226 | 14h06m21.89s | +22d23m46.6s | 0.098 | 1.0 | $44.379^{+0.017}_{-0.018}$ | $6.889^{+0.080}_{-0.098}$ | Ves2006 |
| PG1411+442 | 14h13m48.33s | +44d00m14.0s | 0.089 | 1.0 | $44.620^{+0.014}_{-0.014}$ | $8.080^{+0.086}_{-0.107}$ | Mar2003 |
| PG1416-129 | 14h19m03.80s | -13d10m44.0s | 0.129 | 1.0 | $45.135^{+0.037}_{-0.041}$ | $9.045^{+0.083}_{-0.103}$ | Ves2006 |
| PG1426+015 | 14h29m06.59s | +01d17m06.5s | 0.086 | 1.0 | $44.740^{+0.070}_{-0.070}$ | $8.750^{+0.100}_{-0.100}$ | N1987, Kaspi2000 |
| PG1435-067 | 14h38m16.16s | -06d58m21.3s | 0.129 | 1.0 | $44.918^{+0.036}_{-0.040}$ | $8.365^{+0.082}_{-0.102}$ | Ves2006 |
| PG1444+407 | 14h46m45.94s | +40d35m05.8s | 0.267 | 1.0 | $45.203^{+0.023}_{-0.024}$ | $8.289^{+0.083}_{-0.102}$ | Ves2006 |
| PG1512+370 | 15h14m43.04s | +36d50m50.4s | 0.371 | 1.0 | $45.602^{+0.030}_{-0.032}$ | $9.373^{+0.085}_{-0.106}$ | Ves2006 |
| PG1534+580 | 15h35m52.36s | +57d54m09.2s | 0.030 | 1.0 | $43.687^{+0.010}_{-0.011}$ | $8.203^{+0.080}_{-0.097}$ | Ves2006 |
| PG1535+547 | 15h36m38.36s | +54d33m33.2s | 0.038 | 1.0 | $43.961^{+0.010}_{-0.011}$ | $7.192^{+0.079}_{-0.097}$ | Ves2006 |

Table 4—Continued

| Source | R.A. | Dec. | Redshift | Type | $\lambda L_\lambda(5100\text{Å})$ ($\text{ergs s}^{-1}$) | $\lg(M_{\rm BH})$ ($M_\odot$) | Reference |
|---|---|---|---|---|---|---|---|
| (1) | (2) | (3) | (4) | (5) | (6) | (7) | (8) |
| PG1545+210 | 15h47m43.54s | +20d52m16.6s | 0.266 | 1.0 | $45.428^{+0.023}_{-0.024}$ | $9.314^{+0.084}_{-0.104}$ | Ves2006 |
| PG1552+085 | 15h54m44.58s | +08d22m21.5s | 0.119 | 1.0 | $44.407^{+0.015}_{-0.015}$ | $7.537^{+0.080}_{-0.099}$ | Ves2006 |
| PG1617+175 | 16h20m11.29s | +17d24m27.7s | 0.114 | 1.0 | $44.375^{+0.069}_{-0.082}$ | $8.436^{+0.115}_{-0.191}$ | Kaspi2000 |
| PG1626+554 | 16h27m56.12s | +55d22m31.5s | 0.133 | 1.0 | $44.580^{+0.026}_{0.028}$ | $8.498^{+0.081}_{-0.099}$ | Ves2006 |
| PG1700+518 | 17h01m24.80s | +51d49m20.0s | 0.292 | 1.0 | $45.470^{+0.010}_{-0.010}$ | $8.427^{+0.109}_{-0.146}$ | Mar2003 |
| PG1704+608 | 17h04m41.38s | +60d44m30.5s | 0.371 | 1.0 | $45.702^{+0.030}_{-0.032}$ | $9.391^{+0.086}_{-0.107}$ | Ves2006 |
| PG2112+059 | 21h14m52.57s | +06d07m42.5s | 0.466 | 1.0 | $46.181^{+0.034}_{-0.037}$ | $9.001^{+0.089}_{-0.112}$ | Ves2006 |
| PG2209+184 | 22h11m53.89s | +18d41m49.9s | 0.070 | 1.0 | $44.469^{+0.012}_{-0.013}$ | $8.766^{+0.080}_{-0.098}$ | Ves2006 |
| PG2214+139 | 22h17m12.26s | +14d14m20.9s | 0.067 | 1.0 | $44.662^{+0.097}_{-0.126}$ | $8.551^{+0.093}_{-0.118}$ | Ves2006 |
| PG2233+134 | 22h36m07.68s | +13d43m55.3s | 0.325 | 1.0 | $45.327^{+0.027}_{-0.028}$ | $8.036^{+0.083}_{-0.103}$ | Ves2006 |
| PG2251+113 | 22h54m10.40s | +11d36m38.3s | 0.323 | 1.0 | $45.692^{+0.026}_{-0.028}$ | $8.989^{+0.085}_{-0.106}$ | Ves2006 |
| PG2304+042 | 23h07m02.91s | +04d32m57.2s | 0.042 | 1.0 | $44.066^{+0.097}_{-0.126}$ | $8.564^{+0.092}_{-0.117}$ | Ves2006 |
| PG2308+098 | 23h11m17.76s | +10d08m15.5s | 0.432 | 1.0 | $45.777^{+0.101}_{-0.131}$ | $9.592^{+0.098}_{-0.126}$ | Ves2006 |
| 2MASSiJ081652.2+425829 | 08h16m52.24s | +42d58m29.4s | 0.235 | 1.0 | $44.605^{+0.002}_{-0.002}$ | $8.27^{+0.01}_{-0.01}$ | Shen2011 |
| 2MASSiJ095504.5+170556 | 09h55m04.55s | +17d05m56.4s | 0.139 | 1.0 | $45.130^{+0.000}_{-0.002}$ | $7.27^{+0.38}_{-0.38}$ | Shen2011 |
| 2MASSiJ130005.3+163214 | 13h00m05.35s | +16d32m14.8s | 0.080 | 1.0 | – | – | – |
| 2MASSiJ132917.5+121340 | 13h29m17.52s | +12d13m40.2s | 0.203 | 1.0 | – | – | – |
| 2MASSiJ1402511+263117 | 14h02m51.20s | +26d31m17.6s | 0.187 | 1.0 | $44.565^{+0.039}_{-0.039}$ | $8.57^{+0.03}_{-0.03}$ | Shen2011 |
| 2MASSiJ145608.6+275008 | 14h56m08.65s | +27d50m08.8s | 0.250 | 1.0 | $44.670^{+0.015}_{-0.015}$ | $7.95^{+0.01}_{-0.01}$ | Shen2011 |
| 2MASSiJ151653.2+190048 | 15h16m53.23s | +19d00m48.3s | 0.190 | 1.0 | $44.200^{+0.000}_{-0.000}$ | $8.22^{+0.00}_{-0.00}$ | Shen2011 |
| 2MASSiJ151901.5+183804 | 15h19m01.48s | +18d38m04.9s | 0.187 | 1.0 | – | – | – |
| 2MASSiJ154307.7+193751 | 15h43m07.78s | +19d37m51.8s | 0.228 | 1.5 | – | – | – |
| 2MASSiJ222221.1+195947 | 22h22m21.14s | +19d59m47.1s | 0.211 | 1.0 | – | – | – |
| 2MASSiJ223742.6+145614 | 22h37m42.60s | +14d56m14.0s | 0.277 | 1.0 | – | – | – |
| 2MASSiJ234259.3+134750 | 23h42m59.36s | +13d47m50.4s | 0.299 | 1.5 | $44.682^{+0.005}_{-0.005}$ | $8.41^{+0.02}_{-0.02}$ | Shen2011 |
| 2MASSiJ234449.5+122143 | 23h44m49.56s | +12d21m43.1s | 0.199 | 1.0 | – | – | – |
| 2MASXJ09210862+4538575 | 09h21m08.06s | +45d38m57.0s | 0.175 | 1.0 | $43.972^{+0.004}_{-0.004}$ | $8.83^{+0.04}_{-0.04}$ | Shen2011 |
| 2MASXJ00370409-0109081 | 00h37m04.01s | -01d09m08.0s | 0.074 | 1.0 | $45.170^{+0.000}_{-0.000}$ | $8.44^{+0.50}_{-0.50}$ | Shen2011 |
| 2MASXJ02335161+0108136 | 02h33m51.60s | +01d08m14.0s | 0.022 | 1.0 | – | – | – |
| 2MASXJ07582810+3747121 | 07h58m28.01s | +37d47m12.0s | 0.041 | 1.0 | $45.330^{+0.000}_{-0.000}$ | $8.90^{+0.53}_{-0.53}$ | Tri2013 |
| 2MASXiJ0208238-002000 | 02h08m23.08s | -00d20m01.0s | 0.074 | 1.0 | – | – | – |
| 2MASXJ02061600-0017292 | 02h06m16.00s | -00d17m29.0s | 0.043 | 1.0 | $43.850^{+0.000}_{-0.000}$ | $8.18^{+0.00}_{-0.00}$ | Du2014 |
| 2MASXJ10493088+2257523 | 10h49m30.90s | +22d57m52.0s | 0.033 | 1.0 | – | – | – |
| 2MASXJ12485992-0109353 | 12h48m59.90s | -01d09m35.0s | 0.089 | 1.0 | – | – | – |
| 2MASXJ14070036+2827141 | 14h07m00.40s | +28d27m15.0s | 0.077 | 1.0 | – | – | – |
| 2MASXJ02143357-0046002 | 02h14m33.50s | -00d46m00.0s | 0.026 | 1.0 | – | – | – |
| 2MASXJ09234300+2254324 | 09h23m43.00s | +22d54m33.0s | 0.033 | 1.0 | $45.104^{+0.000}_{-0.000}$ | $7.58^{+0.04}_{-0.04}$ | Dasyra.2011 |
| 2MASXJ12170991+0711299 | 12h17m09.90s | +07d11m30.0s | 0.008 | 1.0 | $42.080^{+0.000}_{-0.000}$ | $7.71^{+0.00}_{-0.00}$ | Woo2012 |
| 2MASXJ12232410+0240449 | 12h23m24.10s | +02d40m45.0s | 0.024 | 1.0 | $42.830^{+0.006}_{-0.006}$ | $7.51^{+0.07}_{-0.07}$ | HK2014 |
| 2MASXJ13381586+0432330 | 13h38m15.90s | +04d32m33.0s | 0.023 | 1.0 | $45.146^{+0.000}_{-0.000}$ | $7.56^{+0.00}_{-0.00}$ | WZ2007 |
| 2MASXJ13495283+0204456 | 13h49m52.80s | +02d04m45.0s | 0.033 | 1.0 | $42.394^{+0.000}_{-0.000}$ | $6.66^{+0.00}_{-0.00}$ | Zhu2010 |
| 2MASXJ23044349-0841084 | 23h04m43.50s | -08d41m09.0s | 0.047 | 1.0 | $43.720^{+0.000}_{-0.000}$ | $8.47^{+0.00}_{-0.00}$ | WL2004 |
| SDSSJ115138.24+004946.4 | 11h51m38.20s | +00d49m47.0s | 0.195 | 1.0 | $42.790^{+0.040}_{-0.040}$ | $6.00^{+0.00}_{-0.00}$ | GH2008 |
| SDSSJ170246.09+602818.8 | 17h02m46.10s | +60d28m19.0s | 0.069 | 1.0 | – | – | – |

Note. — Column (1): AGN name; Column (2): Right ascension of the AGN; Column (3): Declination of the AGN; Column (4): Redshift $z$; Column (5): Optical classification derived from the emission line ratio of the AGN: "1.0" for type 1 AGN with broad emission

lines, "2.0" for type 2 AGN with only narrow emission lines, values between 1.0 and 2.0 for intermediate types; Column (6): Power emitted at $\lambda = 5100$ Å; Column (7): Black hole mass (in unit of solar mass $M_{\odot}$); Column (8): References from which we collect $\lambda L_{\lambda}(5100\,\text{Å})$ and $M_{\rm BH}$ — N1987 = Neugebauer et al. (1987); Mar2003 = Marziani et al. (2003); SG1983 = Schmidt & Green (1983); WPM1999 = Wandel, Peterson & Malkan (1999); Kaspi2000 = Kaspi et al. (2000); WL2004 = Wu & Liu (2004); WZ2007 = Wang & Zhang (2007); GH2008 = Greene & Ho (2008); Ves2006 = Vestergaard et al. (2006); Dong2010 = Dong et al. (2010); Sani2010 = Sani et al. (2010); Zhu2010 = Zhu et al. (2010); Dasyra2011 = Dasyra et al. (2011); Shen2011 = Shen et al. (2011); Woo2012 = Woo et al. (2012); Tri2013 = Trichas et al. (2013); Rose2013 = Rose et al. (2013); Du2014 = Du et al. 2014; HK2014 = Ho & Kim (2014).

Table 5. Basic Parameters of 30 Sources from Our PG Quasar Sample, *2MASS* Quasar Sample, and S$^3$AGA AGN Sample Which Show No Silicate Emission but a Featureless Thermal Continuum

| Source | R.A. | Dec. | Redshift | Type | $\lambda L_\lambda$(5100Å) (ergs s$^{-1}$) | lg($M_{\rm BH}$) ($M_\odot$) | Reference |
|---|---|---|---|---|---|---|---|
| (1) | (2) | (3) | (4) | (5) | (6) | (7) | (8) |
| PG0838+770 | 08h44m45.26s | +76d53m09.5s | 0.131 | 1.0 | $44.727^{+0.015}_{-0.015}$ | $8.154^{+0.080}_{-0.099}$ | Ves2006 |
| PG1226+023 | 12h29m06.70s | +02d03m08.6s | 0.158 | 1.0 | $46.060^{+0.014}_{-0.014}$ | $9.262^{+0.130}_{-0.186}$ | Mar2003 |
| PG1354+213 | 13h56m32.80s | +21d03m52.4s | 0.300 | 1.0 | $44.977^{+0.072}_{-0.086}$ | $8.627^{+0.088}_{-0.110}$ | Ves2006 |
| PG1427+480 | 14h29m43.07s | +47d47m26.2s | 0.221 | 1.0 | $44.759^{+0.021}_{-0.022}$ | $8.088^{+0.081}_{-0.099}$ | Ves2006 |
| PG1448+273 | 14h51m08.76s | +27d09m26.9s | 0.065 | 1.0 | $44.482^{+0.011}_{-0.011}$ | $6.970^{+0.080}_{-0.098}$ | Ves2006 |
| PG1501+106 | 15h04m01.20s | +10d26m16.2s | 0.036 | 1.0 | $44.285^{+0.010}_{-0.011}$ | $8.523^{+0.079}_{-0.097}$ | Ves2006 |
| PG1543+489 | 15h45m30.24s | +48d46m09.1s | 0.400 | 1.0 | $45.445^{+0.037}_{-0.041}$ | $7.998^{+0.085}_{-0.105}$ | Ves2006 |
| 2MASSiJ010835.1+214818 | 01h08m35.10s | +21d48m18.0s | 0.285 | 1.9 | – | – | – |
| 2MASSiJ024807.3+145957 | 02h48m07.36s | +14d59m57.7s | 0.072 | 1.0 | $43.910^{+0.170}_{-0.170}$ | $7.46^{+0.00}_{-0.00}$ | Rose2013 |
| 2MASSiJ082311.3+435318 | 08h23m11.27s | +43d53m18.5s | 0.182 | 1.5 | – | – | – |
| 2MASSiJ145410.1+195648 | 14h54m10.17s | +19d56m48.7s | 0.243 | 1.9 | – | – | – |
| 2MASXJ17223993+3052521 | 17h22m39.90s | +30d52m53.0s | 0.043 | 1.0 | – | – | – |
| 2MASXJ13130577+0127561 | 13h13m05.80s | +01d27m56.0s | 0.029 | 1.0 | – | – | – |
| 2MASXJ13130565-0210390 | 13h13m05.70s | -02d10m39.0s | 0.084 | 1.0 | – | – | – |
| 2MASXJ15055659+0342267 | 15h05m56.50s | +03d42m26.0s | 0.036 | 1.0 | $43.450^{+0.000}_{-0.000}$ | $7.55^{+0.00}_{-0.00}$ | Dong2010 |
| 2MASXJ09191322+5527552 | 09h19m13.20s | +55d27m55.0s | 0.049 | 1.0 | – | – | – |
| 2MASXJ12384342+0927362 | 12h38m43.40s | +09d27m37.0s | 0.083 | 1.0 | – | – | – |
| 2MASXJ16164729+3716209 | 16h16m47.30s | +37d16m21.0s | 0.152 | 1.0 | – | – | – |
| 2MASXJ11230133+4703088 | 11h23m01.30s | +47d03m09.0s | 0.025 | 1.0 | – | – | – |
| 2MASXJ11110693+0228477 | 11h11m06.90s | +02d28m48.0s | 0.035 | 1.0 | – | – | – |
| 2MASSiJ1448250+355946 | 14h48m25.10s | +35d59m47.0s | 0.113 | 1.0 | – | – | – |
| SDSSJ090738.71+564358.2 | 09h07m38.70s | +56d43m58.0s | 0.099 | 1.0 | – | – | – |
| SDSSJ124035.81-002919.4 | 12h40m35.80s | -00d29m19.0s | 0.081 | 1.0 | | – | – |
| SDSSJ101536.21+005459.3 | 10h15m36.20s | +00d54m59.0s | 0.120 | 2.0 | – | – | – |
| SDSSJ164840.15+425547.6 | 16h48m40.10s | +42d55m48.0s | 0.129 | 1.0 | – | – | – |
| SDSSJ091414.34+023801.7 | 09h14m14.30s | +02d38m02.0s | 0.073 | 2.0 | – | – | – |
| SDSSJ164019.66+403744.4 | 16h40m19.70s | +40d37m45.0s | 0.151 | 1.0 | – | – | – |
| SDSSJ104058.79+581703.3 | 10h40m58.70s | +58d17m04.0s | 0.071 | 1.0 | – | – | – |
| UGC05984 | 10h52m16.70s | +30d03m55.0s | 0.035 | 2.0 | – | – | – |
| UGC06527 | 11h32m37.60s | +52d56m53.0s | 0.026 | 1.0 | – | – | – |

Note. — Column (1): AGN name; Column (2): Right ascension of the AGN; Column (3): Declination of the AGN; Column (4): Redshift $z$; Column (5): Optical classification derived from the emission line ratio of the AGN: "1.0" for type 1 AGN with broad emission lines, "2.0" for type 2 AGN with only narrow emission lines, values between 1.0 and 2.0 for intermediate types; Column (6): Power at $\lambda = 5100$ Å; Column (7): Black hole mass (in unit of solar mass $M_\odot$); Column (8): References from which we collect $\lambda L_\lambda(5100\,\text{Å})$ and $M_{\rm BH}$ — Mar2003 = Marziani et al. (2003); Ves2006 = Vestergaard et al. (2006); Dong2010 = Dong et al. (2010); Rose2013 = Rose et al. (2013).

Table 6. Basic Parameters of 24 Sources from Our PG Quasar Sample, *2MASS* Quasar Sample, and S$^3$AGA AGN Sample Which Show a Thermal Continuum Superimposed with PAH Features

| Source | R.A. | Dec. | Redshift | Type | $\lambda L_\lambda(5100\text{Å})$ ($\mathrm{ergs\,s^{-1}}$) | $\lg(M_{\rm BH})$ ($M_\odot$) | Reference |
|---|---|---|---|---|---|---|---|
| (1) | (2) | (3) | (4) | (5) | (6) | (7) | (8) |
| PG0007+106 | 00h10m31.01s | +10d58m29.5s | 0.089 | 1.0 | $44.816^{+0.014}_{-0.015}$ | $8.728^{+0.081}_{-0.099}$ | Ves2006 |
| PG0157+001 | 01h59m50.21s | +00d23m40.6s | 0.164 | 1.0 | $44.975^{+0.017}_{-0.018}$ | $8.166^{+0.081}_{-0.100}$ | Ves2006 |
| PG0923+129 | 09h26m03.29s | +12d44m03.6s | 0.029 | 1.0 | $43.860^{+0.097}_{-0.125}$ | $8.598^{+0.092}_{-0.117}$ | Ves2006 |
| PG0934+013 | 09h37m01.03s | +01d05m43.5s | 0.050 | 1.0 | $43.875^{+0.097}_{-0.126}$ | $7.041^{+0.092}_{-0.117}$ | Ves2006 |
| PG1022+519 | 10h25m31.28s | +51d40m34.9s | 0.045 | 1.0 | $43.696^{+0.097}_{-0.126}$ | $7.145^{+0.092}_{-0.117}$ | Ves2006 |
| PG1115+407 | 11h18m30.29s | +40d25m54.0s | 0.154 | 1.0 | $44.619^{+0.017}_{-0.018}$ | $7.667^{+0.080}_{-0.099}$ | Ves2006 |
| PG1119+120 | 11h21m47.10s | +11d44m18.3s | 0.049 | 1.0 | $44.132^{+0.012}_{-0.012}$ | $7.470^{+0.079}_{-0.097}$ | Ves2006 |
| PG1126-041 | 11h29m16.66s | -04d24m07.6s | 0.060 | 1.0 | $44.385^{+0.012}_{-0.012}$ | $7.749^{+0.080}_{-0.098}$ | Ves2006 |
| PG1149-110 | 11h52m03.54s | -11d22m24.3s | 0.049 | 1.0 | $44.107^{+0.097}_{-0.126}$ | $7.924^{+0.092}_{-0.117}$ | Ves2006 |
| PG1244+026 | 12h46m35.25s | +02d22m08.8s | 0.048 | 1.0 | $43.801^{+0.030}_{-0.032}$ | $6.523^{+0.080}_{-0.099}$ | Ves2006 |
| PG1415+451 | 14h17m00.70s | +44d56m06.0s | 0.114 | 1.0 | $44.561^{+0.017}_{-0.018}$ | $8.014^{+0.080}_{-0.098}$ | Ves2006 |
| PG1425+267 | 14h27m35.61s | +26d32m14.5s | 0.366 | 1.0 | $45.761^{+0.100}_{-0.130}$ | $9.734^{+0.097}_{-0.126}$ | Ves2006 |
| PG1519+226 | 15h21m14.26s | +22d27m43.9s | 0.137 | 1.0 | $44.710^{+0.019}_{-0.020}$ | $7.942^{+0.081}_{-0.099}$ | Ves2006 |
| PG1612+261 | 16h14m13.20s | +26d04m16.2s | 0.131 | 1.0 | $44.717^{+0.026}_{-0.028}$ | $8.058^{+0.081}_{-0.100}$ | Ves2006 |
| PG1613+658 | 16h13m57.18s | +65d43m09.6s | 0.129 | 1.0 | $44.650^{+0.070}_{-0.070}$ | $8.990^{+0.10}_{-0.10}$ | N1987, Kaspi2000 |
| PG2130+099 | 21h32m27.81s | +10d08m19.5s | 0.063 | 1.0 | $44.280^{+0.011}_{-0.011}$ | $7.947^{+0.081}_{-0.099}$ | Mar2003 |
| 2MASSiJ165939.7+183436 | 16h59m39.77s | +18d34m36.8s | 0.170 | 1.0 | $44.241^{+0.006}_{-0.006}$ | $8.950^{+0.03}_{-0.03}$ | Shen2011 |
| 2MASXJ08381094+2453427 | 08h38m10.90s | +24d53m43.0s | 0.029 | 1.0 | – | – | – |
| 2MASXJ22533142+0048252 | 22h53m31.40s | +00d48m26.0s | 0.072 | 1.0 | – | – | – |
| 2MASXJ15085397-0011486 | 15h08m53.90s | -00d11m49.0s | 0.054 | 1.0 | – | – | – |
| 2MASXJ14175951+2508124 | 14h17m59.50s | +25d08m12.0s | 0.016 | 1.0 | – | – | – |
| 2MASXJ12042964+2018581 | 12h04m29.70s | +20d18m58.0s | 0.023 | 1.0 | – | – | – |
| 2MASXJ10032788+5541535 | 10h03m27.90s | +55d41m54.0s | 0.146 | 2.0 | – | – | – |
| 2MASSJ16593976+1834367 | 16h59m39.80s | +18d34m37.0s | 0.171 | 1.0 | – | – | – |

Note. — Column (1): AGN name; Column (2): Right ascension of the AGN; Column (3): Declination of the AGN; Column (4): Redshift $z$; Column (5): Optical classification derived from the emission line ratio of the AGN: "1.0" for type 1 AGN with broad emission lines, "2.0" for type 2 AGN with only narrow emission lines, values between 1.0 and 2.0 for intermediate types; Column (6): Power at $\lambda = 5100$ Å; Column (7): Black hole mass (in unit of solar mass $M_\odot$); Column (8): References from which we collect $\lambda L_\lambda(5100\,\text{Å})$ and $M_{\rm BH}$ — N1987 = Neugebauer et al. (1987); Mar2003 = Marziani et al. (2003) Kaspi2000 = Kaspi et al. (2000); Ves2006 = Vestergaard et al. (2006); Shen2011 = Shen et al. (2011).